

UC San Diego

UC San Diego Electronic Theses and Dissertations

Title

Phase Control and Processing Methods for High-Coercivity Magnets based on Metastable Fe₂O₃

Permalink

<https://escholarship.org/uc/item/8q08q7pp>

Author

Chan, Kyle T

Publication Date

2018

Peer reviewed|Thesis/dissertation

UNIVERSITY OF CALIFORNIA SAN DIEGO

Phase Control and Processing Methods for High-Coercivity Magnets based on Metastable Fe₂O₃

A dissertation submitted in partial satisfaction of the requirements
for the degree of Doctor of Philosophy

in

Materials Science and Engineering

by

Kyle Tong Yuen Chan

Committee in charge:

Professor Javier E. Garay, Chair
Professor Renkun Chen
Professor Eric E. Fullerton
Professor Vitali Nesterenko
Professor Jeffrey Rinehart

2018

Copyright

Kyle Tong Yuen Chan, 2018

All rights reserved.

The Dissertation of Kyle Tong Yuen Chan is approved, and it is acceptable in quality and form
for publication on microfilm and electronically:

Chair

University of California San Diego

2018

DEDICATION

This dissertation is dedicated to those who supported me throughout my life – culminating in the successful completion of my graduate studies. First and foremost, this dissertation is dedicated to my family, who encouraged me to pursue and complete my graduate degrees. Next is my friends and colleagues, who provided support in various forms, including emotional and intellectual support when it was most needed. Finally, this dissertation could not have been completed without the occasional carne asada burrito, the phenomenal beer from Alesmith brewery, the comforting and beer-filled environment of Quantum Brewing which was conducive to the writing process, and most importantly - a certain adorable and fluffy dog by the name of Nova.

EPIGRAPH

Ooooooooooh.

Dr. Yasuhiro Koderu

TABLE OF CONTENTS

SIGNATURE PAGE	iii
DEDICATION	iv
EPIGRAPH	v
TABLE OF CONTENTS	vi
LIST OF FIGURES	viii
LIST OF TABLES.....	xii
ACKNOWLEDGEMENTS	xiii
VITA	xiv
ABSTRACT OF THE DISSERTATION	xv
1. INTRODUCTION TO NANOMETRIC IRON OXIDES	1
1.1. Introduction and Motivation	1
1.2. Thermodynamics and Kinetics of Iron Oxide Polymorphs	2
1.2.1. Background on Iron Oxide Phases.....	2
1.2.2. Phase Stability of Nanometric Fe ₂ O ₃	5
1.3. Relating Crystallographic Phase and Magnetic Properties.....	12
1.3.1. Fundamentals of Magnetic Materials.....	12
1.3.2. Properties of Permanent Magnetic Materials.....	19
1.3.3. Magnetic Properties of Fe ₂ O ₃ Polymorphs.....	23
2. SYNTHESIS AND PROCESSING OF BULK AND POWDER Fe ₂ O ₃	30
2.1. Prior Work on Chemical Synthesis Methods for Fe ₂ O ₃ Powder	30
2.2. Overview and Prior Work on Chemical Synthesis of ε-Fe ₂ O ₃ /SiO ₂ Precursor Powders	34
2.3. Background on Modifying Fe/O Diffusivity Through Silica/Silicate Glass	39
2.4. Powder Processing and Consolidation Techniques for Fe-O/Si-O Composites.....	42
2.4.1. Overview of Powder Processing Methods.....	42
2.4.2. Overview of Powder Consolidation/Densification Methods	44
3. RELEVANT CHARACTERIZATION TECHNIQUES FOR	49
4. TUNING PHASE STABILITY OF ε-Fe ₂ O ₃ BY KINETICS AND GROWTH CONTROL.....	54
4.1. Background on Size Dependent Stability and Growth of Nanometric Fe ₂ O ₃	54
4.2. Growth Mechanisms of Nanometric Fe ₂ O ₃ in a Silica Matrix	55
4.3. Sodium-Silicate Shell Synthesis Procedure	60

4.4. Results and Discussion of Sodium-Silicate Shell Effects on Growth Behavior of ϵ - Fe_2O_3	64
4.5. Results and Discussion of Sodium-Silicate Shell Effects on Magnetic Properties of ϵ - Fe_2O_3	70
4.6. Magnetic Annealing Effects on Nanometric Fe_2O_3	78
4.7. Summary of Chapter 4	85
5. HIGH COERCIVITY COMPOSITE MAGNET WITH HIGH ϵ - Fe_2O_3 CONTEN.....	86
5.1. Bulk Composite Magnet Based on Metastable ϵ - Fe_2O_3	86
5.2. Experimental Procedure.....	87
5.3. Results and Discussion	88
5.4. Dense Magnetic Fe-O/Na-Si-O Composites.....	102
5.5. Summary of Chapter 5	108
6. SUMMARY AND CONCLUSIONS	110
APPENDIX.....	114
A-1 Grain Growth Kinetics Calculations.....	114
A-2 Grain Growth Kinetics Calculation Results	115
A-3 Additional Magnetic Hysteresis Measurements	116
A-3.1 Hysteresis of Na-Si-O-15 samples.....	116
A-3.2 Hysteresis of Si-O-15 samples.....	117
A-3.3 Hysteresis of Si-O-90 Samples	118
A-3.4 Hysteresis of Densified Na-Si-O-15 and Si-O-15 Samples.....	119
A-4 Surface Area to Volume Ratios	120
REFERENCES	121

LIST OF FIGURES

Figure 1.1 Crystal structure of (a) γ -Fe ₂ O ₃ (b) ϵ -Fe ₂ O ₃ (c) β -Fe ₂ O ₃ and (d) α -Fe ₂ O ₃ generated by VESTA software[8], constructed using data adapted from [9], [10], [11], and [12], respectively.	3
Figure 1.2 Phase-map of Fe ₂ O ₃ polymorphs, correlating particle size and annealing temperature to crystallographic phase from [28]	6
Figure 1.3 Qualitative plot of Gibbs free energy (G) vs particle diameter (d), in which the stability of each Fe ₂ O ₃ polymorph is shown relative to particle size, adapted from [5].....	7
Figure 1.4 Data adopted from [5], indicating phase transformations are primarily size-driven... ..	12
Figure 1.5 Magnetic moments attributed to the electron spin and orbit at the first Bohr orbital give the Bohr magneton (μ_B), a fundamental unit for magnetic moment.....	14
Figure 1.6 (a) moment from an electron, also known as a Bohr magneton (b) size scale of a crystal lattice (c) size scale of a magnetic domain (d) domains within a single grain.....	16
Figure 1.7 Magnetic moment behavior in bulk materials before (a-I, b-I, c-I, d-I), during (a-II, b-II, c-II, d-II), and after (a-III, b-III, c-III, d-III) application of an external magnetic field in diamagnetic (a), paramagnetic (b), ferromagnetic (c), and antiferromagnetic (d), respectively ..	21
Figure 1.8 Sublattice exchange diagram demonstrating the antiferromagnetic sublattice exchange between the four sublattices, with the uncompensated ferromagnetic component due to the tetrahedral site., adapted from [27]	25
Figure 1.9 Crystal structure and expected magnetic hysteresis behavior of each Fe ₂ O ₃ polymorph.	28
Figure 1.10 Field cooling curves from [5], demonstrating the different magnetic responses of each polymorph to temperature	29
Figure 2.1 Structure of micelle (a) vs reverse-micelle (b) – the polar nature of the surfactant preferentially organizes to minimize surface energies, with the ratio of water to oil phase as the primary determining factor for micelle vs reverse-micelle formation.....	35
Figure 2.2 Steps of reverse-micelle/sol-gel process used to synthesize precursor materials used in subsequent work. Two reverse-micelle solutions containing the reactants are prepared, then a sol-gel process is used to form a diffusion matrix, followed by heat-treatment to form the desired phase	37
Figure 2.3 Figure adapted from [28], Structure models showing the twin relationships and crystal interfaces: (a) the inversion twin relationship (b) the (110) twinning relationship and (c) the crystal interfaces between ϵ -Fe ₂ O ₃ and α -Fe ₂ O ₃ along the c-axis.....	38
Figure 2.4 (a) Diffusivity of various metal ions through different metal-oxides, figure from [82] and (b) Diffusion of iron through a silica layer grown on a silicon substrate, figure from [83]. Diffusivity of Fe through sodium-silicate glass is shown to be significantly higher than pure SiO ₂	41
Figure 2.5 Diagram of CAPAD apparatus and the die and plunger set which houses the sample. Rapid joule heating and mechanical loads are applied via the top and bottom electrodes.	47

Figure 3.1 (a) A typical VSM setup with two toroidal electromagnets (a-I) used to generate the external field, pole pieces (a-II) to increase flux density, motor head to vibrate the sample (a-III), and pickup coils in which an EMF is induced and correlated to magnetization values (a-IV). Field directions are shown in a (b) classic VSM design and a (c) modern SQUID system 50

Figure 4.1 (a) Long-range diffusion of Fe and O through the silica matrix, leading to the smaller Fe-O particle shrinking and the larger Fe-O particle growing. (b) The short-range rearrangement along the c-axis, which leads to the phase transformation from ϵ -Fe₂O₃ to α -Fe₂O₃, adapted from [28]..... 55

Figure 4.2 (a) Average diameter of spherical nanoparticles versus annealing temperature, adapted from [5]. (b) Grain growth model applied to data from [5]..... 56

Figure 4.3 Average dimensions of the (a) short and (c) long axes of the nanorods reported in [24], [25], [73] Grain growth kinetics model applied to the (b) short and (d) long axes dimensions of the nanorods from [24], [25], [73], R² values are 0.979 and 0.991 for the short and long axes, respectively 59

Figure 4.4 Replacing the matrix through which Fe and O atoms diffuse with a higher-diffusivity material (SiO₂ vs Na-Si-O), it is proposed that similar diffusion kinetics can be achieved with significantly lower temperatures, leading to a lower-temperature ϵ -Fe₂O₃ phase stabilization.. 60

Figure 4.5 (a) sodium-nitrate is dissolved into water and mixed into the core-shell power prepared via reverse-micelle/sol-gel process (b) the sodium-nitrate solution is mixed to evenly distribute the sodium source (c) the sodium is evenly distributed on the precursor powder and (d) after heat-treatment, the SiO₂ shell is converted to an Na-Si-O shell..... 61

Figure 4.6 Synthesis procedure for iron oxide/sodium-silicate core-shell powder. Addition of sodium is performed at an intermediate step in order to introduce the sodium prior to crystallization of the silica shell..... 63

Figure 4.7 (a) SEM micrograph of synthesized core-shell Si-O/Fe-O nanoparticles (b) TEM micrograph showing iron oxide core with thick silica shell, courtesy of Dr. Takahito Imai of Ryukoku University, Shiga Japan..... 64

Figure 4.8 SEM and EDS of the as-synthesized powders, prior to annealing, indicate small initial particle sizes (<50nm) and a homogenous distribution of sodium 65

Figure 4.9 SEM micrographs of Si-O vs Na-Si-O shell samples show similar microstructure and nanorod distribution, indicating similar growth kinetics at different temperatures..... 66

Figure 4.10 Comparison of dimensions of Fe₂O₃ nanorods synthesized in this work using Na-Si-O and Si-O matrices with 15 mol% Fe-Ba concentration with values reported in [24], [25], [73]. Similar nanorod dimensions at different temperatures are seen for the Na-Si-O and Si-O samples. 67

Figure 4.11 Increasing the iron oxide concentration (90 mol% cation concentration) leads to decreased interparticle distance and increased growth under the same conditions, allowing for significantly increased growth of nanorods. 69

Figure 4.12 Magnetization vs field hysteresis loops of Na-Si-O-15 and Si-O-15 samples annealed at 875°C and 1050°C, respectively. The similar magnetic properties and high coercivities indicate ϵ -Fe₂O₃ is likely the dominant phase 71

Figure 4.13 Field-cooling measurements of Na-Si-O-15 and Si-O-15 samples, which show a Morin-like transition at 150K, attributed to the ϵ -Fe ₂ O ₃ phase.	73
Figure 4.14 Magnetic hysteresis loops of Na-Si-O-90 and Si-O-90 samples show a decrease in coercivity in the Na-Si-O-90 sample, which can attributed to decreased homogeneity of the nanorods. The coercivity values in both samples are within the range expected for ϵ -Fe ₂ O ₃	74
Figure 4.15 Field-cooling of Na-Si-O-90 and Si-O-90 samples show a broadening of the Morin-like transition in the Na-Si-O-90 sample, which can be attributed to the increased variation in nanorod size and dimensions. A second transition \sim 100K may be due to presence of β -Fe ₂ O ₃ The Si-O-90 sample shows a typical transition expected in ϵ -Fe ₂ O ₃	75
Figure 4.16 Coercivity versus annealing temperature of Si-O and Na-Si-O samples, indicating that the maximum coercivity of Na-Si-O samples is reached at a significantly lower temperature than Si-O samples.	77
Figure 4.17 Diagram of the magnetic annealing furnace designed for the annealing tests. The system is designed to keep consistent heating parameters with a removable furnace in order to compare samples annealed with a field and without a field	79
Figure 4.18 Normalized hysteresis loops comparing Si-O-90 samples annealed with and without an external magnetic field at 450, 600, 700, 800, 900, and 950°C.	81
Figure 4.19 Field cooling of sample annealed at 600°C with an external field, showing an increase in magnetization that is consistent with previously reported low-temperature behavior of γ -Fe ₂ O ₃ [5]	83
Figure 4.20 (a) Field cooling curves of samples annealed at 600C with and without field (b) field cooling of the sample annealed at 600C without field.....	84
Figure 5.1 Synthesis and densification process to attain a bulk composite with ϵ -Fe ₂ O ₃ nanorods/silica matrix[57]	88
Figure 5.2 (a) SEM of pre-annealed powder showing small (sub-50nm) particles, and (b) post-annealing and partial etching showing high-aspect ratio nanorods. (c) XRD analysis shows a transition from a primarily amorphous (I) material to a crystalline material comprised of cristobalite (silica) and ϵ -Fe ₂ O ₃ (II). (d) magnetic hysteresis indicate a transition from a weakly paramagnetic material to a high-coercivity magnetic material[57]	90
Figure 5.3 (a) Normalized extension curves show drastic change in densification behavior at 90 mol% concentration. (b) XRD analysis of samples with increasing iron oxide content indicate that ϵ -Fe ₂ O ₃ begins to dominate at high concentrations, but also begins to form secondary iron oxide phases. (c) Varying density of the IO-90 samples finds that lower density allows for ϵ -Fe ₂ O ₃ to exist in higher concentration[57].....	93
Figure 5.4 (a) Plot of coercivity vs IO concentration, (b) plot of coercivity vs primary peak ratio between ϵ -Fe ₂ O ₃ and α -Fe ₂ O ₃ , SEM micrographs of (c) bulk fracture surface prior to annealing, (d) bulk fracture surface after annealing, and (e) bulk fracture surface after annealing and polishing of the surface[57]	97
Figure 5.5 (a) Room temperature M-H loops of IO-15 vs IO-90 samples of comparable density, (b) low-temperature M-H loops of IO-15 vs IO-90 samples, (c) field cooling of IO-90 sample, (d) FMR measurement of IO-90 sample[57]	100

Figure 5.6 Normalized extension curves of Na-Si-O and Si-O samples with comparable cation concentrations plotted versus temperature.....	102
Figure 5.7 Hysteresis loops of bulk Na-Si-O-15 and Si-O-15 samples annealed at 875C and 1025C, respectively.....	105
Figure 5.8 Field cooling of densified Na-Si-O-15 sample, annealed at 875°C. Two transitions occur which can be attributed to the presence of β -Fe ₂ O ₃ which is stable at a larger size range than ϵ -Fe ₂ O ₃	106
Figure 5.9 Coercivity of densified Na-Si-O-15 and Si-O-15 samples annealed at 450, 600, 875, and 1025°C.....	107
Figure A.1 Hysteresis loops of Na-Si-O-15 samples annealed at temperatures ranging from 450-1000°C.....	116
Figure A.2 Hysteresis loops of Si-O-15 samples annealed at varying temperatures from 450-1100°C.....	117
Figure A.3 Hysteresis loops of Si-O-90 samples annealed from 450-1100°C	118
Figure A.4 Hysteresis of densified Na-Si-O-15 and Si-O-15 samples annealed at 450, 600, 875, and 1025°C.....	119
Figure A.5 Surface area-to-volume ratios of various geometries	120

LIST OF TABLES

Table 4.1 Diffusion constants (k) calculated from Eq 1.2.5 for Fe/O through Na-Si-O and Si-O shells, compared with k values calculated from [5], [24], [25], [73] at different temperatures....	68
Table 5.1 Comparison of the coercivity of samples with different cation concentration (samples #1-4) and varying densities at high concentration (samples#4-6)[57].....	95
Table 5.2 The densification onset temperature, densities measured by Archimedes method, resulting relative densities and coercivities for the Si-O and Na-Si-O samples. The * indicates that the sample was annealed at 875°C instead of 1025°C	103
Table A.1 Calculation of grain growth constant (k) for values reported in literature as well as values found in this work	115

ACKNOWLEDGEMENTS

This work gratefully acknowledges the contributions of Dr. Jason Morales who was integral in the development of this project, Professor Ward Beyermann (UC Riverside) and Professor Jing Shi (UC Riverside) whose equipment was used for many preliminary measurements, Dr. Takahito Imai (Ryuokoku University) for his TEM contributions, and the Office of Naval Research (ONR) with Dr. H.S. Coombe as program manager who supported this work.

Chapter 4 is co-authored with Professor Javier E. Garay and Dr. Yasuhiro Kodera. It is currently in preparation for submission. The dissertation author was the primary investigator and author on this paper.

Chapter 5 is co-authored by Dr. Jason R. Morales, Dr. Yasuhiro Kodera, and Professor Javier E. Garay, and is published in *Journal of Materials Chemistry C* 2017,**5**, 7911-7918. The dissertation author was the primary investigator and author on this paper.

VITA

2008	Bachelor of Science, University of California, Riverside
2012-2016	Research Assistant, University of California, Riverside
2013-2014	Teaching Assistant, University of California, Riverside
2014	Master of Science, University of California, Riverside
2016-2018	Research Assistant, University of California, San Diego
2018	Doctor of Philosophy, University of California, San Diego

PUBLICATIONS

“A processing route for bulk, high coercivity, rare-earth free, nanocomposite magnets based on metastable iron oxide”. *Journal of Materials Chemistry C*. doi: 10.1039/c7tc01789h

“Thermal and magnetic properties of nanostructured densified ferrimagnetic composites with graphene-graphite fillers”. *Materials and Design* 118, 75-80. doi: 10.1016/j.matdes.2017.01.018

“Exquisite growth control and magnetic properties of yttrium iron garnet thin films”. *Applied Physics Letters*, 108(10). doi:10.1063/1.4943210

ABSTRACT OF THE DISSERTATION

Phase Control and Processing Methods for High-Coercivity Magnets based on Metastable Fe₂O₃

by

Kyle Tong Yuen Chan

Doctor of Philosophy in Materials Science and Engineering

University of California San Diego 2018

Professor Javier E. Garay, Chair

High coercivity magnets are crucial in modern technology. Current state-of-the-art, high coercivity magnets rely on rare earth elements and/or precious metals which raises environmental and economic concerns. For this reason, the development of high-coercivity permanent magnetic materials comprised of earth-abundant and environmentally friendly materials is of world-wide interest. The focus of this work was the development of bulk, nanocomposite permanent magnetic materials based on the high-coercivity, metastable ϵ -Fe₂O₃ phase. A reverse-micelle/sol-gel process was used to synthesize Fe₂O₃/SiO₂ core-shell structures, with Ba used as an aid in the formation of ϵ -Fe₂O₃ nanorods. Initial samples were prepared with an Fe/Ba concentration of 15 mol%. The SiO₂ acted as a long range diffusion-mediating matrix, which allows for the controlled growth and stabilization of the metastable Fe₂O₃ phases. Annealing at 1050°C resulted in ϵ -Fe₂O₃ nanorods with a maximum coercivity of 17.5 kOe. The diffusivity of Fe/O was increased through modification of the Si-O matrix with Na addition which resulted in ϵ -Fe₂O₃ nanorod formation with comparable dimensions and magnetic properties at 875°C. This significant decrease in growth temperature confirms the hypothesis that ϵ -Fe₂O₃ stability is size dependent and is controlled by long range diffusion. Annealing experiments were also done using an externally applied magnetic

field to investigate the effect of a magnetic field on the growth of nanometric Fe_2O_3 . It was found that magnetic ordering was induced at 600°C , which is 300°C lower than samples annealed without field. The Si-O and Na-Si-O shells thicknesses were decreased to increase the Fe/Ba concentration, and therefore the magnetic content, to 90 mol%, resulting in samples with coercivities ≥ 13.0 kOe. Finally, bulk, high-coercivity magnets comprised primarily of the metastable $\epsilon\text{-Fe}_2\text{O}_3$ phase were produced by rapidly densifying the composite Fe-O/Si-O composite powders via Current Activated Pressure Assisted Densification (CAPAD), followed by annealing. The Na-Si-O shell powders with 15 mol% Fe/Ba were also densified via CAPAD processing, resulting in relative densities $\sim 99\%$, and high coercivities similar to the ideal Fe-O/Si-O powder samples. The nanocomposites produced in this work have some of the highest coercivities ever reported in dense millimeter-sized magnets that do not contain rare earths or precious metals.

1. INTRODUCTION TO NANOMETRIC IRON OXIDES

1.1. Introduction and Motivation

Magnetic materials have been integral to the development of a wide array of modern technology, ranging from data storage to energy production, and even biomedical applications. Historically, magnetic materials were first recorded with the discovery of Fe_3O_4 (magnetite) in ancient Greece in 385 B.C., and became integral to human exploration with the invention and widespread use of the magnetic compass around 1200 A.D. [1]. By the mid-20th century, permanent magnetic materials had become critical to the modern civilization, being used in power generators, electric motors, transformers, and even in various home appliances. With the development of modern computers, the focus of magnetic materials research shifted from bulk properties to nanostructured properties (i.e. thin films) for data storage applications[2]. In both bulk and nanoscale applications of magnetic materials, there is a heavy reliance on rare earth-based magnetic materials, specifically the Neodymium-Iron-Boron material system. In recent years there has been renewed interest in alternative high-performance bulk magnetic materials due to the ever-increasing energy demand worldwide and the economic and environmental concerns associated with the current state-of-the-art magnetic materials, which are either rare earth or precious metal-based[3]. To overcome the environmental, economic, and political concerns associated with the production of rare earth-based magnetic materials, a proposed alternative is to take advantage of the unique properties found in metastable phases of earth-abundant materials.

The Fe_2O_3 material system is of particular interest due to the unique magnetic properties of the metastable phases, particularly the $\epsilon\text{-Fe}_2\text{O}_3$ phase, which exhibits a remarkably high coercivity that is comparable to rare-earth based magnets, making it a viable candidate for future

permanent magnetic applications. However, to fully utilize these metastable materials, a high degree of phase selectivity and understanding of thermodynamic stabilities is required. This work presents methods of controlling and utilizing metastable iron oxide phases with unique magnetic properties as bulk, functional composites by controlling thermodynamic and kinetic processes.

1.2. Thermodynamics and Kinetics of Iron Oxide Polymorphs

1.2.1. Background on Iron Oxide Phases

Iron oxides, are some of the most earth abundant materials, and can exist in multiple stoichiometries, including FeO, Fe₃O₄, Fe₂O₃, as well as multiple hydroxylated and hydrated forms (goethite, akagenéite, ferrihydrite, etc.)[4]. While Fe₃O₄, commonly known as magnetite, is the oldest known ferromagnetic material, Fe₂O₃ is particularly interesting due to the existence of five (isochemical) crystallographic polymorphs[4]–[7]. Currently, five known polymorphs have been observed, with four of these having been well-characterized magnetically. Since they each have a different crystal structure, as shown in **Figure 1.1**, they also have unique magnetic properties that will be discussed subsequently.

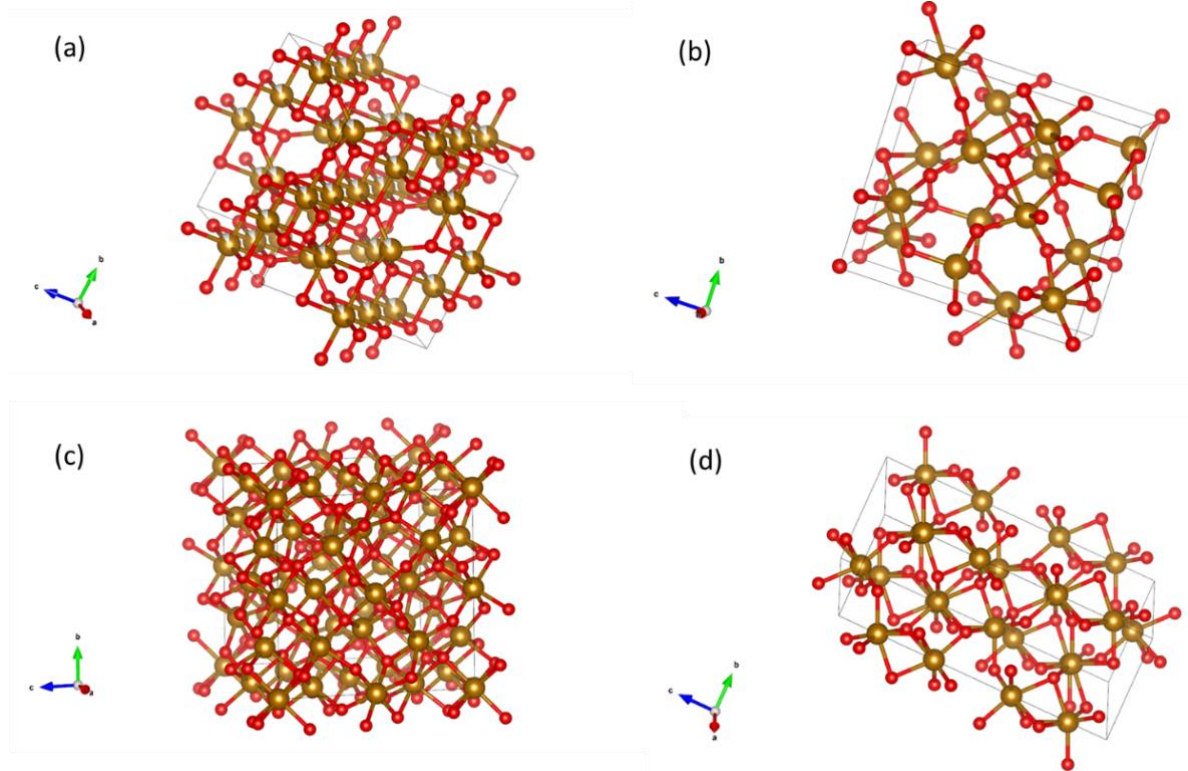


Figure 1.1 Crystal structure of (a) γ -Fe₂O₃ (b) ϵ -Fe₂O₃ (c) β -Fe₂O₃ and (d) α -Fe₂O₃ generated by VESTA software[8], constructed using data adapted from [9], [10], [11], and [12], respectively.

Of the four polymorphs, the most common and stable phase is α -Fe₂O₃, commonly known as hematite, or rust. The α -Fe₂O₃ phase is a hexagonal crystal system with a corundum structure (**Figure 1.1d**), and has been shown to have a structural relationship with other phases, such as the relation between the (001) plane with the (111) plane of magnetite or the (001) plane of ϵ -Fe₂O₃. As a consequence, it is possible for multiple phases to nucleate along certain planes of a hematite structure. Prior work has demonstrated that the preferred morphology of α -Fe₂O₃ is size dependent, and similarly, as are the magnetic properties[4]. At room temperature, α -Fe₂O₃ exhibits a slightly canted antiferromagnetic, or weakly ferromagnetic behavior, and exhibits a range of Morin transition temperatures, typically around 270 K, which are size, morphology, or defect dependent[13]–[15]. The second most common phase is the γ -Fe₂O₃ phase (commonly

known as maghemite), which exists in an inverse-spinel structure (**Figure 1.1a**), and is considered to be the most stable nanometric Fe_2O_3 phase. The ferrimagnetic properties of $\gamma\text{-Fe}_2\text{O}_3$ arise from the two sublattices comprised of Fe atoms located at tetrahedral and octahedral sites. Each sublattice contain parallel moments, but are antiparallel to each other[4], [16], [17]. Two additional polymorphs have been shown to exist as intermediate phases during the transformation from $\gamma\text{-Fe}_2\text{O}_3$ to $\alpha\text{-Fe}_2\text{O}_3$: $\varepsilon\text{-Fe}_2\text{O}_3$ and $\beta\text{-Fe}_2\text{O}_3$, both of which are highly metastable, and are difficult to synthesize as a phase-pure material. $\varepsilon\text{-Fe}_2\text{O}_3$ is described as an orthorhombic (**Figure 1.1b**), non-centrosymmetric structure, comprised of four sublattices with distinct Fe sites. It has been heavily studied primarily as a nanomaterial, with a predicted size range of ~10 nm to 200 nm with an average particle size of ~50 nm as spherical particles, and exhibits a unique magnetic behavior in that it has been considered either a non-collinear ferromagnetic or canted antiferromagnet. The unique magnetic properties arise from the complex crystal structure, which is comprised of four sublattices, with Fe atoms occupying three octahedral and one tetrahedral site[18]–[20]. Interestingly, $\varepsilon\text{-Fe}_2\text{O}_3$ has been shown to share a crystal interface along c-axis with $\alpha\text{-Fe}_2\text{O}_3$, and this interface has been proposed to serve as the substrate/interface for $\alpha\text{-Fe}_2\text{O}_3$ formation from $\varepsilon\text{-Fe}_2\text{O}_3$. $\beta\text{-Fe}_2\text{O}_3$ exhibits primarily a paramagnetic behavior, and is extremely difficult to produce as a single phase material. Work by Sakurai, et al.[5] demonstrated the first observation of phase transformation through all four polymorphs of Fe_2O_3 , using mesoporous silica both as nano-reaction sites as well as a diffusion barrier to control the growth rate of Fe_2O_3 nanoparticles. The work demonstrated that by controlling the diffusion and kinetics of the nanoparticles, it was possible to reliably determine the temperature and size dependence of the various polymorphs for spherical nanoparticles.

1.2.2. Phase Stability of Nanometric Fe₂O₃

The initial particle size and growth kinetics of iron oxides is largely controlled by the synthesis conditions, including cation concentration, inorganic and organic additives, pH, and temperature[21]. While the various factors contributing to phase transformation can be summarized within enthalpy and entropy terms, the enthalpy, which is proposed to have a significant effect on the free energy[21], [22] , is greatly influenced by surface energies. Some ambiguity may arise regarding the degree to which particle size contributes to the overall free energy, as many works have reported different conclusions due to variations in synthesis and processing parameters[4], [16], [21], [23]–[27]. Work by G. Schimanke and M. Martin further demonstrated the link between particle size and phase stability, as in-situ X-ray diffraction was performed during thermal treatment in order to observe the growth and phase transformation kinetics from γ -Fe₂O₃ to α -Fe₂O₃[16]. In the work, it was shown that the average particle size of α -Fe₂O₃ particles was significantly larger than γ -Fe₂O₃, and a first-order kinetics model was found to fit well in describing the growth behavior of Fe₂O₃ particles and ensuing phase transformation.

More recently, work by Lee and Xu constructed a phase map with the dominant phase as a function of annealing temperature and particle size. Also discussed in this work was the phase transformation kinetics for the transformation between γ -Fe₂O₃, ϵ -Fe₂O₃, and α -Fe₂O₃ which was described with a first-order kinetics equation[28]. The samples were prepared by thermally decomposing nontronite (a naturally occurring Iron (III)-rich mineral), then annealing to facilitate particle growth[28]. **Figure 1.2**, from Lee and Xu, demonstrates the link between dominant phase, particle size, and annealing temperature. It is a powerful tool in developing novel methods of attaining the desired phase of Fe₂O₃.

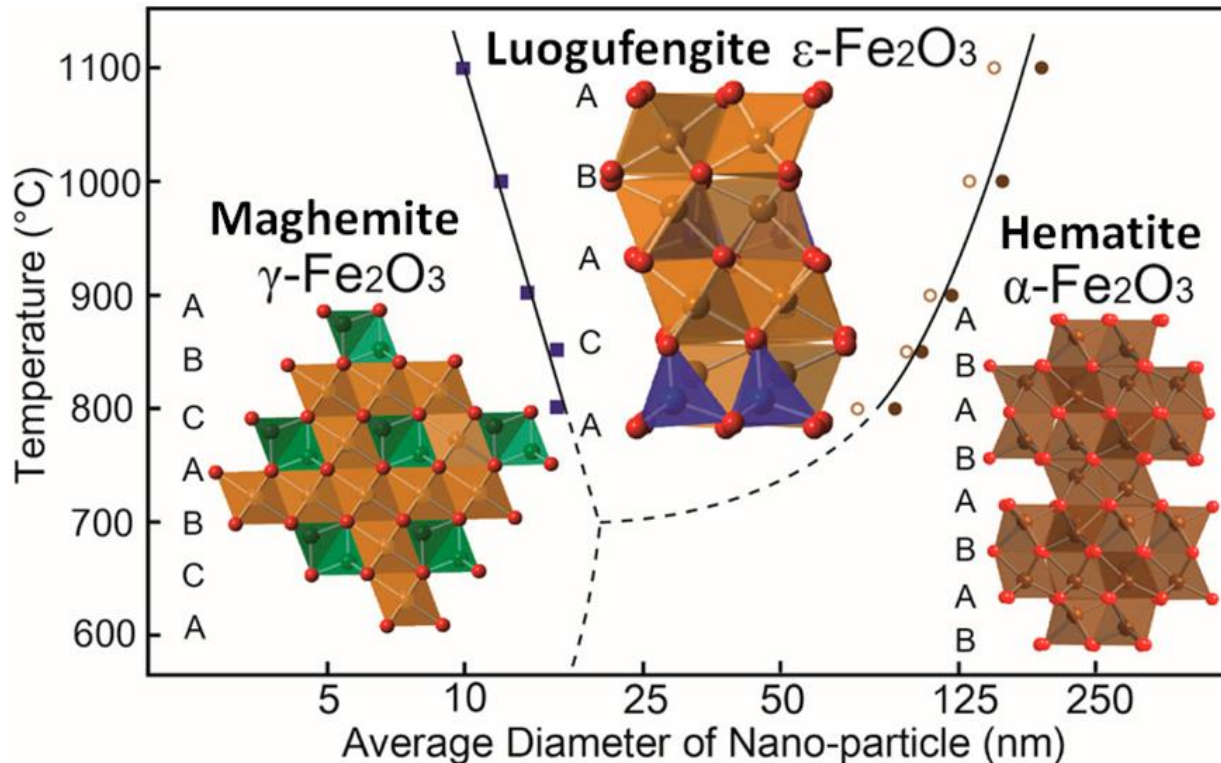


Figure 1.2 Phase-map of Fe₂O₃ polymorphs, correlating particle size and annealing temperature to crystallographic phase from [28]

Prior to this work, the formation of ε-Fe₂O₃ was shown to occur through the agglomeration of γ-Fe₂O₃ nanoparticles, and has been demonstrated to exist at intermediate particle sizes between the stable size range of γ-Fe₂O₃ and the most thermodynamically stable α-Fe₂O₃[19], [20], [29]. The link between particle size and stability (free energy) is best represented in the qualitative plot from Sakurai, et al. (**Figure 1.3**):

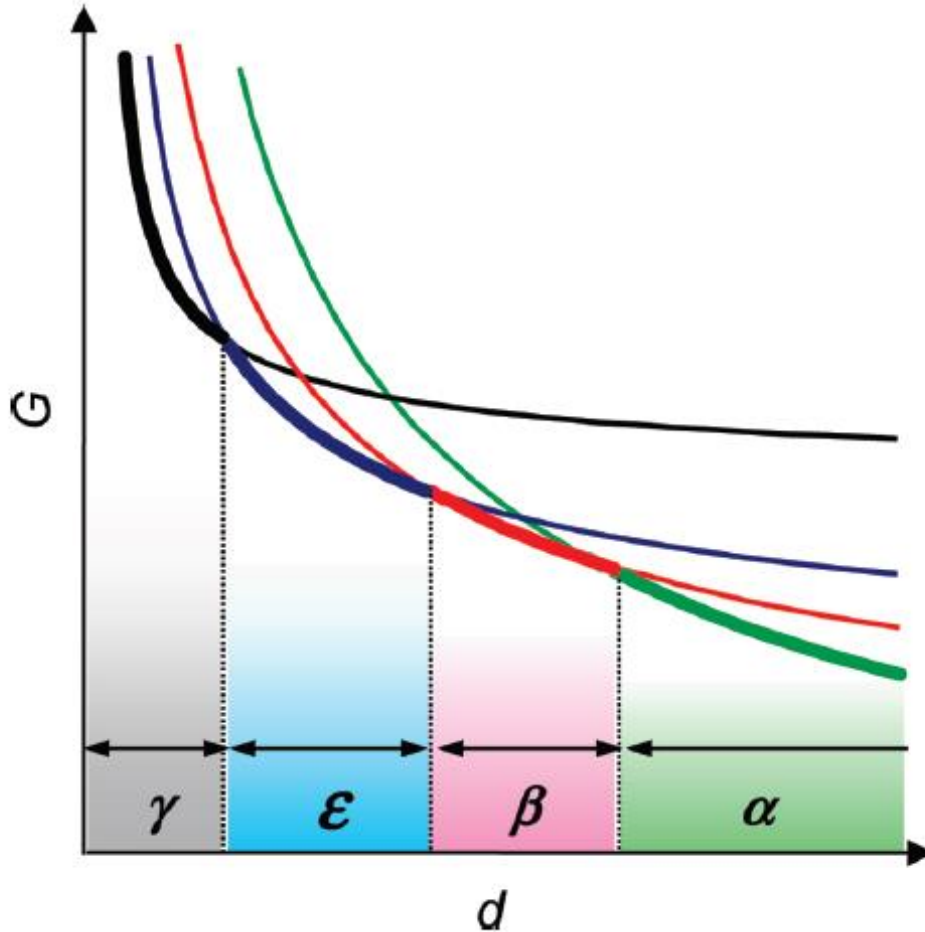


Figure 1.3 Qualitative plot of Gibbs free energy (G) vs particle diameter (d), in which the stability of each Fe_2O_3 polymorph is shown relative to particle size, adapted from [5]

From this prior work, it is possible to lay the foundations for developing a better understanding of the link between grain size/grain growth and crystallographic phase changes and stability, and by controlling the Fe/O diffusion rate to attain the desired grain sizes in the Fe_2O_3 system, one may potentially decouple temperature effects (purely thermodynamic) from size/surface energy effects (kinetics) in determining the most thermodynamically stable phase.

Preferred crystallographic phase transformations in a material system are influenced by a variety of factors, including the initial synthesis method, surface conditions, cation substitutions,

thermal treatment methods, and the surrounding environment[4], [25], [30]–[33]. The thermodynamic stability of phases are typically described in terms of a Gibbs free energy G , the sum of enthalpy H , entropy S , and temperature T .

$$G = H - TS \quad [1.2.1]$$

The enthalpy of a system is the sum of the internal energy U and the product of pressure P and volume V . Gibbs free energy then takes the form

$$G = U + PV - TS \quad [1.2.2]$$

Oftentimes, Gibbs free energy can be written as the sum of a volumetric contribution to free energy G_v and a surface contribution free energy G_s . Since the surface area-to-volume ratio of a system dramatically increased in nanometric systems, the G_s contribution is expected to become a significant determining factor in the overall G of the system.

$$G = G_v + G_s \quad [1.2.3]$$

A comparison of surface area-to-volume ratios for various geometries (as can be found in **Appendix A-4**) shows that the dependence varies as $3/r$ for spherical particles and as $\frac{2}{r} + \frac{2}{l}$ for cylindrical nanorods. From this, it can be seen that at sufficiently small sizes (nanometric size scales) the surface energy becomes a major contributor in determining the free energy. This implies a strong link between particle size and phase stability.

While a simple comparison of Gibbs free energies is typically sufficient to predict phase transformations, this is complicated within the Fe_2O_3 material system due to the relatively small variation in the Gibbs free energies of each polymorph at room temperature[34]. This leads to the coexistence of multiple phases at room temperature and likely at other temperatures as well. Because of this, the exact transformation mechanisms between different polymorphs has been a topic of debate, and is not fully understood. Therefore, the primary focus of this section will be to illustrate prior studies in diffusion-mediated growth and phase stability in the Fe_2O_3 polymorphs.

Generally, to facilitate a crystallographic phase change, a certain amount of energy input (typically heat) is required to sufficiently alter the free energies such that the desired phase becomes most energetically favorable. In addition to the heat required to facilitate a phase change, kinetic effects (such as long-range diffusion) should also be considered[35]–[39]. As previously stated, the free energy of a system is also determined by particle size (the surface area-to-volume ratio), and the contributions of long-range diffusion processes versus short-range crystallographic reorientation to phase stability should be considered. In discussing the phase transformations of Fe_2O_3 , prior work has shown that there is a strong correlation between surface contributions to free energy (a function of particle volume) and phase stability[6], [40]–[42]. Thus, it is important to begin a discussion of crystallographic phase transformations with a discussion of diffusion kinetics which determine the rate of particle growth and the final particle size after treatment at specific temperatures and times. For particle growth to occur, ions must diffuse through some medium, with smaller particles typically being consumed by larger particles in order to minimize the surface energies – hence, a larger particle is typically more stable than a smaller one. Grain growth in crystalline materials occurs in multiple steps, with the growth rate limited by the slowest step: bulk diffusion of solvated ions or molecules to the surface of the crystal, adsorption and diffusion over

the crystal surface, dehydration, dihydroxylation, decharging, and rearrangement of surface ions, integration of ions into the structure, and finally counter diffusion of released solvent from the crystal[4], [35], [37], [43], [44]. Grain growth rates are therefore heavily influenced by both the mobility of the diffusing ions as well as the surface conditions of the crystal. Diffusion of ions during particle growth processes can be considered analogous to a dissolution/reprecipitation process, in which the crystal-growing ions must be in supersaturation within the surrounding medium[4]. Generally, the degree of supersaturation plays a major role in determining the dominant growth mechanism, with nucleation/growth via dislocations dominating under low supersaturation, two-dimensional nucleation/spreading mechanisms being dominant at moderate supersaturation, and crystal surface nucleation dominating in high supersaturations[4]. These aforementioned parameters which are directly related to grain growth can be controlled by changing the initial synthesis method as well as through various interface modification techniques (to be discussed in a later section). These principals regarding grain growth may be extended to general particle growth (involving long-range diffusion processes) as well. In ideal material systems, a diffusion-controlled growth kinetics equation may be applied:

$$d^2 - d_0^2 = kt \quad [1.2.4]$$

where d is the final grain size, d_0 is the initial grain size, t is time, and k is a temperature- dependent constant related to activation energy Q , the and temperature T by an Arrhenius relation:

$$k = k_0 \exp\left(\frac{-Q}{RT}\right) \quad [1.2.5]$$

in which R is the gas constant and k_0 is a rate constant. When the initial grain size is sufficiently small (i.e. a crystal nucleates from solution), d_0 can be approximated to be $d_0 = 0$, and **Eq 1.2.4** becomes a parabolic relation between diffusivity and particle size. From these equations it can be seen that this diffusion kinetics-controlled growth model is a function of initial conditions (d_0 and Q) as well as temperature and time.

While in many cases, it is difficult to decouple particle size from other complex interactions when discussing phase stability, in well-controlled cases, it is found that the diffusion-controlled equations (**Eq. 1.2.4, Eq 1.2.5**) can be fitted to experimental data with remarkable accuracy (to be discussed in detail in a later section). Specifically, the first observation of transformation between four polymorphs of Fe_2O_3 was reported by Sakurai et al, and involved the use of a mesoporous SiO_2 matrix as both nanoreactor sites and diffusion-controlling matrix[5]. While the work described the SiO_2 matrix as a diffusion barrier, the role of the matrix was to facilitate a desirable Fe and O diffusion rate, and shall be referred to as a diffusion-controlling matrix in this work. In the work by Sakurai, et al., grain size and the dominant (majority composition) phase as a function of annealing temperature and times were reported, as shown in **Figure 1.4**, which adapts the data reported in the literature. Magnetic and crystallographic characterization techniques were used to verify the results.

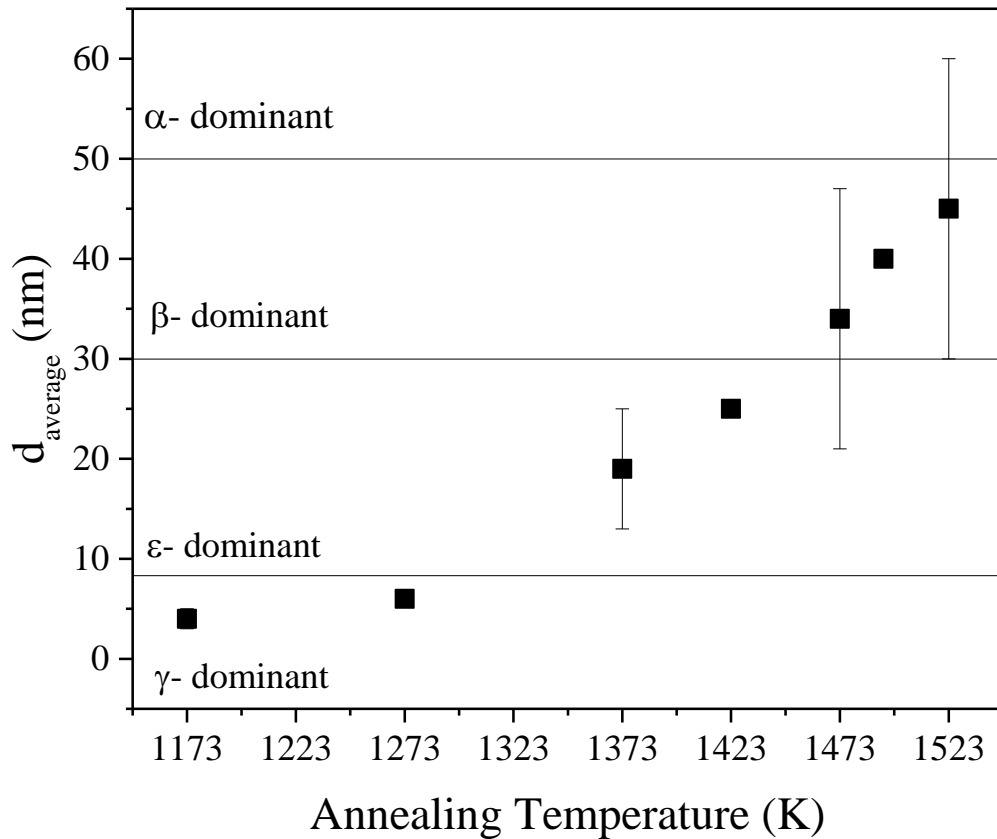


Figure 1.4 Data adopted from [5], indicating phase transformations are primarily size-driven

1.3. Relating Crystallographic Phase and Magnetic Properties

1.3.1. Fundamentals of Magnetic Materials

As previously established, the four polymorphs of Fe_2O_3 exhibit unique magnetic properties due to the different crystal structures. Magnetic properties of a given material can change drastically due a variety of factors, including changes in dimensionality (i.e. quantum dot, thin film, or bulk), volume, morphology (i.e. rod vs sphere), crystallographic defects (dopants, strains, etc.), and environmental effects (pressure, temperature, etc.). To best understand the link

between the crystal structures of Fe₂O₃ polymorphs and their magnetic properties, it is useful to first discuss the basis of magnetism in materials across multiple length-scales.

Intrinsic magnetic interactions in materials arise from the motion of electrons. Specifically, both the spin and orbital of an electron contributes to the total magnetic moment. The spin of an electron is an intrinsic property of electrons, and thus the magnetic moment is a constant value ($\mu_{spin} = 9.27 \times 10^{-21} \text{ emu}$). The orbital moment on the other hand, may be considered analogous to that of a field generated by a current owing to the electron orbit about the nucleus being a moving charge. This allows for the moment associated with an orbiting electron can be formulated as:

$$\mu_{orbit} = \frac{evr}{2c} \quad [1.3.1]$$

where e is the electron charge, v is velocity in circular orbit, r is the radius of the orbit, and c is the speed of light. In the first Bohr orbital, the orbital moment is found to be

$$\mu_{orbit} = \frac{eh}{4\pi mc} \quad [1.3.2]$$

where h is Planck's constant, and m is the rest mass of the electron, which is found to be equal to spin moment, giving the fundamental unit for a magnetic moment, the Bohr magneton ($\mu_B = 9.27 \times 10^{-21} \text{ emu}$)[2], as illustrated in **Figure 1.5**.

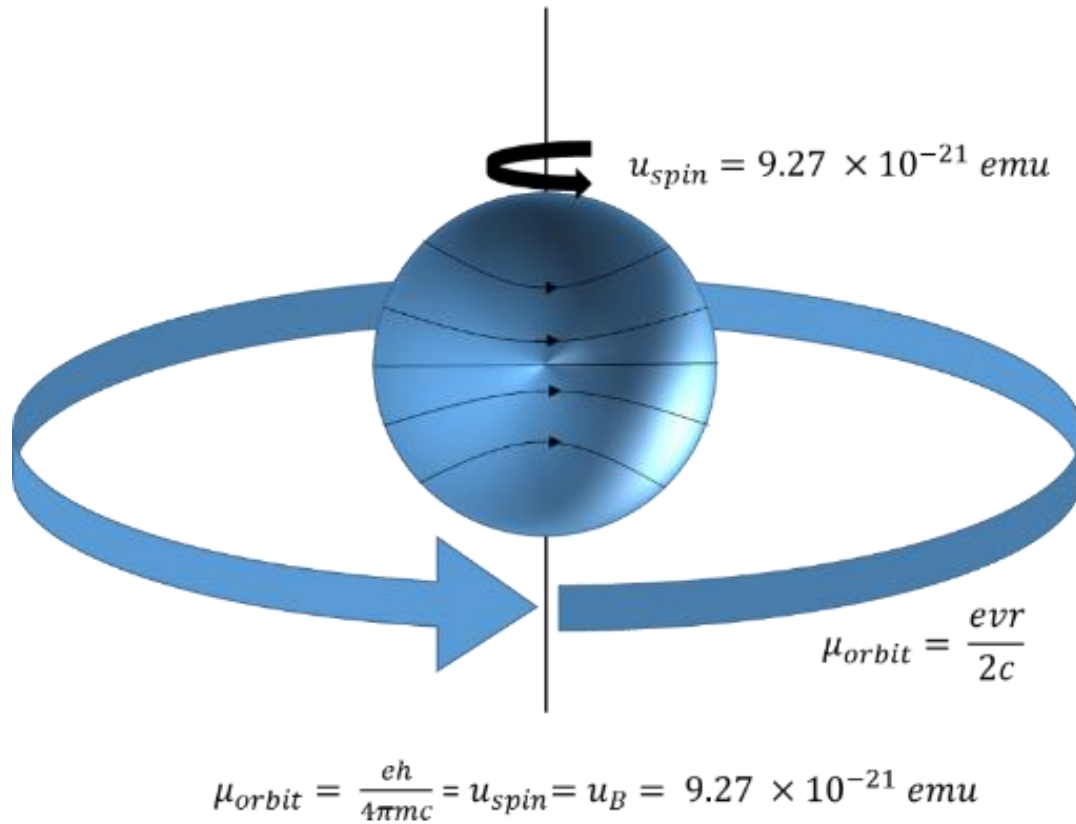


Figure 1.5 Magnetic moments attributed to the electron spin and orbit at the first Bohr orbital give the Bohr magneton (μ_B), a fundamental unit for magnetic moment

While a magnetic moment is a fundamental component in all electrons, and all materials will exhibit some interaction with external magnetic fields, only certain materials exhibit ferromagnetism, or can be considered permanent magnets. To better understand magnetic properties of materials, it is useful to first link the magnetic moment of a single electron (μ_B) to the magnetic domains found within materials. The net moment of a single atom is dependent on the number and arrangement (individual spins and orbits) of the constituent electrons. From this, an atom may exhibit either no net magnetic moment due to the cancellation from opposing spins, or a net magnetic moment from an incomplete cancellation (unpaired electron) of opposing spins[2]. There are a select few elements which typically exhibit ferromagnetic properties – some

transition metals (Ni, Fe, Co) and rare-earth elements (Gd, Tb, Dy). Within a crystal lattice (typically comprised of several atoms), the net moment depends on both the constituent atoms (whether the atoms can inherently exhibit a net moment) and the symmetry of the structure. Typically, a less symmetric (higher anisotropy) lattice will be more likely to exhibit a net magnetic moment. From the single crystal lattice, individual grains (multiple ordered and connected lattices) in a polycrystalline material may form. Depending on the size of the individual grains, one or more magnetic domains may form within the grain, as shown in **Figure 1.6**. While an individual electron is orders of magnitude smaller than an atom, and several atoms comprise a single lattice, the size scales of magnetic domains and crystallites or grains can vary drastically. When the grain size is the same size or smaller than the single domain size of a magnetic material (known as the critical radius), a material may exhibit superparamagnetic behavior. Conversely, a grain that is very large may contain many magnetic domains which may not necessarily align in the same direction[45].

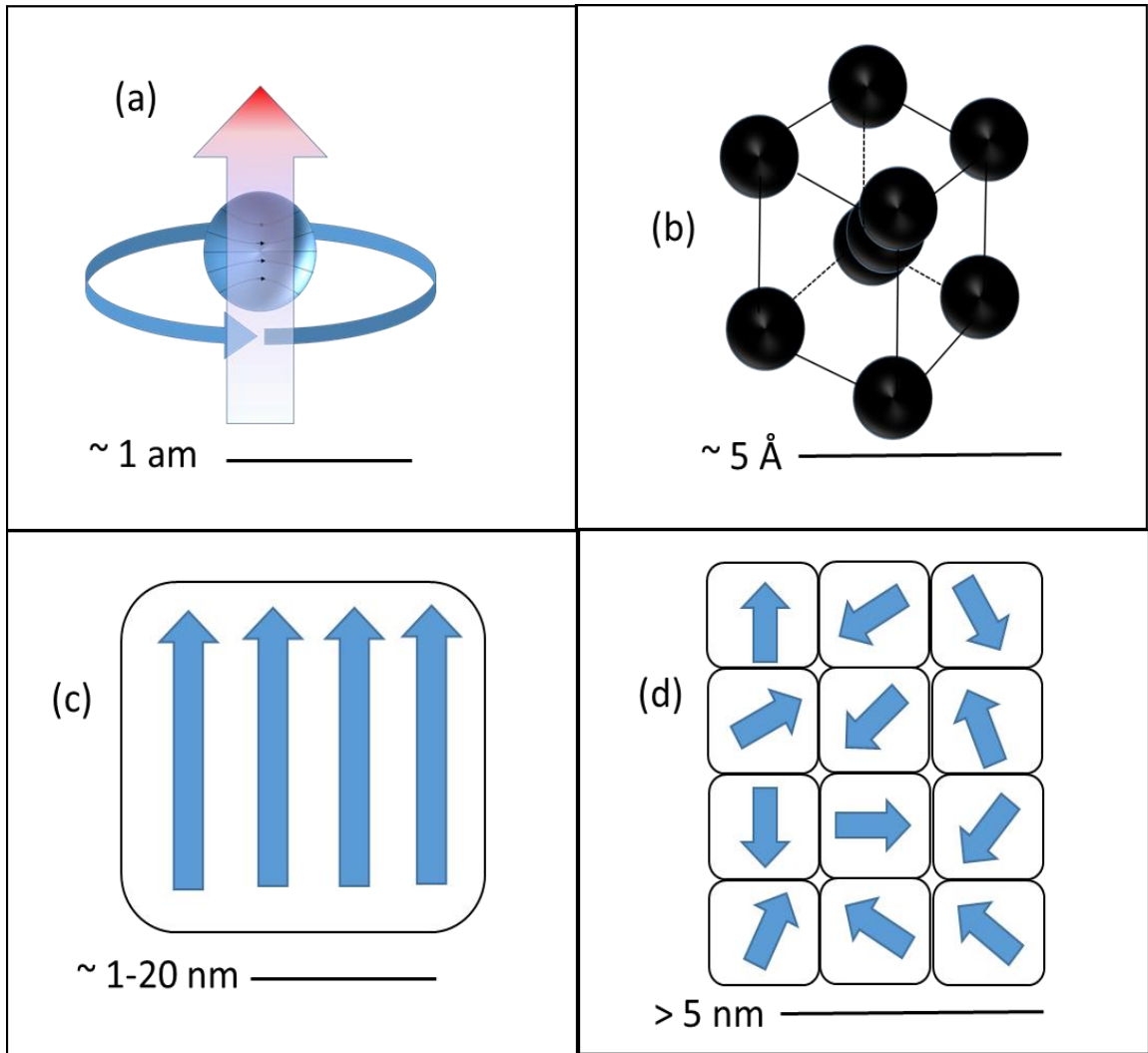


Figure 1.6 (a) moment from an electron, also known as a Bohr magneton (b) size scale of a crystal lattice (c) size scale of a magnetic domain (d) domains within a single grain

Along with a general understanding of the size scales relevant to magnetic properties, it is also useful to understand the energies associated with magnetic materials, which can provide insight for understanding and designing desirable properties in magnetic materials. The resulting behavior of a magnetic material can be predicted by the sum of the various energies involved, which include the stray field (E_{stray}), the exchange energy ($E_{exchange}$), the magnetocrystalline anisotropy ($E_{anisotropy}$), external field effects ($E_{external}$), surface effects, and other energies (i.e.

thermal energy)[2], [45], [46]. The stray field is the external field generated by a magnetic material, and can be considered the demagnetizing field which arises in order to counteract the internal moments of the material and lower the total magnetic moment. The stray field energy can be presented as:

$$E_{stray} = -\frac{1}{2}\overrightarrow{H_d}\overrightarrow{M} \quad [1.3.3]$$

where H_d is the demagnetizing field that is generated by the material, and M is the internal magnetization. Beyond simple geometries, the exact stray field energy becomes difficult to calculate. An exchange interaction describes an interaction between two neighboring atomic moments, in which the moments couple to align either parallel or antiparallel. The exchange energy is typically described as

$$E_{exchange} = A \left(\frac{d\varphi}{dx}\right)^2 \quad [1.3.4]$$

Where A is the material-dependent exchange constant, and $\frac{d\varphi}{dx}$ describes the rate of local magnetization rotation over length at the domain wall. Another intrinsic energy is the anisotropy energy, which is dependent on the total anisotropy of a material (including magnetocrystalline, surface, magneto-elastic, and shape anisotropies). Because an unpaired moment which is capable of retaining alignment is necessary for materials to exhibit a permanent magnetic response, most magnetic materials have anisotropic crystal structures, and therefore have a preferred direction of magnetization (known as the easy axis). In thin films (ranging from a single to several atomic layers), surface anisotropy must be considered because a significant portion of the moments are at

the surface and therefore do not have the same interactions in all directions as in bulk materials. As with many material properties, strains on a crystal lattice will also affect spin-orbit interactions. In heavily strained lattices, a magneto-elastic anisotropy arises which may play a significant role. Within bulk magnetic materials (\geq millimeter sized), the shape anisotropy begins to dominate. In a bulk magnet, the majority of moments are contained within the volume and preferentially align to minimize internal energy, which is determined by the direction which contains more moments to align with. Hence, the stray field geometry in a bulk magnet may be manipulated by utilizing shape anisotropy (i.e. a bar magnet vs a disc vs a horseshoe). The total anisotropy energy is determined by the sum of these individual anisotropy values:

$$E_{anisotropy} = K_{effective}(\sin\theta)^2 \quad [1.3.5]$$

$$K_{effective} = (K_{shape} + K_{magnetocrystalline} + K_{magneto-elastic}) + \frac{2K_{surface}}{t} \quad [1.3.6]$$

where K_{shape} , $K_{magnetocrystalline}$, $K_{magneto-elastic}$, and $K_{surface}$ are the anisotropy constants associated with each anisotropy effect, t is the thickness of the thin film, and θ is the angle between the magnetization direction and the easy direction of the material. For the purpose of general discussion of non-thin film materials, the anisotropy energy which arises from the K_{shape} , $K_{magnetocrystalline}$, $K_{magneto-elastic}$ terms can be summarized as a volumetric anisotropy energy ($E_{vol-anisotropy}$) The final energy to be considered is the energy associated with an externally applied magnetic field. This value is simply described as

$$E_{external} = -\vec{H} \cdot \vec{M} \quad [1.3.7]$$

where H is the external field and M is the magnetization value. The total magnetic energy associated with a single magnet is the sum of these energies:

$$E_{total} = \int_{vol} (E_{external} + E_{exchange} + E_{stray} + E_{vol-anisotropy}) dV + C \quad [1.3.8]$$

The value of C is the additional energies which may arise from surface anisotropy, thermal fluctuations, etc. [2], [45], [46]. In summary, the structures in a magnetic material (grain size, morphology, crystal structure, etc.) play significant roles in determining the net properties.

1.3.2. Properties of Permanent Magnetic Materials

Understanding the foundations of magnetic interactions within materials allows for definition of different types of magnetism within materials. The first and most common of these types of magnetism is diamagnetism. A diamagnetic response arises from the interaction between an external magnetic field and an orbiting electron, in which the electron may be considered as a moving charge which generates an opposing moment in response to the external field. This effect is seen in all materials, but is generally a very weak response with negligible effect on the external magnetic field. While diamagnetic interactions are strongly overshadowed by the response of unpaired moments, the vast majority of materials contain fully paired moments, and thus are considered to be diamagnetic. Paramagnetism is a common magnetic interaction in which a material contains a large amount of unpaired moments which are distributed such that they do not interact and retain alignment, essentially behaving as “free” moments. Paramagnetic materials

typically magnetize linearly (until saturation) with an external field, but do not retain any alignment under zero field.

Ferro/ferrimagnetic and antiferromagnetic materials are typically considered to be permanent magnetic materials. Ferromagnetic materials are the classical magnetic material, in which the crystal structure consists of many unpaired moments which can be aligned and retain their alignment. Ferrimagnetic materials behave similarly to ferromagnetic materials, except they have some moments aligned in directions opposing the majority of the moments, meaning the material can be magnetized, but will always have some percentage of opposing moments. Antiferromagnetic materials (such as hematite) are materials in which the crystal structures contain unpaired moments, but are distributed antiparallel throughout, such that the flipping of one moment will be counteracted by the flipping of another moment. Most materials that are considered antiferromagnetic are in fact slightly canted (the moments are not perfectly antiparallel) at room temperature, and thus can display a slightly ferromagnetic behavior. Each of the aforementioned magnetic behaviors exhibit different interactions with external fields and should therefore be expected to exhibit vastly different hysteresis, as shown in **Figure 1.7**.

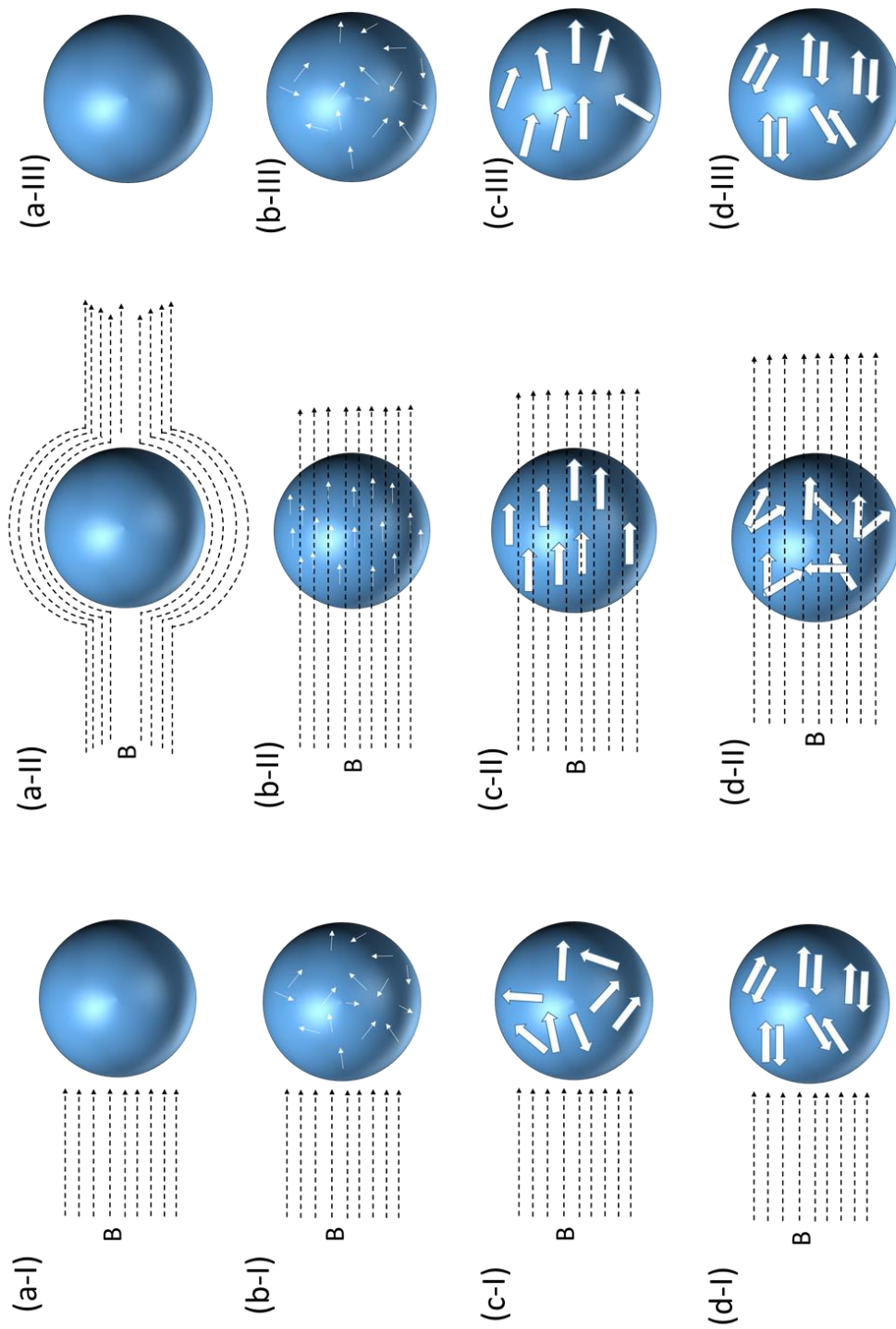


Figure 1.7 Magnetic moment behavior in bulk materials before (a-I, b-I, c-I, d-I), during (a-II, b-II, c-II, d-II), and after (a-III, b-III, c-III, d-III) application of an external magnetic field in diamagnetic (a), paramagnetic (b), ferromagnetic (c), and antiferromagnetic (d), respectively

When discussing permanent magnets, several properties should be considered in order to best characterize the overall strength of the magnet. In permanent magnets, the coercivity (H_c), remanence (M_r), saturation (M_s), and energy product (BH_{max}) are typically the values of most concern. The M_s is the maximum magnetization a material can reach under the influence of an externally applied field, in which all of the moments are fully aligned. The M_r is the amount of magnetization that remains without any applied field, and is an indicator of the potential total stray field that the material can produce. The H_c is the amount of externally applied field required to demagnetize the material, and is an indicator of the how resistant the material is to demagnetization. Hard and soft magnets are general terms used to describe the overall behavior of a magnet, with hard magnets exhibiting high H_c values and soft magnets exhibiting high M_r values but low H_c values. The BH_{max} is a figure of merit which indicates the overall strength of a permanent magnet, being a product of the magnetic flux density (B) and the coercivity (H) of a material. These values can be determined with a magnetic hysteresis ($M-H$) loop. In addition to these properties, magnetic moments in a material also undergo restructuring and reordering at various temperatures. At sufficiently high temperatures, thermal energy will overcome the magnetic ordering and a magnetic material will begin behaving as a paramagnet. This is known as the Curie Temperature (T_c) in ferro/ferrimagnetic materials, and the Neél temperature (T_N) in antiferromagnetic materials. At temperatures below room temperature, magnetic structure rearrangements can also occur in materials, (such as the blocking temperature T_B in paramagnets and Morin transition T_M in antiferromagnets), with the resulting magnetic behavior and transition temperatures being largely dependent on the phase (crystal structure) of the material. The temperature at which these magnetic reordering phenomena occur in a material can change based on particle size and/or significant defects in a crystal structure or particle surface[4], [15]. An

example is in the skewing of the Morin transition temperature in hematite particles. While early reports stated that particle size was the determining factor in the change in transition temperature, later reports disputed this by showing that while particle size was a factor, it was primarily surface energies (particle size, surface defects, etc.) that determined the change in transition temperature (smaller particles inherently have higher surface area to volume ratios). In sufficiently small particles (typically tens of nanometers or smaller), the particle size may become smaller than the single domain size, and there is not enough internal magnetic energies to maintain magnetic ordering. At this point, the magnetic moments begin to flip spontaneously from thermal excitation, and is known as superparamagnetic, due to the resulting magnetic behavior being very similar to conventional paramagnetic materials[46]–[48].

1.3.3. Magnetic Properties of Fe₂O₃ Polymorphs

Having established the basics of magnetism and the relevant concepts for bulk magnetic materials, it is possible to discuss the link between crystal structure and magnetic properties of the Fe₂O₃ polymorphs. The ferrimagnetic behavior of γ -Fe₂O₃ can be attributed to it being a cubic iron oxide phase (inverse-spinel structure), similar to Fe₃O₄ (magnetite). In fact, the magnetic properties as well as X-ray diffraction patterns are remarkably similar and sometimes indistinguishable[4], [16], [49]. The inverse-spinel structure of γ -Fe₂O₃ contains Fe³⁺ ions at two separate octahedral and tetrahedral sites and is ferrimagnetic at room temperature, with (mass normalized) M_s values reported as 60-80 emu/g and H_c typically below 200 Oe. It exhibits a blocking temperature (the temperature in which the Néel relaxation time of a superparamagnet becomes slower than the measurement time) reported between 20-60K, and a T_c around 800-900K. However, the T_c has been variously disputed because γ -Fe₂O₃ is typically a nano-sized phase, and

begins to exhibit significant grain growth and a resulting phase transformation towards the more stable α -Fe₂O₃ at temperatures above 500K unless the particles are isolated and well-constrained to prevent grain growth[16], [30], [50], [51].

By growing γ -Fe₂O₃ under well-controlled conditions, it is possible to isolate the second metastable polymorph, ε -Fe₂O₃. ε -Fe₂O₃ is a metastable polymorph and readily converts to α -Fe₂O₃ at temperatures above 500K when the individual particles are unrestricted. Despite this thermodynamic metastability, much work has been devoted to synthesizing and isolating as a pure phase due to the unique magnetic properties[26], [27], [52]–[56]. As previously described, the orthorhombic, non-centrosymmetric crystal structure is comprised of four distinct Fe sites, which in turn gives rise to unique magnetic properties due to the four different sublattice magnetizations, and has been described as either a heavily canted antiferromagnet or a non-collinear ferromagnet. The magnetocrystalline anisotropy has been reported as $K = 2\text{--}5 \times 10^5 \text{ J/m}^3$, with a M_s between 15–25 emu/g[27]. It has been shown to exhibit very high H_c values, ranging from 12 to over 20 kOe, with variation depending on phase purity, morphology, and synthesis method[10], [27], [53], [54], [57]–[59]. Work by Ohkoshi, et al.[60] sought to determine the exact origins of the high H_c by modeling the sublattice magnetic exchange behavior using molecular field theory. In the model, it was shown that the magnetic ordering is driven by antiferromagnetic superexchange. The single tetrahedral Fe site exhibits a lower sublattice magnetization than the three octahedral Fe sites (as shown in **Figure 1.8**), leading to a small ferromagnetic component. This allows for the ε -Fe₂O₃ phase to be magnetized under sufficiently high fields while retaining a high H_c due to the antiferromagnetic exchange component. For this reason, ε -Fe₂O₃ has been described as both a canted-antiferromagnet and a non-collinear ferromagnet.

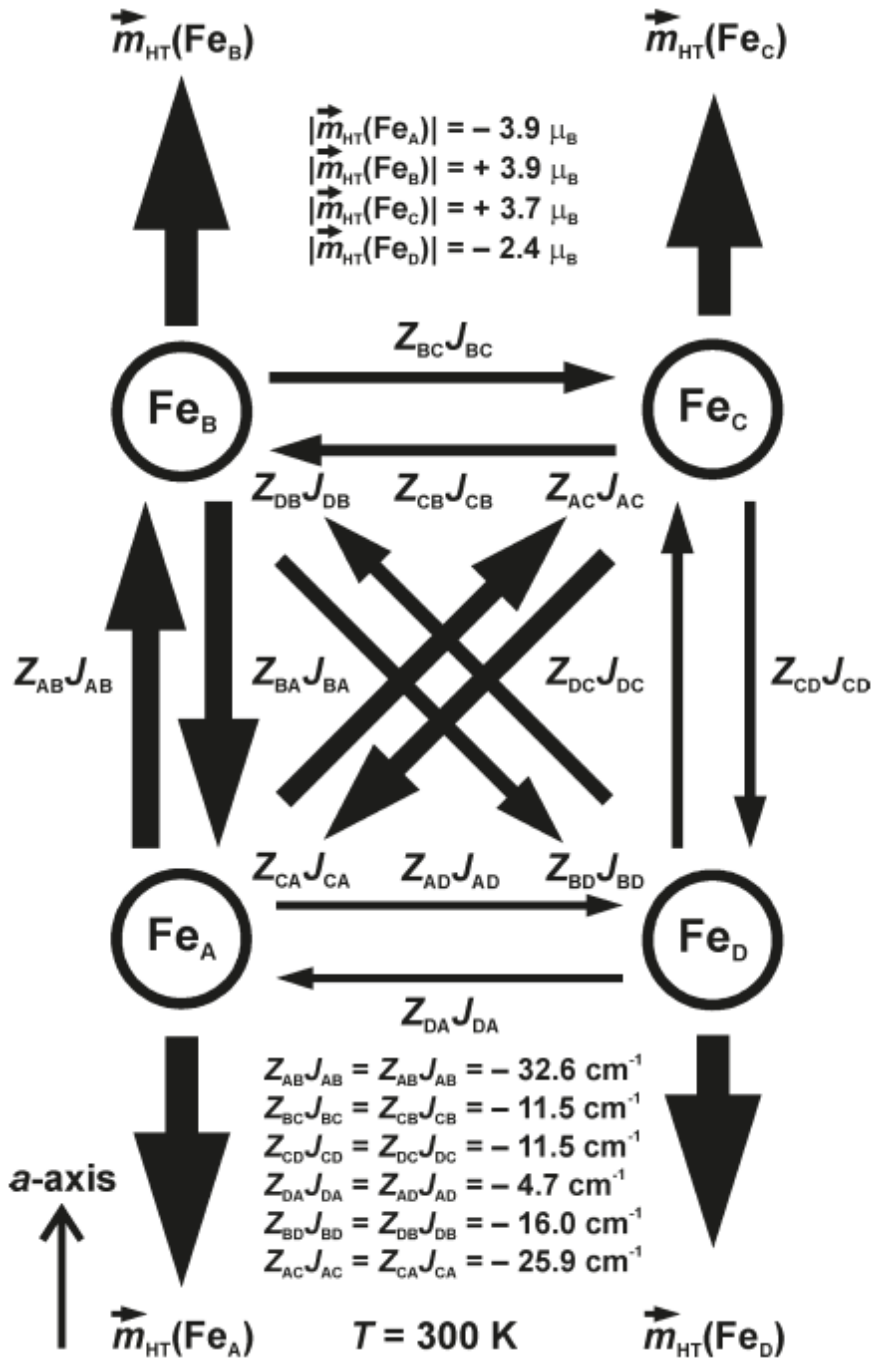


Figure 1.8 Sublattice exchange diagram demonstrating the antiferromagnetic sublattice exchange between the four sublattices, with the uncompensated ferromagnetic component due to the tetrahedral site., adapted from [27]

Due to the complex sublattice exchange structure, ϵ -Fe₂O₃ also exhibits interesting magnetic transitions at various temperatures. It has been reported to have a T_c (or T_N) as low as 490K, with a tendency to transform to α -Fe₂O₃ at higher temperatures unless the particles are heavily segregated and constrained. It also undergoes two separate magnetic structural reorderings at low temperatures, with the first occurring between 110-150K and is analogous to the Morin transition seen in α -Fe₂O₃[5], [27], [61]. This Morin-like transition is marked by the gradual increase in moment as temperature is lowered from the T_c , before the magnetic structure reorders from a canted antiferromagnet to a true antiferromagnetic structure below 150K and exhibits a rapid drop in magnetization. A second transition occurs below 80K, with the magnetization increasing down to 2K, as it reorders into a second canted state. Because of the high coercivity and unique magnetic structure transitions related to the complex crystal structure, the magnetic properties of ϵ -Fe₂O₃ may be used as strong indicators of the phase purity.

Upon growing ϵ -Fe₂O₃ further, a third phase is stabilized, known as β -Fe₂O₃. The β -Fe₂O₃ phase is difficult to synthesize as a pure phase, due to the small size range in which it is most stable, and often co-exists with other polymorphs, such as ϵ -Fe₂O₃ or α -Fe₂O₃. Due to the difficulty of synthesizing as a pure phase, the magnetic properties of β -Fe₂O₃ have not been as heavily studied as the other three phases. Due to the low T_N (100-117K), the magnetic behavior has been described as either antiferromagnetic (below 117K) or paramagnetic (above 117K to 500K)[11], [62], [63]. At temperature above 500K, even in well-controlled cases, β -Fe₂O₃ is difficult to isolate as a pure phase, and preferentially transforms to the most stable iron (III) oxide polymorph, α -Fe₂O₃.

α -Fe₂O₃ (commonly known by the mineral name hematite) is typically considered to be the end product of the series of Fe₂O₃ phase transformations during grain growth, and is the most

stable as well as most common naturally occurring polymorph. The magnetic behavior is typically described as antiferromagnetic, but exhibits a slight canting at 300K, leading to a slightly ferromagnetic component. Due to the slight canting related to the hexagonal-like crystal structure, the H_c and M_s of hematite are typically quite low (less than 500 Oe and about 0.3 emu/g respectively)[4]. Hematite transitions to a paramagnetic state at 600-700K, considered as the T_c or T_N . These terms may be used interchangeably because the slightly canted antiferromagnetic structure of hematite gives rise to a slightly ferromagnetic behavior. At low temperatures, the Morin transition has been reported as varying from 200K to 260K. The reason for the variation in temperature has been attributed to either an effect arising directly from grain size (with smaller grains leading to a lower Morin transition temperature) or surface defects associated with the decrease in grain size (altering surface energies)[14], [15]. Additionally, superparamagnetic particles of hematite have been synthesized, with 8-16 nm grain sizes reported and a blocking temperature (transition from paramagnetic to weakly ferromagnetic) of 117 ± 5 K[4]. The magnetic properties of the Fe_2O_3 polymorphs are intrinsically linked to the phase and crystal structure, and thus exhibit vastly different magnetization vs field (magnetic hysteresis) loops (**Figure 1.9**).

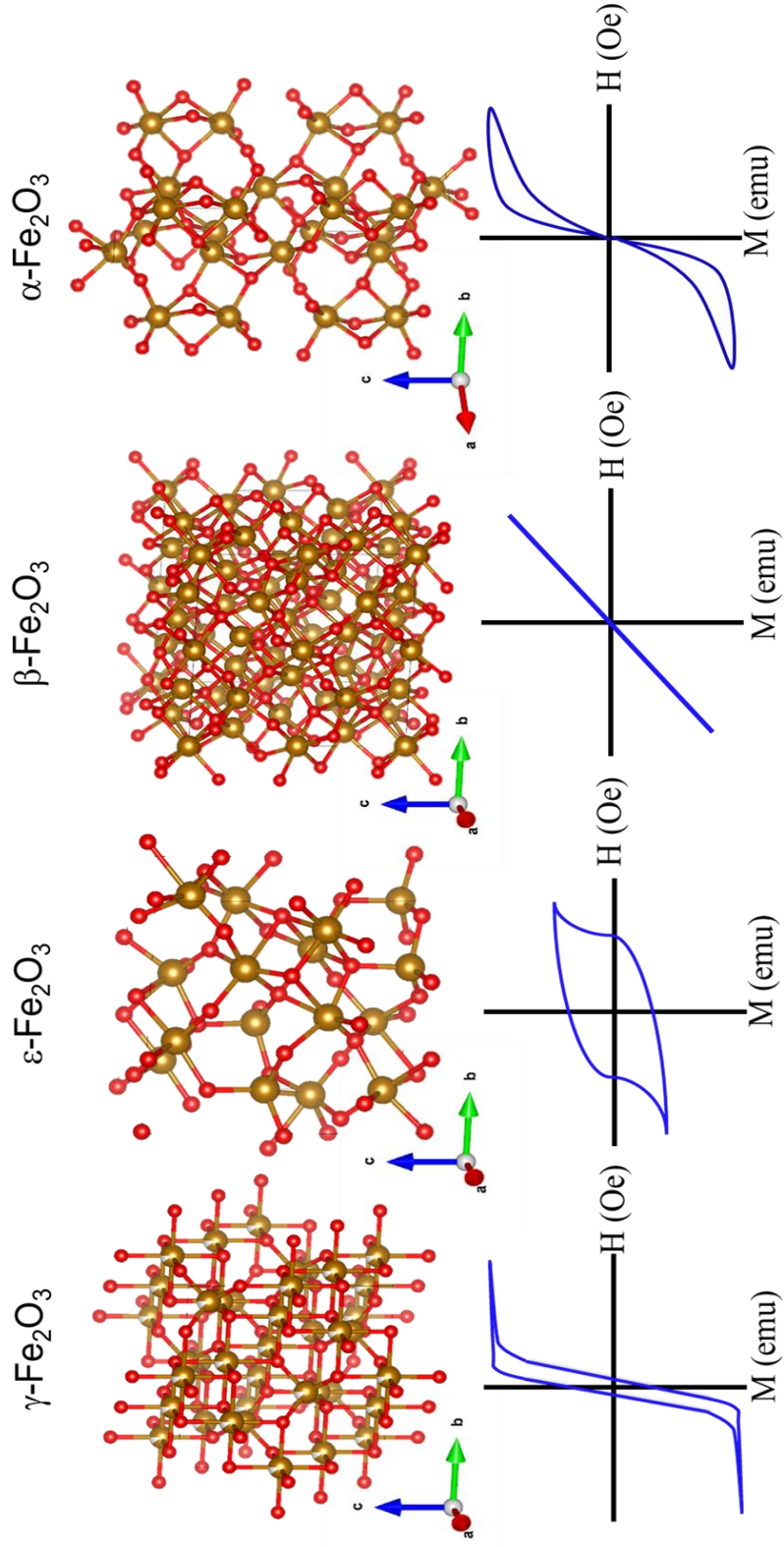


Figure 1.9 Crystal structure and expected magnetic hysteresis behavior of each Fe_2O_3 polymorph.

It should be noted that while the phase stability of the different Fe_2O_3 polymorphs has been presented as a size-dependent function, the close free energies of the different phases may lead to the coexistence of multiple phases under the same conditions, and the existence of superparamagnetic hematite particles may be considered to be a metastable state. The unique magnetic properties of the Fe_2O_3 phases arise from the distinct crystal structures, and therefore exhibit different magnetic structural transitions due to temperature change. **Figure 1.10**, adapted from Sakurai, et al.[5] shows the magnetic transitions during field cooling for each phase. Field cooling is useful for determining the magnetically dominant phase in a material.

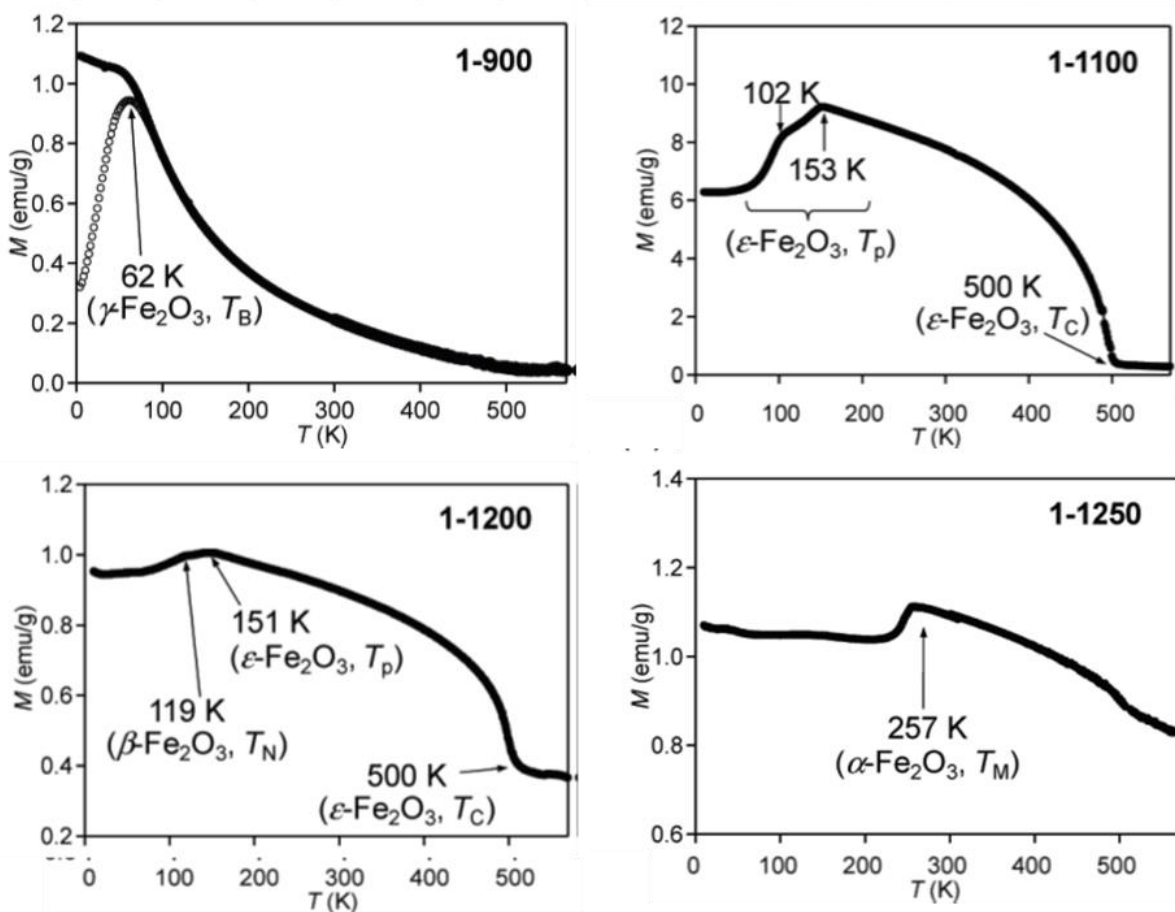


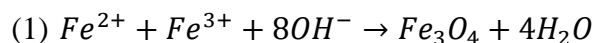
Figure 1.10 Field cooling curves from [5], demonstrating the different magnetic responses of each polymorph to temperature

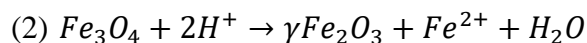
2. SYNTHESIS AND PROCESSING OF BULK AND POWDER Fe₂O₃

2.1. Prior Work on Chemical Synthesis Methods for Fe₂O₃ Powder

With the abundance and importance of magnetic materials in modern technology, a wide range of chemical synthesis techniques have been developed for production of high-purity Fe₂O₃ nanoparticles in various morphologies for many applications. Commonly used chemical synthesis routes for Fe₂O₃ nanoparticles include: co-precipitation, hydrothermal/high temperature reactions, sol-gel reactions, flow injection synthesis, electrochemical synthesis, aerosol/vapor synthesis, and sonolysis[64]. The choice of synthesis technique is heavily dependent on application (i.e. use as a nanoparticle vs bulk material, phase control, etc.), and a variety of factors may make one technique more desirable or require a combination of processes. The following section aims to highlight the differences between the aforementioned synthesis techniques and provide insight into the choice of synthesis and processing techniques used in this work, with an emphasis on the understanding and control of the nucleation and growth kinetics in order to attain the desired phase and morphology.

Co-precipitation is heavily used in many synthesis techniques due to the simplicity and high efficiency. Co-precipitation is a classic chemical synthesis technique in which the cation source, typically a salt such as Fe(NO₃)₃, is dissolved in an aqueous solution and allowed to oxidize, either by ageing in air or by some electron/ion transfer process (i.e. adjusting the pH). An example of co-precipitation for synthesis of iron oxide nanoparticles involves the dissolution of ferric salts followed by oxidation of cations to form the metal-oxide particles[64], [65]:





A co-precipitation process relies on the ease of dissolution of ionic salts in aqueous solution and the metal oxide formation being the naturally energetically favorable process. An advantage of such a process is that a large quantity of material can be relatively quickly synthesized with low energy input. However, tunability of particle size and morphology with a purely co-precipitation process is difficult due to the uncontrolled kinetics during the process. A typical co-precipitation process involves rapid nucleation of a crystal site when the reactants reach a critical supersaturation, followed by diffusion-controlled grain growth[41], [64]. In unconstrained environments, uniform distribution of the ions is difficult to achieve, and the nucleation/growth kinetics occur readily, leading to poor control of size distribution and sometimes results in unpredictable morphology. A greater degree of control over particle size and shape can be achieved by adjusting pH, temperature, or the starting materials (type of salt or solution), but in the absence of a constraining environment, size and shape distribution control is still relatively poor. Various other experimental factors may also contribute, such as mixing time, kinetics of mixing, etc. To reliably achieve small size and shape distributions of particles, a constraining matrix may be introduced to separate the initial nucleation from the particle growth and inhibit the diffusion kinetics that would normally lead to the size and shape disparity.

While co-precipitation processes are typically low energy and carried out at or near room temperature, hydrothermal/high temperature reactions of nanoparticles typically require high pressure and temperatures significantly higher than room temperature. Either hydrolysis and oxidation or neutralization of metal hydroxides provide the basic chemical reaction, but the processes are carried out in sealed reactors (such as an autoclave) at high temperatures, leading to pressures in excess of 2000 psi within the reaction vessel[64], [66], [67]. In such processes, the

particle shape and size are heavily dependent on both the time and temperature. As with coprecipitation, the size and shape of the particle is largely determined by the rate of nucleation and growth. In the case of hydrothermal synthesis, the nucleation and growth is controlled by the temperature and time, with longer times typically resulting in larger particles.

A sol-gel reaction is a wet chemistry synthesis route named for the solution-to-gel process. Sol-gel processes involves the hydroxylation and condensation of particles inside a solution, in which a precursor is suspended or dissolved in a solution (either water or alcohol) and is then activated by a change in pH (addition of an acid or base). The activated precursor then forms either a colloid or polymeric chain, and transitions from the solution state to a coherent network with some excess liquid (gel)[64], [68]. Following the formation of a gel, subsequent heat-treatment is necessary to complete the reaction and remove excess organic material to obtain the desired pure phase. Through purely sol-gel synthesis, small particle sizes (<15nm) have been demonstrated by careful selection of the reactants, surrounding environment, and heat treatment process. Some advantages of sol-gel processes are increased control over particle size, the ability to obtain amorphous phases, and greater control over morphology. This controllability and tunability can be further increased when a sol-gel process is used to form a constraining matrix during coprecipitation of Fe₂O₃ nanoparticles, essentially forming nanoreaction sites as well as a diffusion barrier to control the nucleation and growth processes[26], [67]–[70].

Flow-injection synthesis of uniform, nano-sized magnetite particles was demonstrated by Salazar-Alvarez, et al.[64], [71]. The flow-injection process replaces the use of a conventional matrix (as in sol-gel processes) with injection of reagents under laminar flow. The reagents are flowed either continuously or through various segments which serve as reaction vessels, and then collected at the end. A system can be configured to allow for simultaneous processes, giving a

high degree of modularity and controllability over the particle size and shape distribution and can potentially improve the efficiency of the chemical synthesis. Aerosol/vapor synthesis methods are similar in concept, in that the constraining matrix for controlling particle nucleation and growth is replaced with an alternative method. Unlike flow-injection, however, aerosol/vapor synthesis techniques involve dissolving ferrite salts into some solvent, and is then sprayed into reactors where the solvent is allowed to dry, and the powder residue is collected. The resulting particle size is dependent on the initial droplet size[64]. The aforementioned synthesis techniques may also be used separate or in conjunction with electrochemical processes. An application of an electric bias during synthesis has been demonstrated to affect the resulting particle size and shape[30], [64].

Synthesis of iron oxide nanoparticles can also be achieved via thermal or sonic decomposition of organometallic precursors. Sonolysis involves the use of ultrasonic agitation on some iron oxide precursor solution to generate bubbles via cavitation. The collapse of these cavitation sites can generate high energy hotspots which lead to the rapid decomposition and conversion of the precursor to nanoparticles. Through such sonolysis techniques, superparamagnetic nanoparticles have been reported. However, due to the relatively high energy involved, there may be some loss in controllability and tunability of particle sizes and shapes.

2.2. Overview and Prior Work on Chemical Synthesis of ϵ -Fe₂O₃/SiO₂ Precursor Powders

The aim of this work is to first reliably control the formation and understand the mechanisms for stability of metastable Fe₂O₃ polymorphs, then to utilize the unique magnetic properties of the metastable phases as bulk, functional, nanocomposite magnets. Specifically, the reliable and controllable synthesis of ϵ -Fe₂O₃ is desired due to the abnormally high H_c which had been previously demonstrated[24], [27], [53], [72]. To achieve desirable properties in the bulk form, the powders used must be highly uniform in size, shape, and morphology. While some alterations to both synthesis and processing techniques were necessary to achieve different goals, the precursor powders used in this work were synthesized with the same reverse-micelle/sol-gel process adopted from Sakurai, et al.[25], [73].

The reverse-micelle/sol-gel process utilizes reverse-micelles as a constraining matrix in the initial nucleation of the iron oxide-precursor core, followed by the formation of a silica shell as the primary growth-inhibiting matrix. A micelle is comprised of some reactant dissolved in an oil phase then mixed with a surfactant and a water phase. The hydrophobic tail of the surfactant then preferentially aligns away from the water phase, encapsulating the oil/reactant mixture into small spheres (**Figure 2.1a**). However, because the ferric salts dissolve in the water phase and not the oil phase, reverse-micelles must be used in place of micelles as nano-reactor vessels. In function, the reverse-micelle achieves the same goal, as hydrophilic heads preferentially align towards the cation-containing water phase and the hydrophobic tails align towards the oil phase (**Figure 2.1b**).

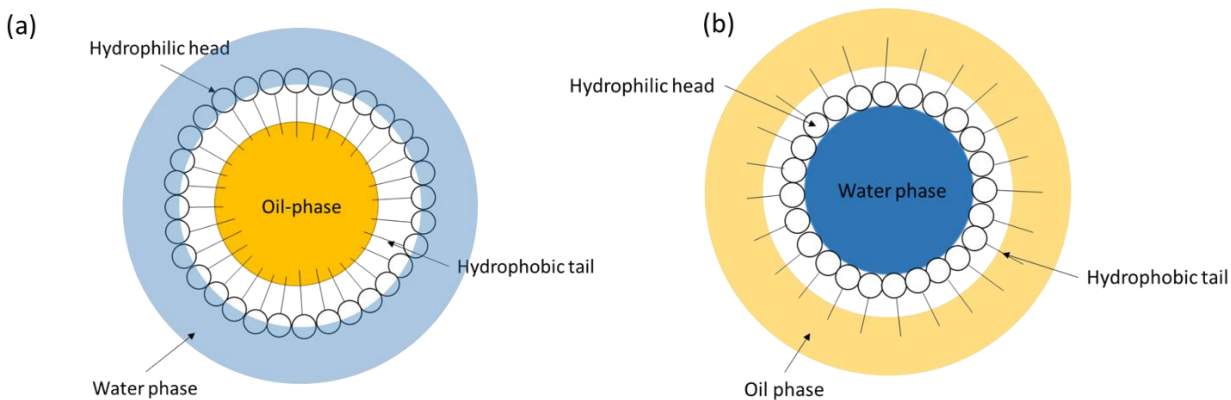
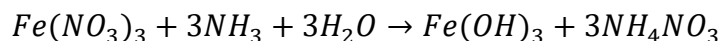


Figure 2.1 Structure of micelle (a) vs reverse-micelle (b) – the polar nature of the surfactant preferentially organizes to minimize surface energies, with the ratio of water to oil phase as the primary determining factor for micelle vs reverse-micelle formation

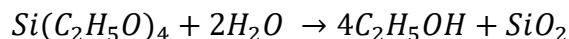
The polar nature of the surfactant leads to the micelle/reverse-micelle formation in order to minimize the surface energies. By adjusting the water-to-oil ratio, it is possible to form either micelles or reverse-micelles.

Figure 2.2 illustrates the chemical synthesis process and the resulting nanorod structure. The synthesis procedure involved the preparation of two separate reverse-micelle solutions. One solution (solution A) contained 0.74 mmol $\text{Fe}(\text{NO}_3)_3$ (iron nitrate), 0.074 mmol of $\text{Ba}(\text{NO}_3)_2$ (barium nitrate), and 330 mmol H_2O (ultra-pure water). After mixing to fully dissolve the salts in water, the solution was added to an oil/surfactant mixture consisting of 9.77 mmol of cetyltrimethylammonium bromide (CTAB), 39 mmol of $\text{C}_4\text{H}_9\text{OH}$ (Butyl alcohol), and 110 mmol C_8H_{18} (n-octane) and a reverse-micelle solution containing the cation source is formed. The second solution (Solution B) consisted of an initial mixture of 30 mmol NH_4OH (ammonium hydroxide) and 330 mmol H_2O (ultra-pure water), which was stirred to fully mix, then subsequently mixed into an oil/surfactant mixture consisting of 9.77 mmol of cetyltrimethylammonium bromide (CTAB), 39 mmol of $\text{C}_4\text{H}_9\text{OH}$ (Butyl alcohol), and 110 mmol C_8H_{18} (n-octane) to form the second

reverse-micelle solution. Upon formation of the reverse-micelles containing the reactants, the solutions were mixed together to precipitate Fe(OH)₃ (iron hydroxide):



The role of the reverse-micelles was to act as nano-reactor sites for the precipitation of the Fe(OH)₃, limiting growth and maintaining a narrow distribution of particle sizes. This reverse-micelle process was followed by a sol-gel process, in which Si(C₂H₅O)₄ (tetraethylorthosilicate or TEOS) a silicon dioxide precursor, was added. The quantity and addition method was varied as required by the desired properties, as will be detailed in later sections. The TEOS reacted with the water to form the SiO₂ (silica) matrix, which acted as the diffusion barrier during heat treatment.



The reaction resulted in the formation of SiO₂ with C₂H₅OH (ethanol) as a byproduct. Prior work has demonstrated that excess NH₄OH will act as a catalyst for the reaction of TEOS and formation of SiO₂ from the precursor, as the reaction rate between TEOS and H₂O is strongly pH-dependent[74], [75]. It was found that the SiO₂ formed in spherical shells around the iron hydroxide cores with various diameters depending on the quantity and timing of TEOS added during the reverse-micelle/sol-gel synthesis process.

Upon formation of the silica matrix around the iron hydroxide particles, the samples were centrifuged to remove excess liquid, then rinsed with CHCl₃ (chloroform) and CH₃OH (methanol) to remove excess unreacted material. Upon removal of excess material, the samples

were dried under vacuum at 80°C for 24 hours. The resulting powder was then collected and ground by hand. Following this, heat treatment was performed at varying temperatures, depending on the requirements of the experiments. Under the standard conditions, as described by Sakurai, et al., the powder was heat-treated at 1025°C for 4 hours to grow iron oxide nanorods. Under normal, unconstrained conditions, the heat treatment of iron oxide nanoparticles at such temperatures would result in substantial grain growth, leading to a rapid transition from γ -Fe₂O₃ nanospheres to much larger and thermodynamically stable α -Fe₂O₃ particles[16], [50], [76], [77].

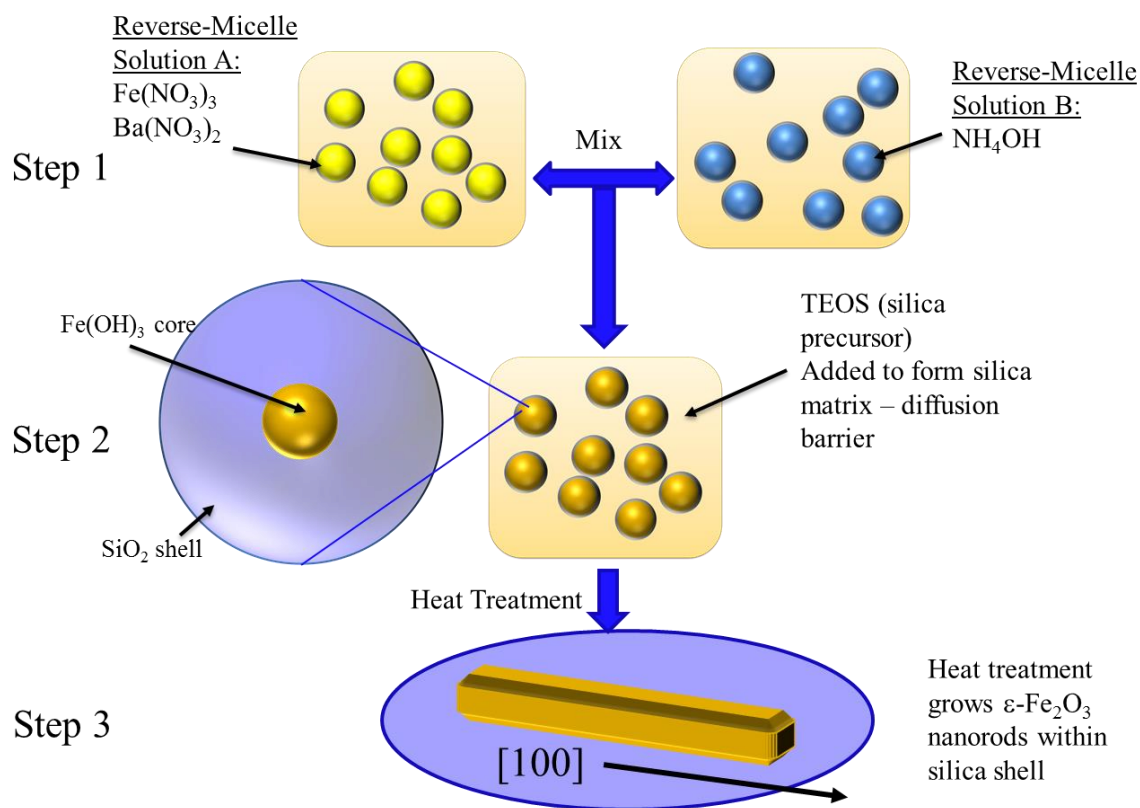


Figure 2.2 Steps of reverse-micelle/sol-gel process used to synthesize precursor materials used in subsequent work. Two reverse-micelle solutions containing the reactants are prepared, then a sol-gel process is used to form a diffusion matrix, followed by heat-treatment to form the desired phase

The barium nitrate served as an alkali ion source, which altered surface energies to encourage formation of a nanorod structure. Work by Ohkoshi, et al. demonstrated that the addition of certain alkali ions during the synthesis of Fe_2O_3 nanoparticles led to the adsorption of the ions to certain crystal planes[25]. Barium nitrate was chosen because the Ba^+ ions preferentially adsorbed to the (010) or (001) planes, inhibiting growth in these directions while allowing growth in the (100) plane. Work by Lee and Xu demonstrated via HRTEM that the $\epsilon\text{-Fe}_2\text{O}_3$ shares a crystal interface along the c-axis with $\alpha\text{-Fe}_2\text{O}_3$, and it was proposed that this interface leads to the c-axis acting as a substrate for $\alpha\text{-Fe}_2\text{O}_3$ phase on the $\epsilon\text{-Fe}_2\text{O}_3$ surface, as shown in **Figure 2.3**[28].

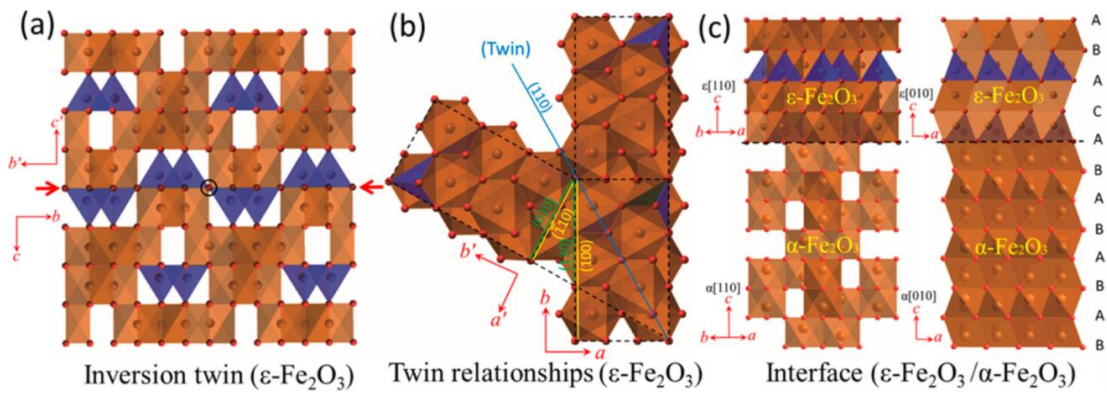


Figure 2.3 Figure adapted from [28], Structure models showing the twin relationships and crystal interfaces: (a) the inversion twin relationship (b) the (110) twinning relationship and (c) the crystal interfaces between $\epsilon\text{-Fe}_2\text{O}_3$ and $\alpha\text{-Fe}_2\text{O}_3$ along the c-axis.

This is useful when synthesizing $\epsilon\text{-Fe}_2\text{O}_3$ as it is believed to serve two purposes: increasing the stable size range of the highly metastable phase, thereby widening the processing window (time and temperature), as well as enhancing the H_c of the resulting nanorods by adding a shape anisotropy effect parallel to the magnetocrystalline anisotropy easy-direction. As previously discussed, the net magnetic properties are a result of multiple contributing magnetic energies which may either be competing or complimentary. As a result of the complimentary anisotropies,

and as demonstrated in the work by Sakurai, et al., the H_c of the as-grown nanorods was substantially higher than that of nanospheres[26], [53], [73].

The reverse-micelle/sol-gel synthesis method was chosen as the primary synthesis route for the ensuing works because of the high degree of size, shape, and phase tunability. The primary mechanism for iron oxide formation in this method relies on the precipitation of iron hydroxide from nitrate salts and water, with ammonium hydroxide acting as a catalyst. Reverse-micelles serve as nano-reactors to control the initial nucleation of the iron hydroxide cores, while the addition of a silica shell enables control of Fe diffusion and iron oxide grain growth during the heat treatment to grow the desired Fe_2O_3 phase. This initial recipe was modified as necessary for the desired properties, and are described in later sections. Hereafter, the powder synthesized through this reverse-micelle/sol-gel method shall be referred to as $\epsilon\text{-Fe}_2\text{O}_3$ precursor powder.

2.3. Background on Modifying Fe/O Diffusivity Through Silica/Silicate Glass

Both crystalline silica and glass-ceramic technology have long been important in human history and as a consequence, much work has been devoted to the study and development of crystalline and amorphous silica and silica glasses. Many forms of Si-O (silica) and silicate (Si-O-XX, where XX is additional atoms) glasses exist, with a wide range of compositions, melting temperatures, and Fe/O diffusivity[78], [79]. As the goal of this work is in utilizing silica as a method of diffusion control and not the development of novel silica technology, the primary focus when discussing silica will be the diffusivity of Fe/O in various silica glasses. Generally, diffusion of one material through a matrix of a different material will be determined by defect

concentration/size and the size of the diffusing atom. These defects may act as diffusion routes (such as transition metals diffusing interstitially) or as pinning sites which inhibit diffusion and have a strong dependence on the materials involved (i.e. larger atoms have a higher activation energy for diffusion)[35], [80]. Previous work has demonstrated that while Fe/O diffusion through amorphous silica is lower than through crystalline silica (some attribute it to the defects in amorphous silica acting as pinning sites), Fe/O diffusion through silicate glasses can be orders of magnitude higher than in pure silica. It is predicted that the introduction of larger atoms into the silica lattice enhances diffusivity of Fe through the silicate due to the higher concentration of oxygen vacancies, which act as large defect sites, enabling enhanced Fe/O diffusion[81], [82]. Essentially, incorporation of a high concentration of additional atoms into the SiO₂ lattice acts to enhance disorder by creating a large concentration of defect sites, leading to both enhanced glass formation as well as enhanced diffusivity of smaller atoms. Such a method has typically been used in glass-making in order to enhance the formation of silicate glasses at lower temperatures, but should also have the additional effect of enhancing diffusivity of Fe/O atoms within the silicate matrix given the proper selection of defect-enhancing atoms. It can be seen in **Figure 2.4**, adapted from Borom and Pask[82] and Kononchuk, et al.[83] that there is a substantial increase in diffusivity of Fe atoms through sodium-silicate compared to the diffusivity through pure amorphous SiO₂ (silica).

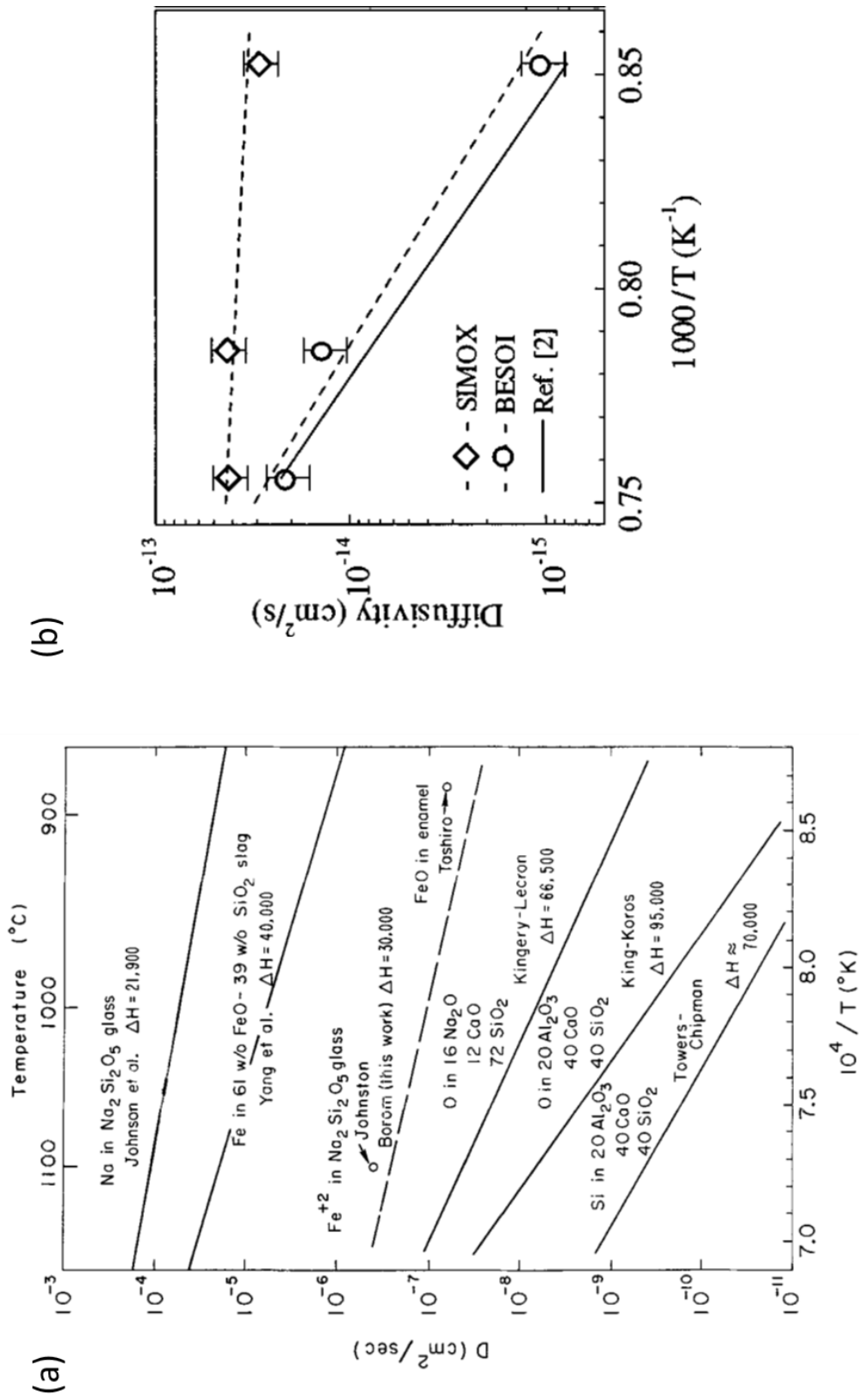


Figure 2.4 (a) Diffusivity of various metal ions through different metal-oxides, figure from [82] and (b) Diffusion of iron through a silica layer grown on a silicon substrate, figure from [83]. Diffusivity of Fe through sodium-silicate glass is shown to be significantly higher than pure SiO_2

The values reported by Kononchuk, et al.[83], as shown in Figure **2.4b** are for Fe diffusion through SiO₂ layers grown on silicon substrates through bonded-and-etched-back (BESOI) and separation-by-implantation-of-oxygen (SIMOX) methods. It can be seen that along with compositional differences (**Figure 2.4a**), the Si-O synthesis method can also greatly affect the slope of the diffusivity vs temperature behavior (**Figure 2.4b**). In addition, the activation energies for Fe diffusion through Si-O/Na-Si-O can vary drastically depending on composition as well as synthesis method, having been reported from 1.0 eV to over 3.0 eV[82]–[84]. As such, it should be expected that varying composition and synthesis method should produce some variation in the activation energy. It can be seen that diffusivity of Fe through sodium-silicate glass is significantly enhanced over pure silica glass. Given that grain growth rates are inherently governed by diffusion rates, the implication of such enhanced diffusivity in a silicate matrix is the potential for enhancing grain growth at lower temperatures. Historically, much research has been dedicated to developing silicate glasses, and many options exist for glass recipes, with significant variation in melting temperatures, viscosities, glass-former atoms/concentrations, and potential for reaction with Fe/Fe-O[78], [79], [85], [86].

2.4. Powder Processing and Consolidation Techniques for Fe-O/Si-O Composites

2.4.1. Overview of Powder Processing Methods

Following the synthesis of the precursor powder, a variety of powder processing and consolidation methods exist which may be used separately or in conjunction in order to achieve the desired properties. The wide range of powder processing techniques (prior to consolidation) includes various mechanical milling techniques, mixing of powders, doping, and heat/atmosphere

treatment. Within each processing technique, there are variations in implementation method, with unique advantages and disadvantages. To determine the ideal combination of processing techniques in order to achieve the desired phase control and bulk magnetic properties, it is useful to begin with an analysis of each technique.

Mechanical milling techniques are perhaps some of the most widely used techniques in ceramics and metallurgy powder processing. The fundamental mechanism that is universal to all mechanical milling techniques is the application of large mechanical forces in order to break agglomerates, deform the particles, mix various powders, or mechanical alloying[87]. Milling techniques may range from fairly simple processes, such as hand grinding with a mortar and pestle, to more intricate systems such as: low energy ball mills, shaker mills, planetary ball mills, attritor mills, and larger and more complex industrial sized mills used commercially. The major advantage of milling techniques is the ability to (relatively easily) process powders into homogenous mixtures for further processing. In some cases, under sufficiently high energy milling, it is possible to cause chemical reactions or crystallographic phase changes[88], [89]. Because of the potential for kinetics-induced crystallographic phase changes, higher energy milling techniques may not be desirable when processing ϵ -Fe₂O₃ precursor powders.

In addition to mechanically processing the synthesized powders, phase/compositional changes may be induced via mixing or doping. An important distinction should be made between mixing and doping of powders, in that the mixing of powders in the context of this work involves the addition of one or more additional materials in quantities typically greater than 1 mol% for the purpose of creating a composite of two separate phases. Doping, on the other hand, refers to the introduction of small quantities of a secondary material (typically >1 mol%, but heavy doping may involve larger quantities) into the lattice of the primary material either substitutionally or

interstitially, thereby distorting the crystal lattice of the material and altering the properties. Both mixing and doping may be achieved through a variety of methods, including milling, chemical dispersion, gas/atmospheric deposition, or highly energetic methods such as ion implantation[87], [90]. Due to the metastability of the desired iron oxide phases, higher energy methods may induce unwanted phase changes, and therefore low energy methods of mixing and doping were chosen, such as low energy milling or chemical dispersion.

Heat/atmospheric treatment may be necessary for a multitude of reasons: calcination for removal of excess byproduct, inducing phase transformation, reduction/oxidation, inducing additional chemical reactions, or annealing to remove defects in crystallites. In choosing the processing conditions (temperature, time, and atmosphere), one should consider that any of these processes may simultaneously occur. An example of this is in the case of Fe_2O_3 , in which annealing to remove defects may also cause a crystallographic phase change or cause a reduction to Fe_3O_4 , FeO , or even pure Fe under hydrogen atmosphere[91]–[93]. While these results may be desirable in certain cases, the grain size-dependent stability of the metastable Fe_2O_3 polymorphs make such reduction undesirable, as the additional energy input required to re-oxidize would likely also encourage grain growth in the particles.

2.4.2. Overview of Powder Consolidation/Densification Methods

Typically, a permanent magnetic material requires a large volumetric magnetization, which naturally requires a high density in a material. This naturally requires the consolidation of the synthesized nanoparticles into a bulk, functional magnet. Many modern commercial magnets (ferrites, rare-earth based, or other ceramic magnets) are typically produced via various powder

metallurgy methods. Powder metallurgy is a blanket term which encompasses several steps of powder-to-bulk processing, as well as multiple methods of consolidation, consisting of: processing of the powder (with the methods previously described), compaction of the processed powders, followed by the actual consolidation process, and finally alignment under field (which can be performed either during or after the consolidation process). In traditional ceramics processing, free-sintering was, and still is, the most widely used and simplest method of achieving a high density. Under conventional free-sintering, a powder is first compacted into the green body (a tightly packed collection of powder) then heat treated (usually in air). During this process, a high density is achieved primarily through sintering of the individual grains and typically requires prolonged exposure to high temperatures (12+ hours at 1200°C or higher for Fe₂O₃)[76], [94]. With sintering being the dominant mechanism to achieve high density, grain growth is difficult or sometimes impossible to prevent, leading to an inability to retain nanoscale metastable phases or structures. An alternative to traditional sintering is the use of flash sintering. Rapid sintering is achieved through either joule heating or microwave excitation. In both cases, a high heating rate and rapid sintering aims to minimize grain growth and retain metastable structures and phases[95], [96]. Nonetheless, materials which are metastable nanophases are difficult to retain when sintering (grain growth) is the primary mechanism for achieving higher densities. Therefore, the use of traditional sintering methods were not chosen for this work.

Alternatively, recent advances in additive manufacturing processes have provided new avenues of powder consolidation. Additive manufacturing encompasses a wide range of techniques, such as 3D printing, laser additive manufacturing, electron beam powder bed, etc[97]. A major advantage of modern additive manufacturing techniques is the potential for creating more complex geometries than in traditional sintering methods. In additive manufacturing, a model of

the desired structure is created, then material is deposited layer-by-layer. The powder is typically contained in a binder material in order to maintain the desired shape. In 3D printing methods, the binder (or ink) is retained and the processing is completed when the binder dries. An inherent drawback to such a method is the dilution of magnetic moments due to the binder material typically being diamagnetic. Laser sintering or other similar methods may provide a higher volumetric magnetization in the final product by burning away the binder material during the sintering process. However, in such cases, grain growth is also difficult to avoid, as the binder material typically causes residual porosity, which then requires further heat treatment (and grain growth) to full remove. Thus, while additive manufacturing processes may provide the ability to create interesting and complex geometries, the currently available processes may not provide a viable means of achieving both high densities (high volumetric magnetization) and retaining the metastable Fe_2O_3 phases.

A third option for consolidation of the powders is the use of large pressures in conjunction with heating, such as hot-pressing, hot isostatic pressing, or Current Activated Pressure Assisted Densification[98]–[101]. Each of these methods introduce large pressures to enhance the kinetics of densification, rather than relying purely on heat-driven sintering. Hot-pressing consists of a die and plunger set, which houses the powder, placed between a set of resistive heaters with the mechanical load applied via hydraulic press. A potential drawback from such a method is the lack of uniformity in heating and precision while applying loads may lead to unwanted thermal and mechanical stresses or thermal gradients. Hot isostatic pressing (HIP) utilizes a sealed, high-pressure vessel containing the powder and filled with an inert gas (to prevent unwanted reactions) in order to achieve the desired high pressures. In HIP, heat is typically applied using resistive heating elements, and pressure is controlled by adjusting the amount of gas and the temperature.

While extremely high temperatures and pressures can be achieved with HIP, the use of gasses and high pressure vessels typically require longer experiment times, often leading to excessive grain growth. Current Activated Pressure Assisted Densification (CAPAD), also known as Spark Plasma Sintering (SPS), Field Assisted Sintering Technique (FAST), or Pulsed Electric Current Sintering (PECS) is in many ways similar to hot-pressing, with the primary difference being that current is directly applied to the die and plunger set, meaning the die/plunger act as the joule heater, as shown in figure 2.5.

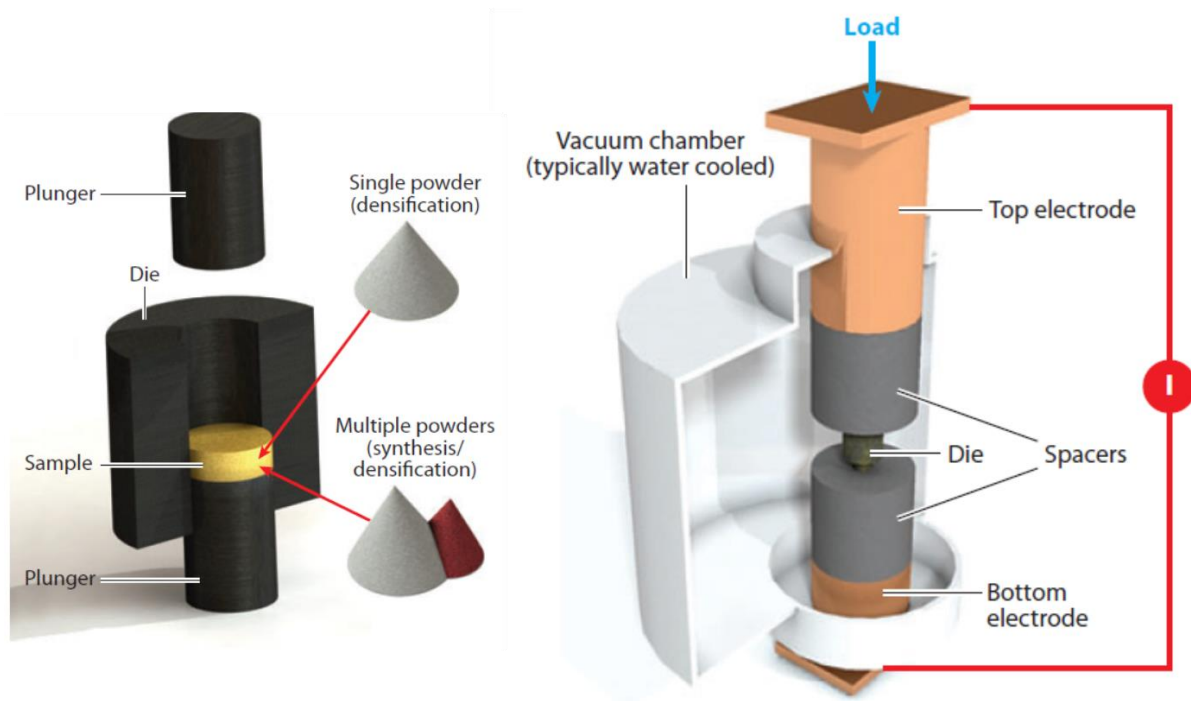


Figure 2.5 Diagram of CAPAD apparatus and the die and plunger set which houses the sample. Rapid joule heating and mechanical loads are applied via the top and bottom electrodes.

Because of this, the thermal gradients can be minimized and in some cases, much faster heating rates can be safely achieved. Furthermore, with the addition of pressure while rapidly heating, additional mechanisms besides sintering (such as particle rearrangement) may occur, allowing for not only rapid densification, but also minimization of grain growth. While typical sintering

experiments may take several hours or days, the use of CAPAD allows for experiments to be shortened to as little as minutes. With the shortened experiment time and the additional densification mechanisms, grain growth may be minimized, making CAPAD the ideal option for consolidation and densification of the synthesized metastable iron oxide powders.

3. RELEVANT CHARACTERIZATION TECHNIQUES FOR

This work seeks to both connect and decouple particle size, shape and temperature contributions to the stability of the Fe_2O_3 polymorphs in order to better understand the mechanisms for phase transformation and stabilization. From this understanding, the goal is to utilize the metastable phases in bulk, functional composites. To do so, three categories of properties must be characterized in both powder and bulk samples: magnetic, crystallographic, and structural. The relevant characterization techniques used were vibrating sample magnetometry, x-ray diffraction, and scanning electron microscopy, respectively, with multiple forms of measurements used in each technique.

The primary motivation for the work is to effectively utilize the remarkably high H_c that has been demonstrated in the highly metastable $\epsilon\text{-Fe}_2\text{O}_3$ phase. Furthermore, as previously discussed in **Section 1.3.3**, each polymorph of Fe_2O_3 exhibits unique magnetic properties with distinct M_s , H_c , and temperature-dependent magnetic reordering. These properties can be measured with a vibrating sample magnetometer (VSM), which fundamentally functions based on Faraday's law - a changing magnetic field over time induces an electromotive force. In a VSM system, an electromagnet is used to apply an external field, which induces a magnetization in the sample. By vibrating the sample at some known frequency between two pickup coils, the moving sample induces a bias, the actual measured value, which is then correlated to the magnetization value of the sample[45], [46], [102]. **Figure 3.1** depicts the basic VSM configurations.

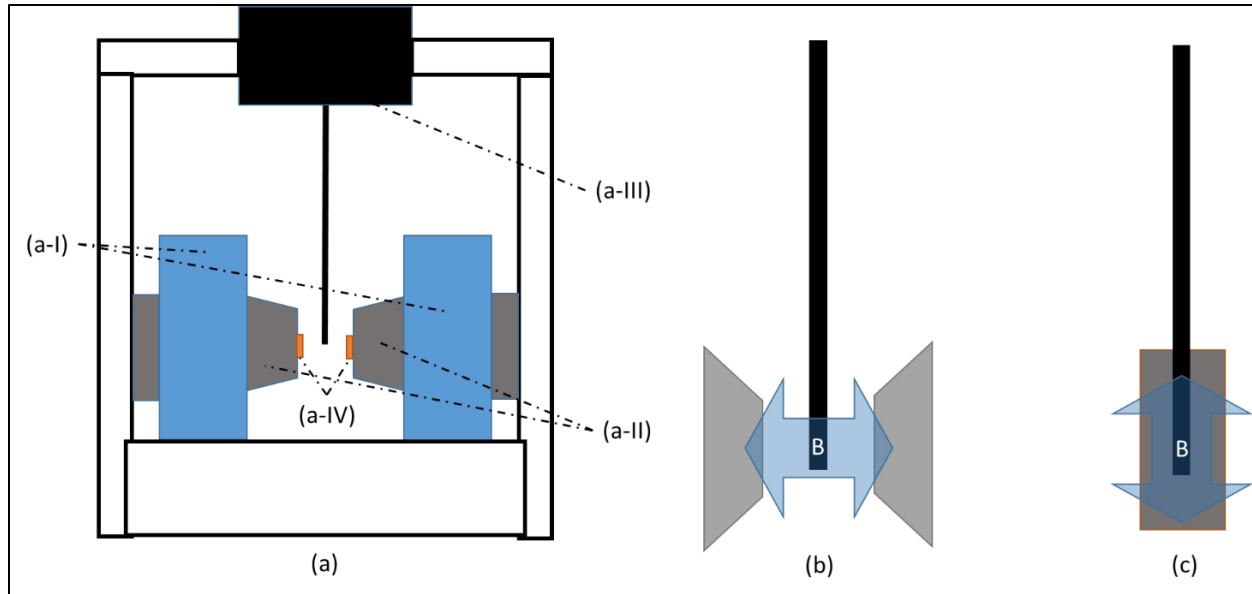


Figure 3.1 (a) A typical VSM setup with two toroidal electromagnets (a-I) used to generate the external field, pole pieces (a-II) to increase flux density, motor head to vibrate the sample (a-III), and pickup coils in which an EMF is induced and correlated to magnetization values (a-IV). Field directions are shown in a (b) classic VSM design and a (c) modern SQUID system

Traditional VSM systems typically utilize toroidal magnets, with the coils cooled with water, and are capable of applying up to around 30-40kOe (3-4T) fields on the samples. While this is sufficient for many materials, extremely hard (high H_c) magnetic materials, such as ϵ - Fe_2O_3 require much higher magnetic fields to saturate. While measurements without saturation may provide insight into the general magnetic behavior of a material, the full M_s , M_r , and H_c values cannot be obtained unless full saturation is achieved. To apply larger fields, modern VSM systems utilize superconducting coils, called superconducting quantum interference device (SQUID) which are typically liquid nitrogen or liquid helium cooled and are typically capable of reaching up to 90 kOe (9T). In addition to general moment vs field (M-H) hysteresis loop, many VSM systems are also capable of moment vs temperature measurements, which are useful for determining the magnetic transitions which can often be used for identifying the magnetic contribution of various phases. The magnetic measurements systems used in this work were a Quantum Design Versalab

and a Quantum Design MPMS. In addition to the magnetization versus applied field measurements (magnetic hysteresis loops), the VSM systems used in this work were also capable of magnetization versus temperature (zero-field/field-cooling) measurements. As previously discussed, thermal energy-dependent magnetic transitions occur in each of the Fe_2O_3 phases, which are directly related to the crystal structure. These transitions are useful for determining the magnetically dominant phase in a sample, and were carried out on each sample to corroborate other results.

The third magnetic characterization method was ferromagnetic resonance (FMR) measurements, which is a spectroscopic technique that is typically useful for probing spin dynamics of a ferromagnetic material[103]–[106]. As the spin dynamics of a magnetic material are inherently dependent on magnetic structure, different magnetic structures should exhibit a different resonance. Specifically, in the context of this work, FMR was used to differentiate and verify the existence of $\epsilon\text{-Fe}_2\text{O}_3$ from other Fe-O or Ba-Fe-O phases, which exhibit different resonance behaviors. FMR measurements were done using a Bruker EMX EPR with a frequency of 9.3 GHz.

In addition to the magnetic properties, crystallographic characterization is also important, as the magnetic properties of a material are partially determined by the crystal structure. X-ray diffraction (XRD) is the most common method for determining crystal structure (and crystal phase) of both powder and bulk materials, and was the characterization method chosen for this work. Fundamentally, Bragg's law is the principal used in XRD systems, in which some light wave interacting with a slit will create a diffraction pattern. In the case of x-ray crystallography, the light source is x-rays, which diffract on the crystal planes of a material, leading to a diffraction pattern which is unique to each crystal structure. Because different polymorphs of a material must have

different crystal structures, the diffraction patterns must be unique, and can be used to identify the phase. The diffraction patterns obtained through XRD can be useful in a variety of ways. A simple method of determining whether a material is crystalline or amorphous is in the existence of peaks, as amorphous materials should show no diffraction peaks due to the lack of any long range ordering. The signal-to-noise ratio of a diffraction pattern may provide insight into the crystallinity of the material, as a highly crystalline material will typically have a high signal-to-noise ratio due to the higher degree of ordering. In the case of small particle sizes (in the order of several nanometers), peak broadening may occur due to the large quantity of randomly oriented crystallites, which behave similarly to an amorphous material. The average particle size of the material may be determined with the width of the peaks using various formulas (such as the Scherrer equation or Williamson-Hall analysis)[107]. Furthermore, in the case of multiple phases coexisting in a sample, the relative quantity of each phase can be approximated by comparing the peak ratios. In some cases, similar crystal structures may exhibit nearly identical diffraction patterns (such as maghemite and magnetite) and are difficult to differentiate purely with XRD. Furthermore, the X-ray source should be taken into consideration, as in the case of Cu-source XRD's being used to characterize iron oxide nanoparticles, due to the potential for overlapping $K\alpha$ peaks[107]. XRD was used largely to supplement magnetic characterization techniques in order to determine the approximate phase composition in this work.

In addition to the crystallographic contribution, shape and size also heavily contribute to the overall magnetic properties, as well as inherently being linked to the overall surface energy of (and hence stable phase) of a material. To determine structure and elemental composition, scanning electron microscopy (SEM) and electron dispersive x-ray spectroscopy (EDS) were used. Scanning electron microscopy fundamentally functions through the interactions between an

electron beam and a material. An SEM system is typically comprised of an electron gun (i.e. cathode) as an electron emitter, which are then accelerated and focused through a series of “lenses” (magnetic fields) into the sample. A variety of characterization techniques are available through electron microscopy due to the different types of interactions between the electron beam and a material. The type of interaction depends on both the material and the energy of the incoming electrons, and include: secondary electrons, backscattered primary electrons, x-ray emissions, various wavelengths of light, Auger electrons, inelastically scattered electrons, elastically scattered electrons, unscattered electrons, and absorbed electrons[108]. Among these, the secondary electrons (SE), which are emitted from the k-shell of atoms and typically do not emit from more than several nanometers from the surface, are most commonly used for determining structural features, such as particle size, morphology, and surface features[73], [108]. Backscattered electrons (BSE) are a higher energy electron emission, originating from the elastic scattering of electrons with an atomic nucleus, and are useful for determining the composition of a material. Specifically, the backscattered electron energy is determined by the size (Z-number) of an atom, and can therefore provide the distribution of different materials within a sample. Similarly, EDS relies on the absorption of electrons and the re-emission of x-rays from a material. The energy of the emitted x-rays is determined by the size of the atomic nucleus. Because each element must have distinct atomic nuclei, EDS is useful for mapping of elemental composition in a sample, and may provide insight into distribution of elements (i.e. doping concentration, uniformity of composites, etc.)[108]. This work utilized SE, BSE, and EDS to determine the morphology, feature size, and elemental composition and distribution in both powder and bulk samples.

4. TUNING PHASE STABILITY OF ϵ -Fe₂O₃ BY KINETICS AND GROWTH CONTROL

4.1. Background on Size Dependent Stability and Growth of Nanometric Fe₂O₃

As discussed in previous sections, it has also been demonstrated that the metastable phases of Fe₂O₃ can exist only in certain size ranges, with ϵ -Fe₂O₃ existing as an intermediate phase between γ -Fe₂O₃ and α -Fe₂O₃[5], [25], [53], [73], [109]. This implies that the stability, and therefore the Gibbs free energy, G , is inextricably linked to the particle/crystallite size. The narrow size range of ϵ -Fe₂O₃ existence makes it exceedingly difficult to synthesize as a pure phase. A creative method to controllably synthesize each phase of Fe₂O₃ was presented by Sakurai, et al.[5], which utilized a silica (Si-O) matrix as an Fe and O diffusion pathway. This study and subsequent studies which utilize a silica matrix-based synthesis method showed that the typical formation temperature of ϵ -Fe₂O₃ is between 1000-1100°C[24]–[26], [53], [73], [110]. However, because of the interplay between kinetics and thermodynamics, it is difficult to fully decouple whether these reported formation temperatures represent the range of temperatures where ϵ -Fe₂O₃ is thermodynamically stable or the temperature range necessary to facilitate the long range diffusion necessary for the growth of particles.

This work proposes that the formation of the metastable phases is primarily dependent on surface energies and particle size, and seeks to decouple the particle size contribution from phase formation temperature. To accomplish this, it is hypothesized that altering the silica diffusion-controlling matrix to enable faster long-range diffusion which should allow for the formation of ϵ -Fe₂O₃ at distinguishably lower temperatures.

4.2. Growth Mechanisms of Nanometric Fe₂O₃ in a Silica Matrix

It is interesting to consider possible growth/transformation mechanisms involving the silica matrix synthesis procedure. As previously discussed in section 1.2.2 and section 2.2, each successive Fe₂O₃ phase grows from the original Fe-O precursors which are interspersed in the silica matrix. Since the global concentration of Fe, Si, and O is constant in this synthesis method, the growth and subsequent phase changes likely occurs in multiple steps. The initial growth mechanism should involve the sintering of silica shells which are in contact with each other. Upon sintering of the silica shell, a diffusion pathway is formed, through which Fe and O must diffuse from smaller particles to larger particles (with the driving force likely being the reduction of high energy surfaces), causing the average particle size to increase over time, as shown in **Figure 4.1a**.

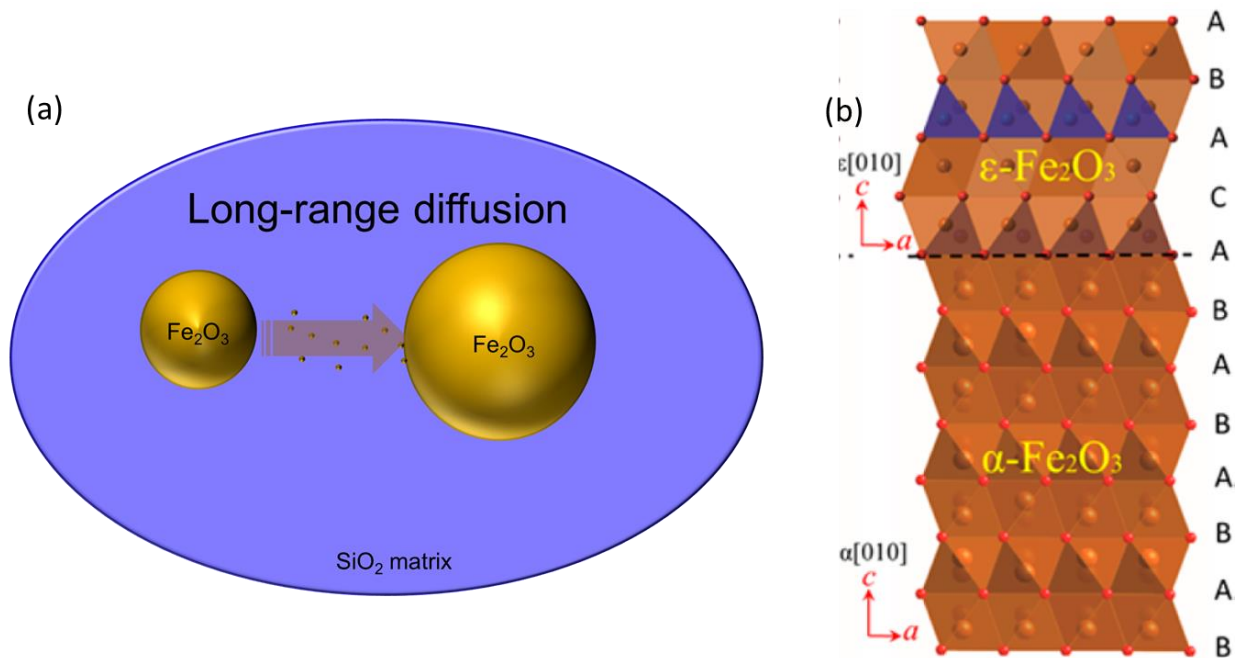


Figure 4.1 (a) Long-range diffusion of Fe and O through the silica matrix, leading to the smaller Fe-O particle shrinking and the larger Fe-O particle growing. (b) The short-range rearrangement along the c-axis, which leads to the phase transformation from ε-Fe₂O₃ to α-Fe₂O₃, adapted from [28]

In addition to the long-range transport of Fe and O from one particle to another, the formation of each Fe_2O_3 phase must involve subsequent phase transformations from one phase to another, following the process of $\gamma\text{-Fe}_2\text{O}_3 \rightarrow \varepsilon\text{-Fe}_2\text{O}_3 \rightarrow \beta\text{-Fe}_2\text{O}_3 \rightarrow \alpha\text{-Fe}_2\text{O}_3$. The kinetics of the phase transformation should be different than the kinetics of Fe diffusion through the silica matrix, and therefore have different rates, leading to one of the steps being the rate-controlling step and therefore dominates the kinetics.

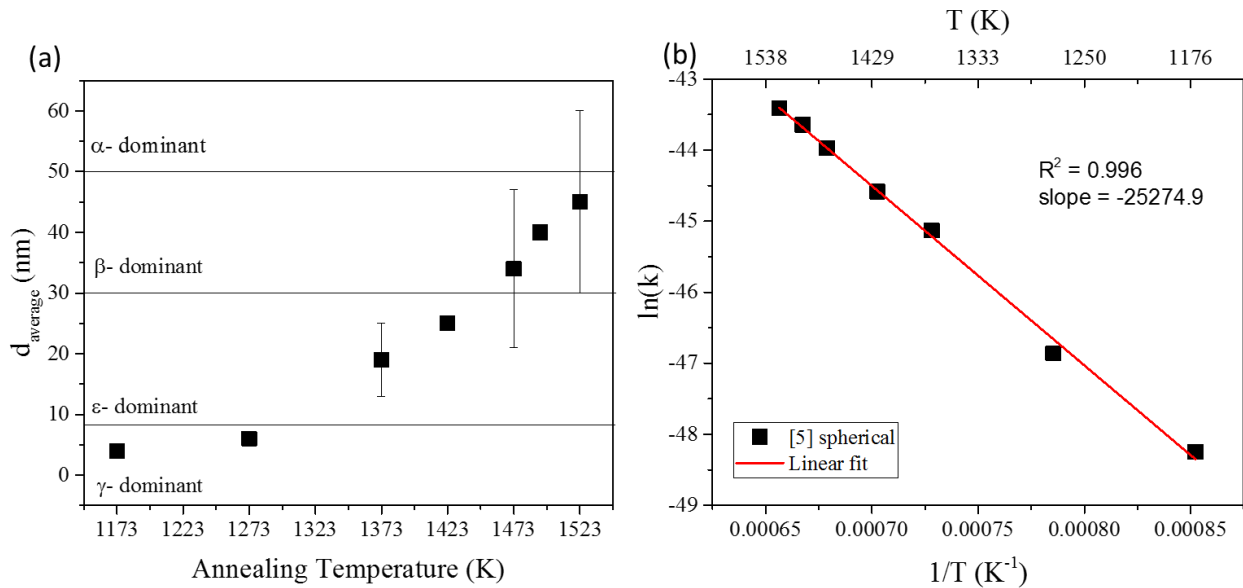


Figure 4.2 (a) Average diameter of spherical nanoparticles versus annealing temperature, adapted from [5]. (b) Grain growth model applied to data from [5]

We surmised that the diffusion of Fe/O through the silica matrix is the rate-limiting step and adapted data from Sakurai, et al.[5] which shows the average particle size as a function of annealing temperature, as shown in **Figure 4.2a**. Along with the average grain size, **Figure 4.2a** also shows the phase which is most dominant over each size range, as described in the work. The data presented by Sakurai, et al. used the same hold time of 4 hours at each annealing temperature. Since diffusion is parabolic (as shown in **eq. 1.2.4**) with time, t , a relation between the average particle size, \bar{d} and rate constant k can be written as:

$$\overline{d^2} = kt \quad [4.1]$$

where, as shown by **Eq. 1.2.5**, k is expected to have an Arrhenius relation to temperature, T . **Eq. 4.1** is derived from **Eq. 1.2.4**, with the assumption that d_0 is sufficiently small such that it is negligible and can be considered as $d_0 = 0$. **Figure 4.2b** shows an Arrhenius plot of the rate constants calculated from the data in **Figure 4.2a**, using **Eq. 4.1** and **Eq. 1.2.4**.

The data in **Figure 4.2b** shows an excellent agreement with the parabolic kinetics over the temperature range from 1170K to 1550K ($R^2 = 0.996$) and strongly implies that the long-range diffusion of Fe/O is the dominant mechanism and the growth/transformation of the Fe_2O_3 phases is primarily diffusion controlled. The activation energy for diffusion was calculated using **Eq. 1.2.5**, and was found to be 2.1 eV or 207.7 kJ/mol which is well within the range of expected values for Fe/O diffusion through SiO_2 (as discussed in **Section 2.3**). This indicates that the diffusion of Fe/O through SiO_2 follows expected trends and is useful for determining the ideal methods for facilitating desirable long-range diffusion rates.

In addition to the growth of spherical particles, Sakurai, et al.[24], [25], [73] also produced nanorods of nanometric $\epsilon\text{-Fe}_2\text{O}_3$, due to the typically higher coercivity associated with the nanorod microstructure. **Figure 4.3a** and **Figure 4.3c** shows the average dimensions of the long and short axes, respectively, from data reported by Sakurai, et al.[24], [25], [73]. **Figure 4.3b** and **Figure 4.3d** shows the Arrhenius plots calculated from the nanorod dimensions from **Figure 4.3a** and **Figure 4.3c** using **Eq. 4.1** and **Eq. 1.2.4**. Similar to the spherical particles, the nanorod dimensions also show a linear fit to the parabolic kinetics, with a long axis $R^2 = 0.991$ and short axis $R^2 = 0.979$, implying that the mechanisms of growth/phase transformations are likely similar. The

activation energies (calculated with **Eq 1.2.5**) for the short axis growth and long axis growth are 4.0 eV or 387.5 kJ/mol and 6.6 eV or 644.0 kJ/mol, respectively. These activation energies are significantly higher than the range for Fe/O diffusing through SiO₂, as discussed in **Section 2.3**, and can be explained by the surface adsorption of the growth-inhibiting Ba ions along certain directions. The Ba ions adsorb along the (010) and (001) planes (which constitute the short axis) while the (100) plane is uninhibited, and constitutes the long axis. The increased activation energy along the short axis can be explained by the adsorption of the Ba ions along these directions, which acts as an additional inhibitor to Fe/O adsorption along these directions. The much higher (6.6 eV) activation energy along the long axis may be due to the limited Fe/O interaction in this direction, as the quantity of Fe/O available along the (100) direction should be comparatively lower than the combined quantity of Fe/O along the (010) and (001) directions. This increased activation energy implies that more heat should be required for significant growth of the nanoparticles, which allows for longer time-scales to achieve comparable diffusion and growth. This is useful, as the synthesis process used in this work was adapted from the work by Sakurai, et al.[73], and produced Fe₂O₃ nanorods.

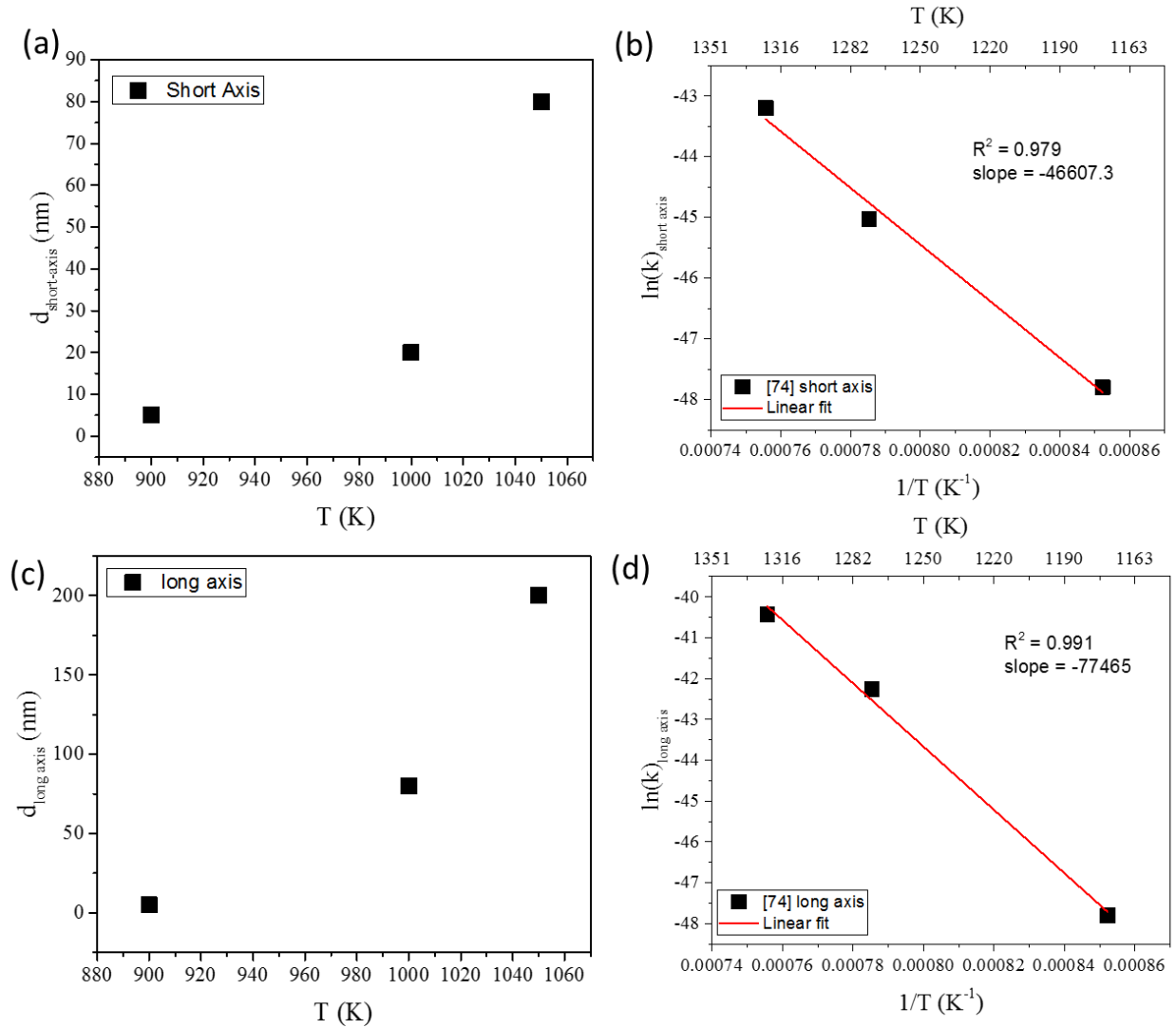


Figure 4.3 Average dimensions of the (a) short and (c) long axes of the nanorods reported in [24], [25], [73] Grain growth kinetics model applied to the (b) short and (d) long axes dimensions of the nanorods from [24], [25], [73], R^2 values are 0.979 and 0.991 for the short and long axes, respectively

Having analyzed the kinetics of the silica matrix-controlled growth from previous work[5], [25], [53], [55], [73], we hypothesized that modifying the matrix such that the diffusivity of Fe/O atoms is increased should substantially lower the temperature required to achieve similar growth of nanometric $\epsilon\text{-Fe}_2\text{O}_3$ (**Figure 4.4**). An Na-Si-O matrix was chosen to replace the pure silica (Si-O) matrix as a diffusion-controlling matrix due to the enhanced diffusivity of Fe/O[78], [111]. As

discussed in **Section 2.3** and shown by **Figure 2.4**, the diffusivity of Fe in Na-Si-O has been shown to be ~ 7 orders of magnitude higher than Si-O[82]–[84].

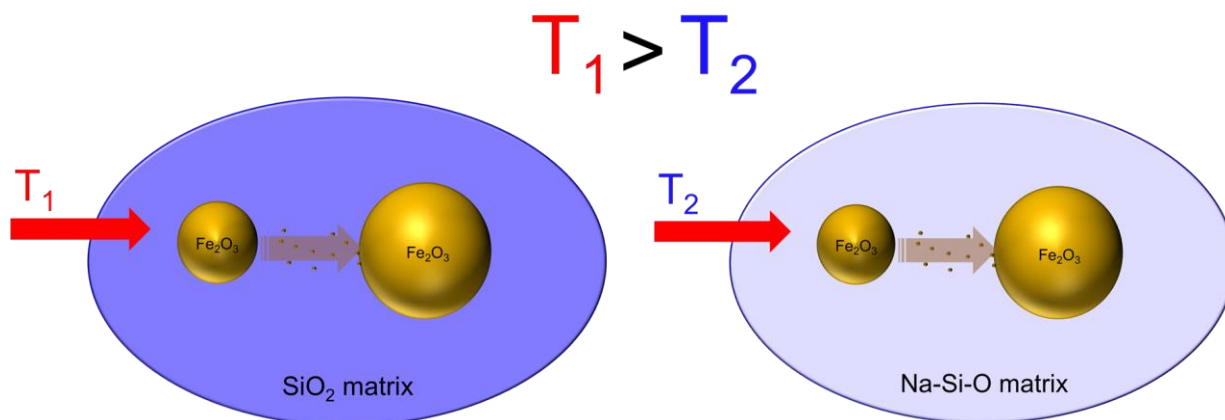


Figure 4.4 Replacing the matrix through which Fe and O atoms diffuse with a higher-diffusivity material (SiO₂ vs Na-Si-O), it is proposed that similar diffusion kinetics can be achieved with significantly lower temperatures, leading to a lower-temperature ϵ -Fe₂O₃ phase stabilization

4.3. Sodium-Silicate Shell Synthesis Procedure

The reverse-micelle/sol-gel synthesis process for obtaining ϵ -Fe₂O₃ which was discussed in **Section 2.2** was used to synthesize the core-shell precursor material. Two different concentrations of iron and barium (Fe-Ba) were studied: 15% and 90%, with the concentration being controlled by varying the quantity of TEOS (silica precursor) added. Following the initial chemical synthesis and drying under vacuum, the sodium source was added in the form of commercially purchased NaNO₃ (sodium nitrate). The vacuum-dried powder was collected and hand ground to break the coarse agglomerates, then 10% sodium nitrate by mass (relative to the calculated mass of SiO₂) was added to the finely-ground powder. The sodium nitrate was first

dissolved into solution by adding the sodium nitrate to ultra-pure H₂O at a ratio of 20:1 (H₂O:NaNO₃). The sodium nitrate solution was then pipetted into the precursor powder and mixed to distribute the sodium into the powder. **Figure 4.5** demonstrates the process by which the sodium ions are added to the precursor core-shell powder.

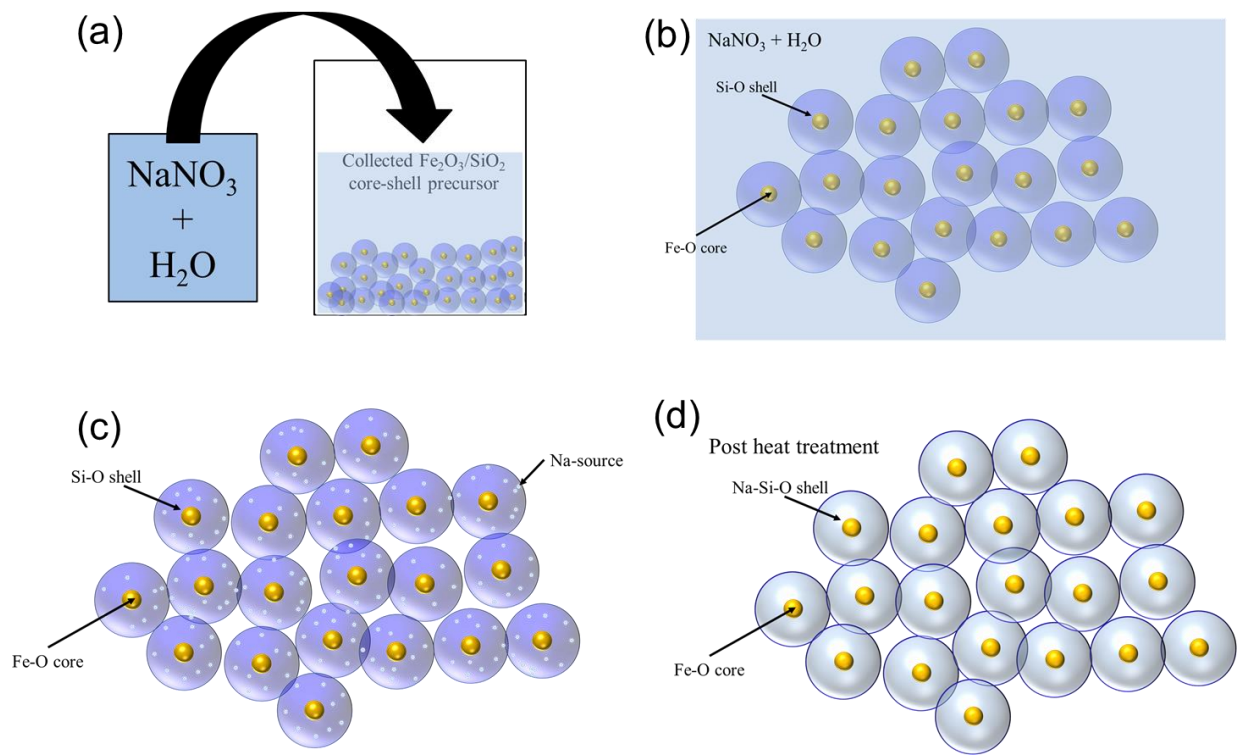


Figure 4.5 (a) sodium-nitrate is dissolved into water and mixed into the core-shell power prepared via reverse-micelle/sol-gel process (b) the sodium-nitrate solution is mixed to evenly distribute the sodium source (c) the sodium is evenly distributed on the precursor powder and (d) after heat-treatment, the SiO₂ shell is converted to an Na-Si-O shell

Following the addition of the Na source, the powder underwent a second vacuum drying process at 80°C/24 hours, then collected and hand-ground again. The collected powder was then calcined initially at 450°C to remove excess organic material and form the Fe₂O₃ core and Na-Si-O shell, then heat treated at 700, 750, 800, 850, 875, 900, 950, and 1000°C to drive Fe₂O₃ grain growth. A

heating rate of 100°C/hour and a dwell time of 2 hours was used for each sample. **Figure 4.6** shows the modifications made to the precursor synthesis process in order to form a sodium-silicate shell. Samples without Na addition were prepared and thermally processed under the same conditions for comparison. The samples are hereafter designated as Na-Si-O-XX and Si-O-XX, where Na-Si-O and Si-O are the sodium-silicate and silica shell powders, respectively, and XX are the mole percent concentration of Fe + Ba. Following the high-temperature heat treatment, the powders were then hand-ground again then characterized with VSM, SEM, and XRD to determine magnetic, structural, and crystallographic properties of the powder.

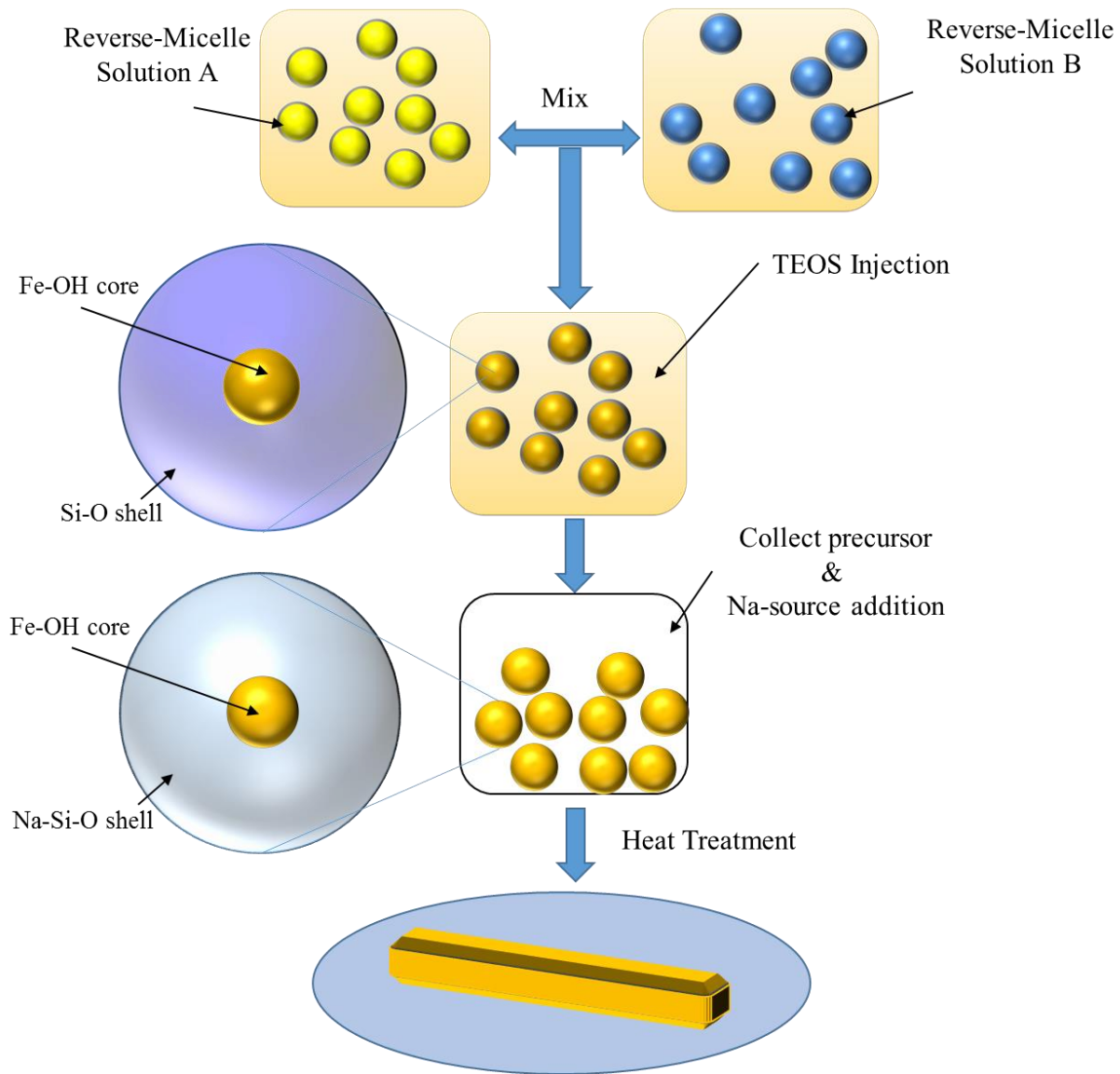


Figure 4.6 Synthesis procedure for iron oxide/sodium-silicate core-shell powder. Addition of sodium is performed at an intermediate step in order to introduce the sodium prior to crystallization of the silica shell.

4.4. Results and Discussion of Sodium-Silicate Shell Effects on Growth Behavior of ϵ - Fe_2O_3

Figure 4.7a shows SEM and **Figure 4.7b** shows TEM (courtesy of Dr. Takahito Imai of Ryukoku University, Shiga, Japan) of the Si-O-15 powder synthesized via the reverse-micelle/sol-gel process described in **section 2.2** indicating that the desired core-shell structures were obtained, with small Fe-Ba cores ($\sim 10\text{nm}$) and a thick and uniform spherical silica shell.

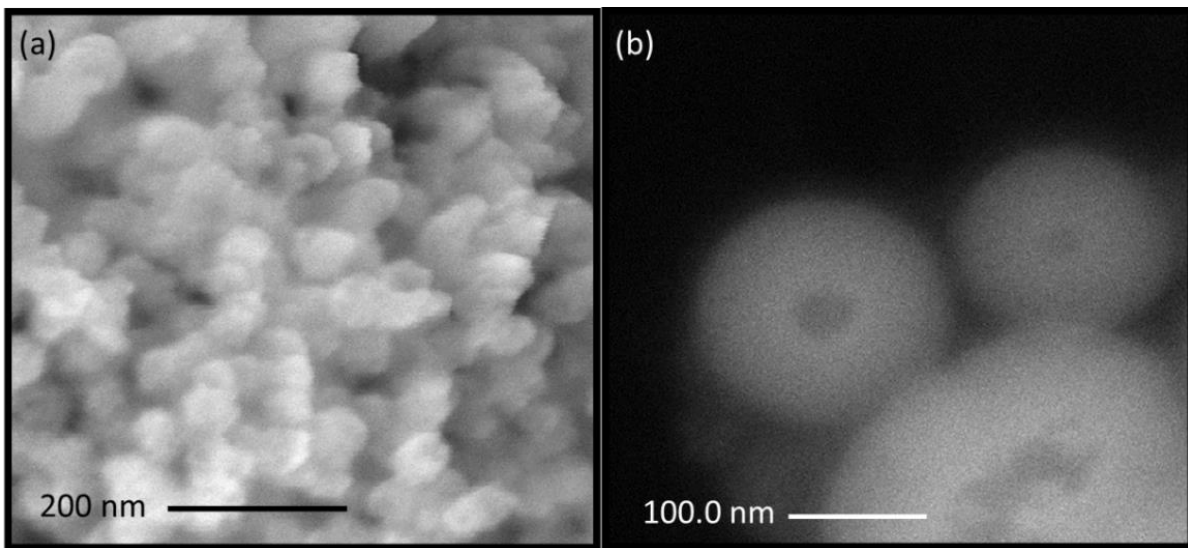


Figure 4.7 (a) SEM micrograph of synthesized core-shell Si-O/Fe-O nanoparticles (b) TEM micrograph showing iron oxide core with thick silica shell, courtesy of Dr. Takahito Imai of Ryukoku University, Shiga Japan

In the Na-Si-O shell case, initially, 20% of sodium nitrate by weight was added, but it was found that the melting temperature was significantly reduced such that the samples fully melted above 800°C and characterization was difficult. This is in-line with previous results, showing that with sufficiently high Na content, the Fe is readily dissolved into the silica and acts as an additional glass-forming element[111], [112]. By contrast, with 10% sodium nitrate by weight, the 15%-Fe-O samples remained solid up to 950°C and melting was observed at higher annealing temperatures.

The Na-Si-O-15 samples were first characterized with SEM and EDS, as shown in **Figure 4.8**, after low-temperature calcination and prior to high-temperature annealing to determine the initial morphology and verify successful sodium addition.

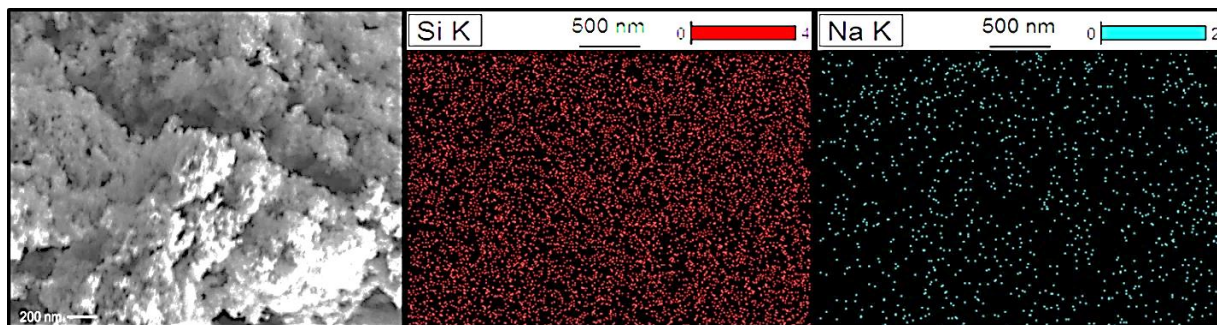


Figure 4.8 SEM and EDS of the as-synthesized powders, prior to annealing, indicate small initial particle sizes (<50nm) and a homogenous distribution of sodium

Following the successful distribution of sodium into the pre-annealed powder, both Na-Si-O and Si-O shell powders were annealed under comparable conditions. **Figure 4.9** shows SEM analysis of Si-O-15 and Na-Si-O-15 samples heat treated at 1050°C and 875°C, respectively, revealing a similar microstructure, with Fe₂O₃ nanorods observed throughout the sample. The average nanorod dimensions in the Na-Si-O-15 sample annealed at 875°C were 33 nm x 213 nm, while the Si-O-15 sample annealed at 1050°C had average nanorod dimensions of 25 nm x 205nm.

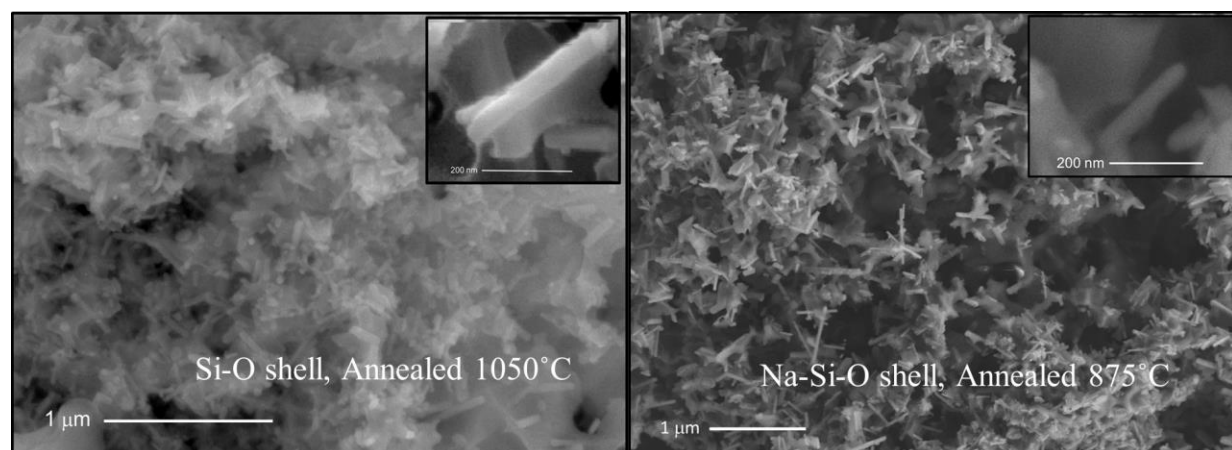


Figure 4.9 SEM micrographs of Si-O vs Na-Si-O shell samples show similar microstructure and nanorod distribution, indicating similar growth kinetics at different temperatures.

The similar nanorod dimensions between the two samples suggests that the morphology of the Fe_2O_3 was not significantly altered by changing from an Si-O to an Na-Si-O shell. This implies similar growth kinetics and should exhibit comparable magnetic properties given similar phase composition. **Figure 4.10** shows the dimensions of the short and long axes of the nanorods found in the Na-Si-O-15 and Si-O-15 samples grown at various temperatures. It can be seen that the Na-Si-O-15 sample exhibits comparable dimensions after annealing at 875°C. This is 175°C lower than the pure Si-O case. This implies similar kinetics at a significantly lower temperature, which can be attributed to the increased diffusivity of Fe through a sodium-silicate shell compared to a pure silica shell.

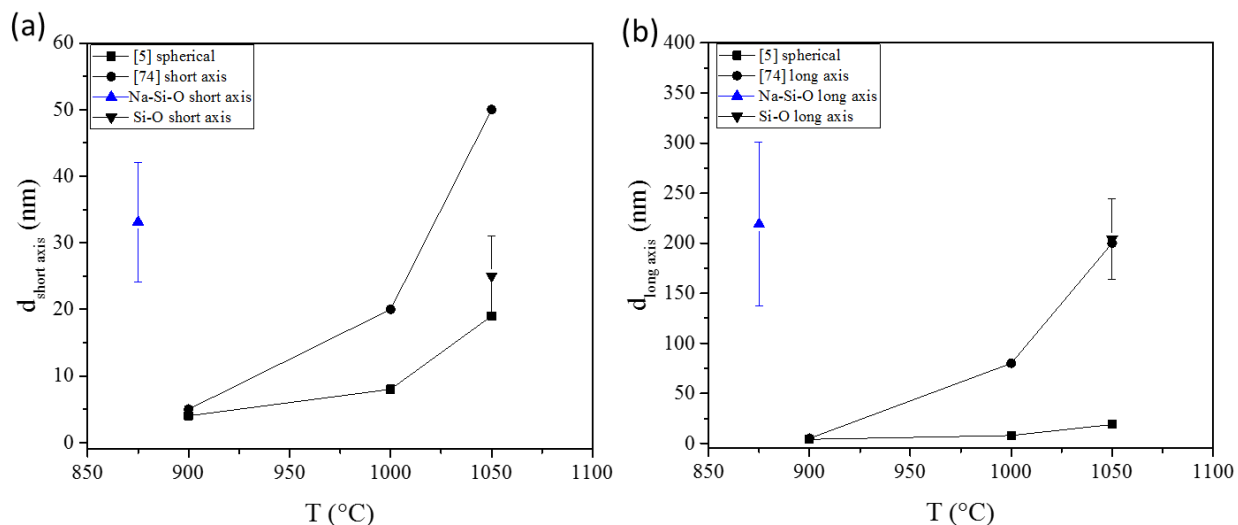


Figure 4.10 Comparison of dimensions of Fe₂O₃ nanorods synthesized in this work using Na-Si-O and Si-O matrices with 15 mol% Fe-Ba concentration with values reported in [24], [25], [73]. Similar nanorod dimensions at different temperatures are seen for the Na-Si-O and Si-O samples.

In order to compare the growth kinetics of Na-Si-O-15 and Si-O-15 samples, we used **Eq. 4.1** and **Eq. 1.2.4** and the dimension data in **Figure 4.10** and compared to the kinetics of growth for both spherical and rod-shaped particles produced in the work by Sakurai, et al [5], [24], [25], [73], which, as previously discussed in **Section 4.2**, exhibit an excellent fit with parabolic kinetics. From **Table 4.1**, it can be seen that the growth rate constant of the short axes of the nanorods produced by Sakurai, et al. is similar to the growth rate constant of the spherical particles. The kinetics of the long axis growth is much faster, which is expected given the synthesis conditions (as previously discussed in **Section 2.2**).

Among the samples produced in this work, it can be seen that at the same annealing temperature (1050°C), the growth kinetics of the Si-O-15 sample is comparable to that of the nanorods produced by Sakurai, et al., which indicates the synthesis process was comparable and produced similar results. The Na-Si-O-15 sample also shows very similar kinetics to the pure silica shell case, but at a much lower temperature (875°C), implying that a remarkably similar growth

kinetics was achieved at a significantly lower temperature. The similar growth kinetics at a significantly lower temperature supports the proposal that the increased diffusivity due to Na addition to the Si-O matrix should allow for the desired grain growth at a different temperature and allow for the decoupling of the role particle size from the temperature in the phase transformations of Fe₂O₃.

Table 4.1 Diffusion constants (k) calculated from Eq 1.2.5 for Fe/O through Na-Si-O and Si-O shells, compared with k values calculated from [5], [24], [25], [73] at different temperatures

T (°C)	[5] Spherical k (cm ² /s)	[74] nanorod (short) k (cm ² /s)	[74] nanorod (long) k (cm ² /s)	Na-Si-O-15 nanorod (short) k (cm ² /s)	Na-Si-O-15 nanorod (long) k (cm ² /s)	Si-O-15 nanorod (short) k (cm ² /s)	Si-O-15 nanorod (long) k (cm ² /s)
875				1.53x10 ⁻¹⁵	6.66x10 ⁻¹⁴		
900	1.09x10 ⁻¹⁷	1.74x10 ⁻¹⁷	1.74x10 ⁻¹⁷				
1000	4.45x10 ⁻¹⁷	2.78x10 ⁻¹⁶	4.43x10 ⁻¹⁵				
1050		1.73x10 ⁻¹⁵	2.79x10 ⁻¹⁴			4.67x10 ⁻¹⁶	2.88x10 ⁻¹⁴
1100	2.51x10 ⁻¹⁶						

Samples with increased Fe-O content (90 mol% cation concentration) were also prepared with the sodium silicate shell (Na-Si-O-90). As can be seen in **Figure 4.11**, it was found that annealing at 875°C produced a nanorod-like microstructure, although the average dimensions were significantly larger (154 nm x 651 nm) and with greater variation. The increased size and variation can be attributed to the significantly decreased Na-Si-O matrix thickness, which leads to increased initial proximity of the Fe-O particles as well as a decreased diffusion length. This in turn leads to increased interaction and growth between iron oxide particles at similar temperatures.

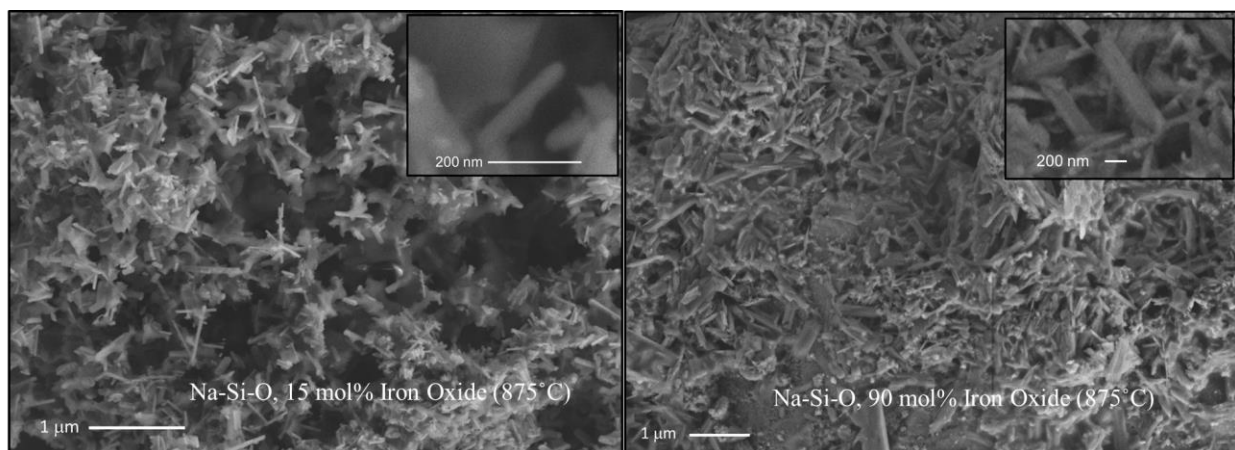


Figure 4.11 Increasing the iron oxide concentration (90 mol% cation concentration) leads to decreased interparticle distance and increased growth under the same conditions, allowing for significantly increased growth of nanorods.

As previously discussed in **Section 1.2.1**, prior work has demonstrated that the stable size range of ϵ - Fe_2O_3 ranges from ~ 10 to 200 nm as spherical particles, with an average particle size of 50 nm[5], [24], [27], [28], [53], [109]. Furthermore, prior work by Lee, S. and Xu, H.[28] demonstrated that ϵ - Fe_2O_3 and α - Fe_2O_3 share a crystal face along the c-axis, implying that the phase transformation from ϵ - Fe_2O_3 to α - Fe_2O_3 is dependent on growth along the c-axis. In the case of spherical nanoparticles, growth is relatively homogenous in all directions, whereas in the nanorod case presented in this work, the growth is heavily restricted along the b- and c-axes due to the adsorption of Ba ions along these surfaces, while growth occurs primarily along the a-axis. This agrees well with prior work by Sakurai, et al.[24], [25], [73], which demonstrated high-aspect ratio ϵ - Fe_2O_3 nanorods of up to 1.5 μm in length along the a-axis, but restricted growth along the c-axis to 50 nm. The dimensions of the nanorods presented in this work agree with these values, with the short axes (in both the 15 mol% and 90 mol% cases) falling well within the size range in which ϵ - Fe_2O_3 has been demonstrated to exist. Regardless of concentration, the long axes of the nanorods are in a size range in which ϵ - Fe_2O_3 has been reported to preferentially transform to α -

Fe₂O₃. However, because the long axes are grown along the a-axis, it is likely that ϵ -Fe₂O₃ can still exist in high concentrations in the samples, and its phase stability is dependent primarily on the growth along the c-axis.

As phase stability is typically best described in terms of the free energy (G), the link between the nanorod dimensions and phase can be interpreted by a surface area-to-volume ratio (SA:V). Typically, because free energy is a sum of both the volumetric free energy and surface free energy, the SA:V ratio can strongly influence the preferred phase. The ratios for simple geometries can be calculated (see appendix), and for a cylinder (an approximation of the synthesized nanorods), the SA:V ratio is shown to be dependent on the radius (r) and length (l). However, because the radius of the nanorods are dependent on growth along the b- and c-axes, it is implied that the radius of the nanorods (short axes) are likely the greater contributor in determining the free energies of the system.

4.5. Results and Discussion of Sodium-Silicate Shell Effects on Magnetic Properties of ϵ -Fe₂O₃

Both moment vs field (magnetic hysteresis) and moment vs temperature (field cooling) measurements were performed on the samples. It is expected that with similar microstructures, the Na-Si-O-15 and Si-O-15 samples should exhibit comparable magnetic behavior if they are comprised of the same phase. Moment vs field measurements were performed with the field ranging from 60 to -60kOe, and the moments were normalized by mass. As discussed previously, the defining feature of the ϵ -Fe₂O₃ phase is the high coercivity (typically higher than 12kOe), which is substantially higher than the coercivity typically expected for the other Fe₂O₃

polymorphs. It can be seen in **Figure 4.12** that the coercivity values of both the Si-O-15 and Na-Si-O-15 samples are very similar, at 15.5 kOe and 17.0 kOe, respectively. The high coercivity values indicate that $\epsilon\text{-Fe}_2\text{O}_3$ is likely the magnetically dominant phase. The magnetization values of both samples are 0.33 emu/g, with negligible difference, which also indicate a similar iron oxide content. While the theoretical magnetization value of $\epsilon\text{-Fe}_2\text{O}_3$ is 16 emu/g, the lower value can be attributed to a dilution effect due to the high silica/sodium silicate (diamagnetic phase) content.

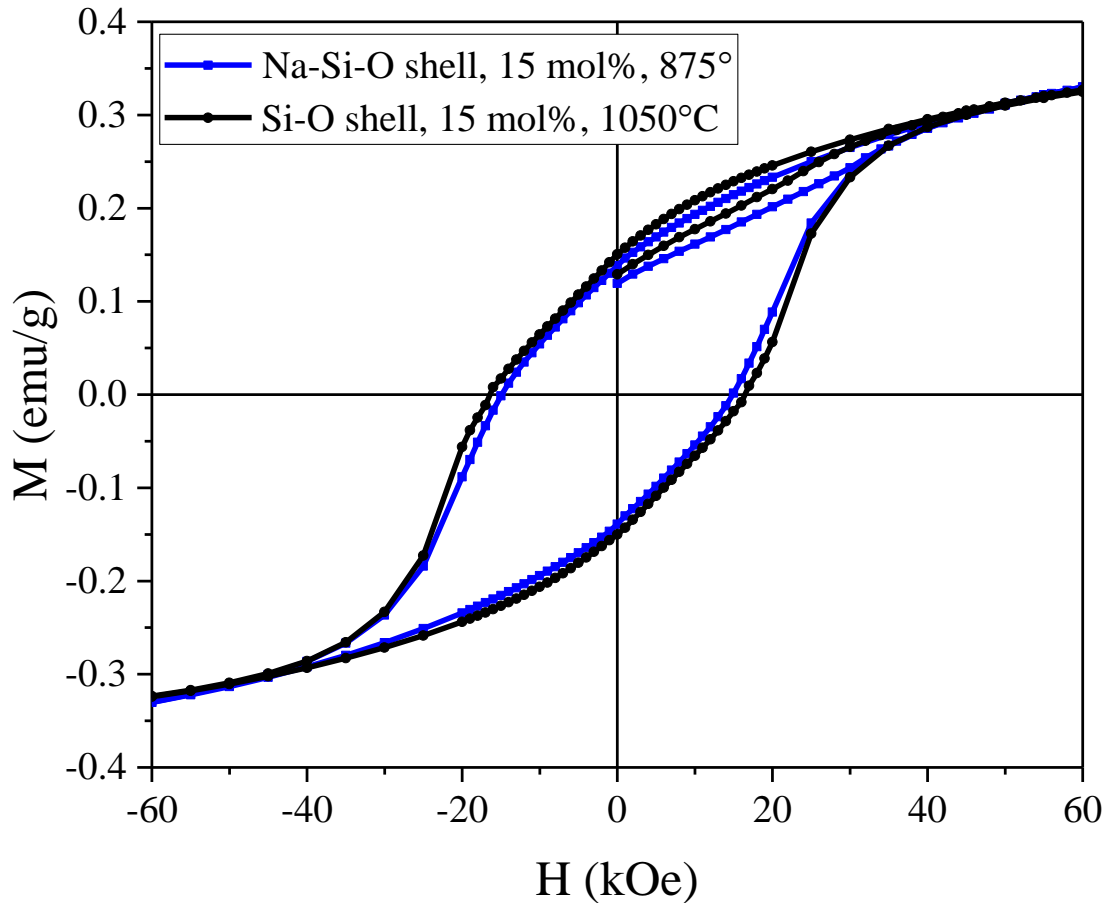


Figure 4.12 Magnetization vs field hysteresis loops of Na-Si-O-15 and Si-O-15 samples annealed at 875°C and 1050°C, respectively. The similar magnetic properties and high coercivities indicate $\epsilon\text{-Fe}_2\text{O}_3$ is likely the dominant phase

ϵ -Fe₂O₃ undergoes a Morin-like magnet transition due to the magnetic reordering from a canted-antiferromagnetic state to an antiferromagnetic state at 110-150K, depending on the synthesis conditions, shape, and morphology. This is signified by an increase in magnetization under constant field as temperature decreases before reaching a peak at 110-150K and rapidly dropping until undergoing a second transition (typically below 80K) and switching to a second canted antiferromagnetic state, signified by a gradual increase in magnetization. The first Morin-like transition is typically the most prominent transition that ϵ -Fe₂O₃ undergoes, and can be used to identify the phase in a multi-phase system. **Figure 4.13** shows the field-cooling measurements were performed on the Na-Si-O-15 and Si-O-15 samples under an applied field of 1000 Oe, and the Morin-like transition can be seen in both samples at 150K, with comparable magnetization vs temperature behaviors. At lower temperatures (below 50K), it can be seen that both samples begin to exhibit an increase in magnetization. This is indicative of a transition into a second canted antiferromagnetic state, which was previously discussed in **section 1.3.3**. The broader transition seen in the Si-O-15 sample may be attributed to some variation in grain size. A significantly larger increase in the magnetization of the Na-Si-O-15 sample may be due to the existence of a second magnetic phase such as γ -Fe₂O₃, which typically exhibits a blocking temperature at low temperature (below 50K). However, the most prominent aspect of the field cooling curve is the Morin-like transition. While the γ -Fe₂O₃ phase is known to exhibit an increase in magnetization from room temperature down to ~60K, the similar slope from 300K to 150K as well as the pronounced decrease in magnetization from 150K to ~50K indicates that the ϵ -Fe₂O₃ phase is the magnetically dominant phase in both samples.

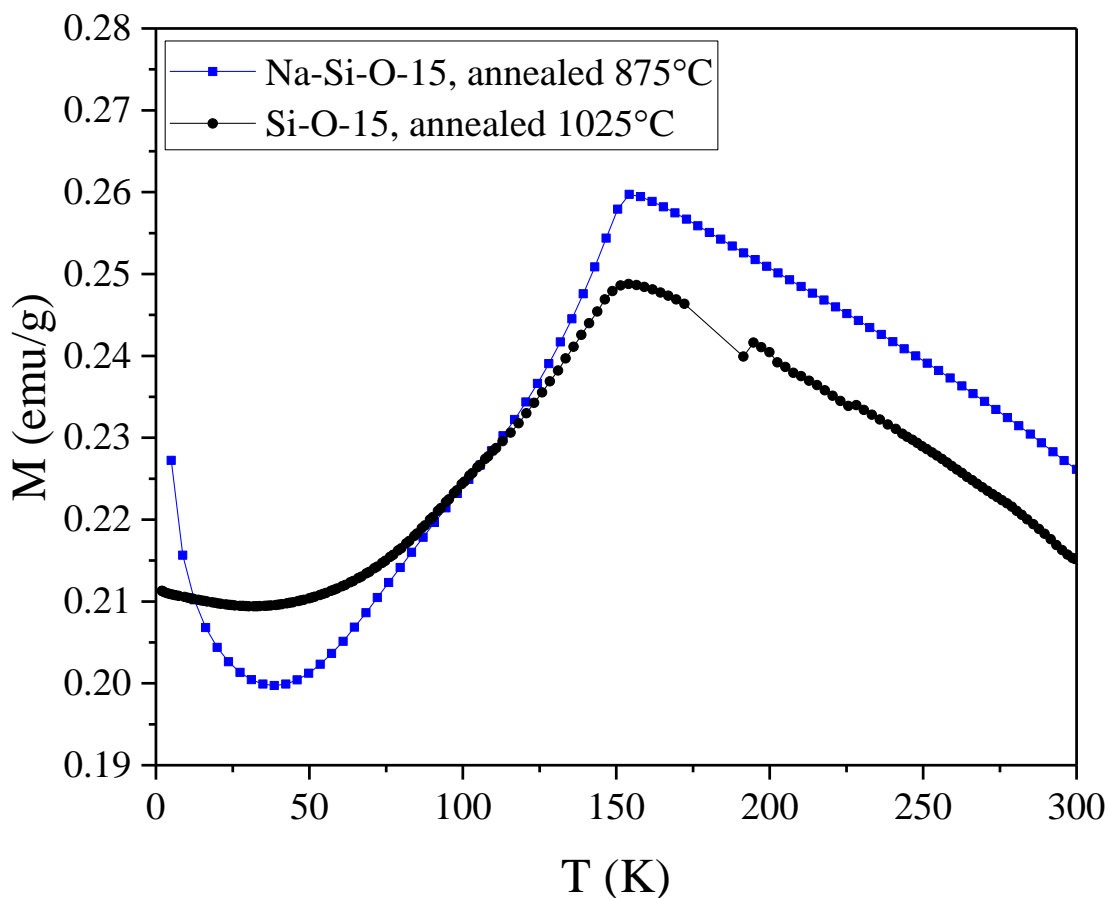


Figure 4.13 Field-cooling measurements of Na-Si-O-15 and Si-O-15 samples, which show a Morin-like transition at 150K, attributed to the ϵ -Fe₂O₃ phase.

After confirming the existence of ϵ -Fe₂O₃ in the Na-Si-O-15 sample annealed at 875°C, the samples with increased iron oxide content (Na-Si-O-90 and Si-O-90) were characterized as well. **Figure 4.14** shows the magnetic hysteresis measurements of the Na-Si-O-90 sample shows a coercivity of 13.0 kOe and maximum magnetization of 8.9 emu/g. The Si-O-90 sample showed a significantly higher coercivity of 14.7 kOe, but a slightly lower maximum magnetization value of 8.5 emu/g. The decrease in coercivity seen in these samples can be attributed to the significantly thinner shells, which allow for increased growth and variation in particle sizes during annealing.

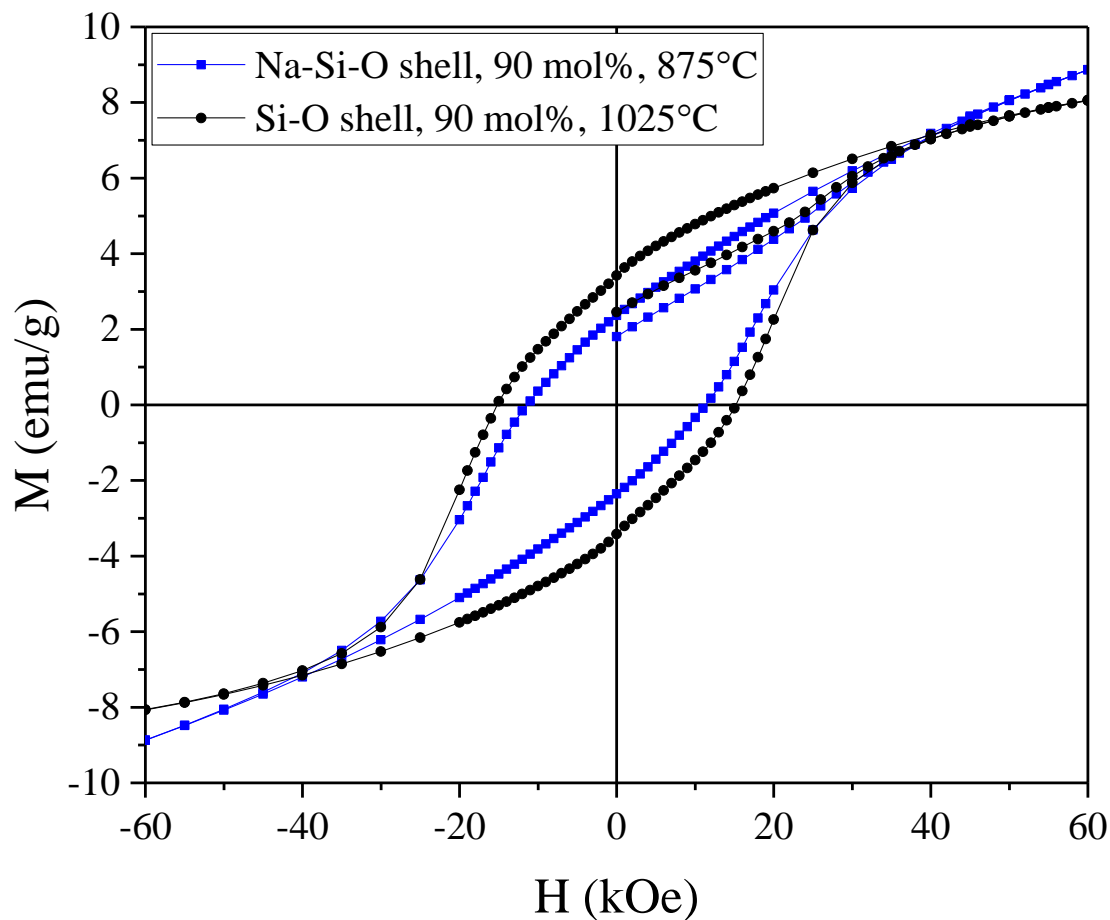


Figure 4.14 Magnetic hysteresis loops of Na-Si-O-90 and Si-O-90 samples show a decrease in coercivity in the Na-Si-O-90 sample, which can be attributed to decreased homogeneity of the nanorods. The coercivity values in both samples are within the range expected for ϵ - Fe_2O_3

Figure 4.15 shows field-cooling measurements were also performed on the 90 mol% samples, and it was found that the Morin-like transition could be observed in both samples near 150K, although there is a noticeable broadening of the transition in the Na-Si-O-90 sample and a small change in slope $\sim 260\text{K}$ in the Si-O-90 sample.

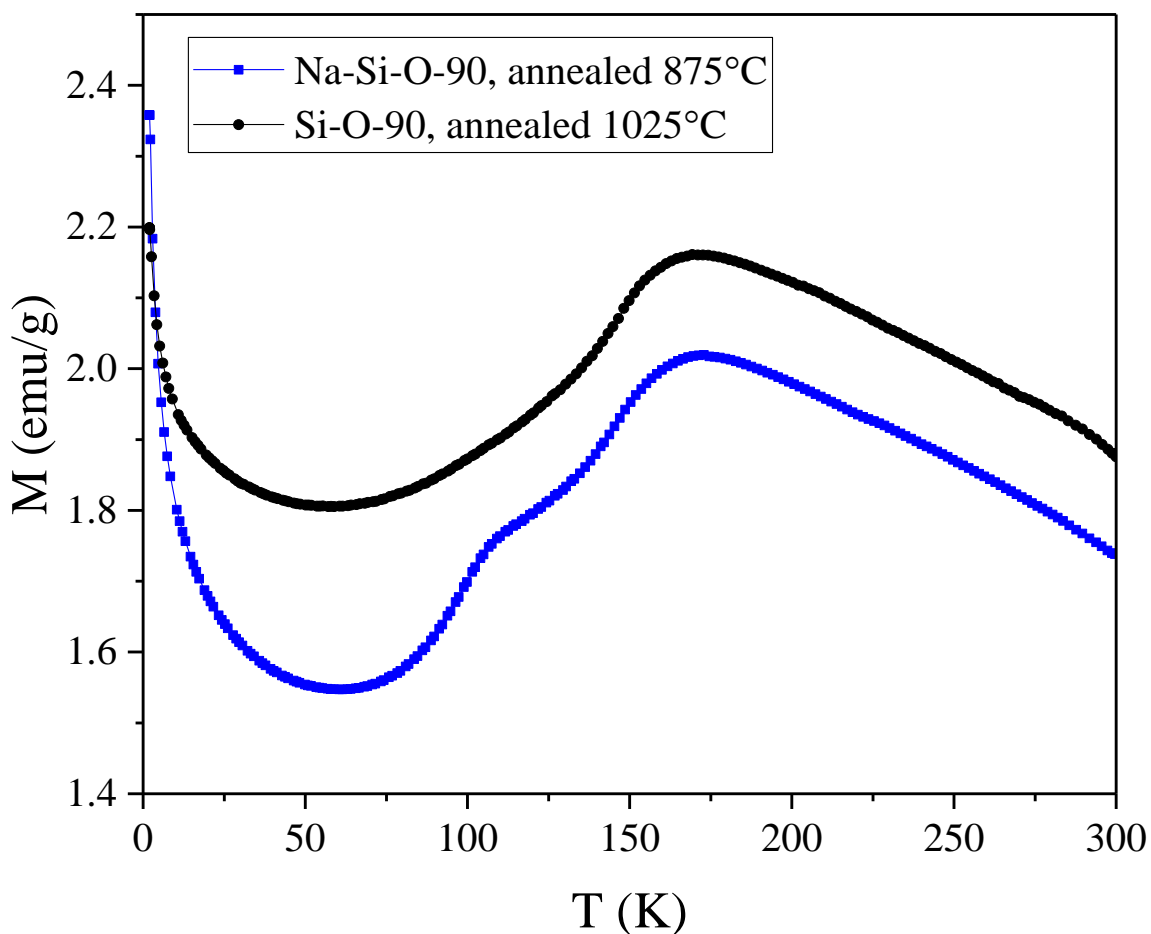


Figure 4.15 Field-cooling of Na-Si-O-90 and Si-O-90 samples show a broadening of the Morin-like transition in the Na-Si-O-90 sample, which can be attributed to the increased variation in nanorod size and dimensions. A second transition $\sim 100\text{K}$ may be due to presence of $\beta\text{-Fe}_2\text{O}_3$. The Si-O-90 sample shows a typical transition expected in $\epsilon\text{-Fe}_2\text{O}_3$.

Shifting of the Morin transition temperature had previously been observed in $\alpha\text{-Fe}_2\text{O}_3$, and has been attributed to a change in the surface energy of particles due to a combination of factors, including particle size and surface defects [15], [72], [113]. The broadening of the transition seen in both samples can be attributed to the decreased homogeneity of the microstructure with the significantly decreased silica shell thickness. Furthermore, a second transition $\sim 120\text{K}$ can be observed which may be attributed to either $\epsilon\text{-Fe}_2\text{O}_3$ (which has a Morin transition between 120-

150K) or the Neel temperature of β -Fe₂O₃. It is difficult to separate these two transitions, as the transition temperatures overlap and β -Fe₂O₃ typically co-exists with other Fe₂O₃ phases. It is possible that two major grain sizes coexist within the sample and with the large average dimensions of the nanorods in the Na-Si-O-90 sample (**Figure 4.11**), it is possible the second transition is likely due to β -Fe₂O₃. Nonetheless, the combination of the high coercivity and Morin-like transition indicates that ϵ -Fe₂O₃ is likely the magnetically dominant phase in the Na-Si-O-90 sample.

The results of the magnetic hysteresis measurements can be strongly indicative of the crystallographic phase transformations. Specifically, the coercivity of ϵ -Fe₂O₃ is the defining feature of the metastable phase. By comparing the coercivity of the samples produced under different conditions, it is possible to understand the conditions under which ϵ -Fe₂O₃ forms. **Figure 4.16** plots the coercivity of the samples annealed at various temperatures for both Si-O and Na-Si-O samples. It can be seen that the maximum coercivity for the Si-O samples is reached at 1025-1050°C. The high coercivity of the samples (>15 kOe) suggest that the ϵ -Fe₂O₃ is the dominant phase at these temperatures. The Na-Si-O samples reached a maximum coercivity at 875°C, a temperature that is significantly lower than that of Si-O samples. At lower and higher temperatures, both Si-O and Na-Si-O samples exhibit much lower coercivities, which can be attributed to other phases of Fe₂O₃. At these annealing temperatures, it is believed that the particle sizes are either too small or too large to be stable as ϵ -Fe₂O₃. Essentially, the different temperatures where maximum coercivity is reached implies that the growth rates are affecting the formation of the metastable Fe₂O₃ phase, rather than purely heat effects.

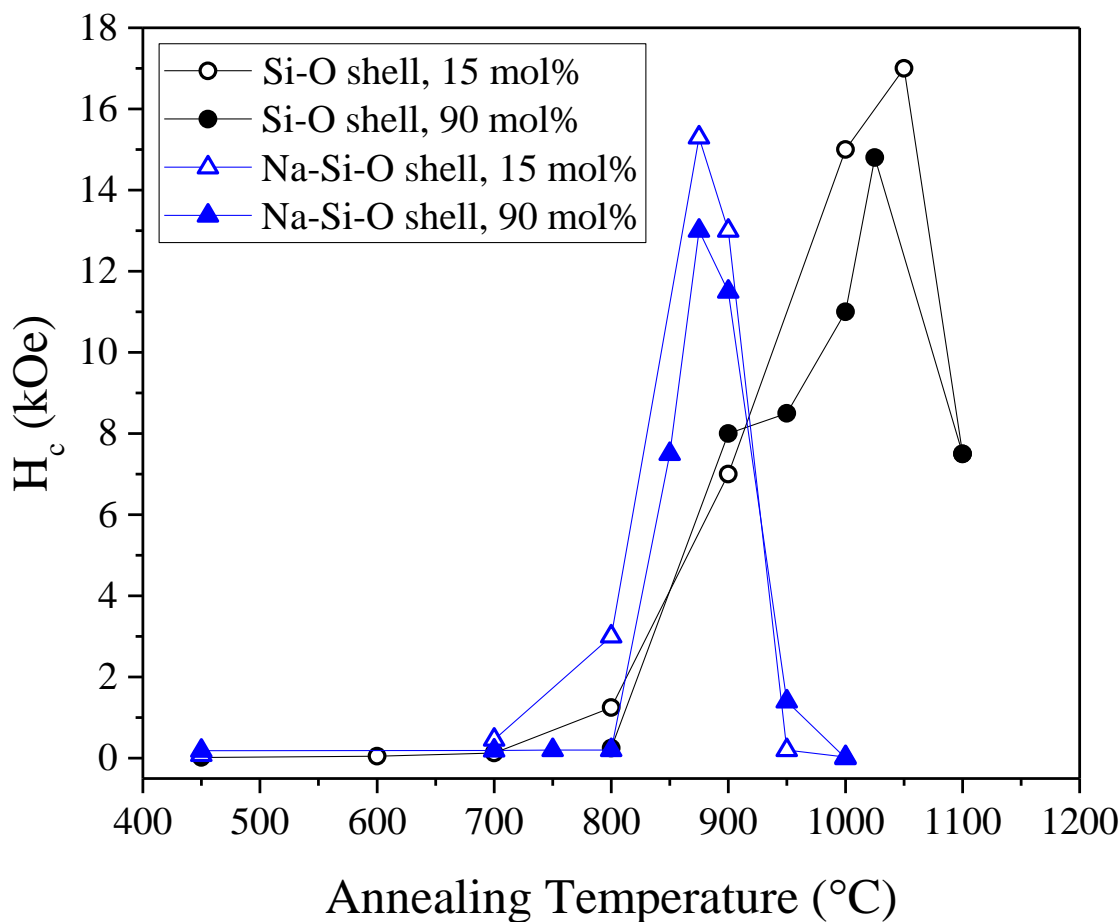


Figure 4.16 Coercivity versus annealing temperature of Si-O and Na-Si-O samples, indicating that the maximum coercivity of Na-Si-O samples is reached at a significantly lower temperature than Si-O samples.

The role of the silica shell is to act as a diffusion pathway to mediate and control Fe_2O_3 phase transformations, while the role of heat during the process is believed to primarily drive the diffusion and grain growth. Addition of sodium to the silica shell leads to formation of a sodium-silicate shell, which significantly enhancing diffusivity of Fe ions through the matrix. By increasing the diffusivity of Fe ions, a comparable microstructure to samples with a pure silica shell was obtained at a significantly lower temperature. Increasing the cation concentration led to a decrease in homogeneity of the microstructure, which can be attributed to the decreased diffusion lengths and corresponding increase in interaction rates. Measurement of the magnetic properties

of the samples verify that ϵ -Fe₂O₃ is the dominant phase in all samples prepared, with the 15 mol% samples exhibiting significantly higher coercivities, which can be attributed to the homogeneity of the formed nanorods.

4.6. Magnetic Annealing Effects on Nanometric Fe₂O₃

Field effects have been demonstrated to have a significant effect on the resulting materials during chemical reactions and thermal treatment. Prior work has shown that magnetic fields applied during chemical synthesis processes affect the reaction rates involving radical intermediates[114]. Additionally, magnetic fields applied during thermal treatment have been shown to increase the permeability of magnetic materials as well as aid in the formation of desirable microstructures in magnetic alloys to increase the shape anisotropy[2], [115]. More recently, an applied magnetic field during synthesis of Fe₃O₄ was shown to influence the resulting microstructure (nanowires vs platelets)[116]. From this prior work, we proposed that the application of a magnetic field during the annealing of powder prepared by the previously discussed reverse-micelle/sol-gel process may affect the crystallization and phase transformation behavior of the iron oxide particles. The Si-O-90 powder synthesized as discussed in the previous section was chosen for the magnetic annealing experiments, as the thinner silica shell was predicted to exhibit a more pronounced effect from the applied field.

To magnetically anneal the Si-O-90 powder synthesized through the same route described in **Section 2.2**, a custom furnace was designed, as shown in **Figure 4.17**. The small high-temperature furnace is housed within a frame containing two commercially purchased permanent magnets to supply a static magnetic field. The furnace was designed to allow for rapid heating (up

to 600°C/min) with a maximum temperature of 1200°C while insulating the magnets to avoid thermal demagnetization. It was also designed to allow for the magnets to be removed in order to anneal samples under the same heating conditions in the absence of field.

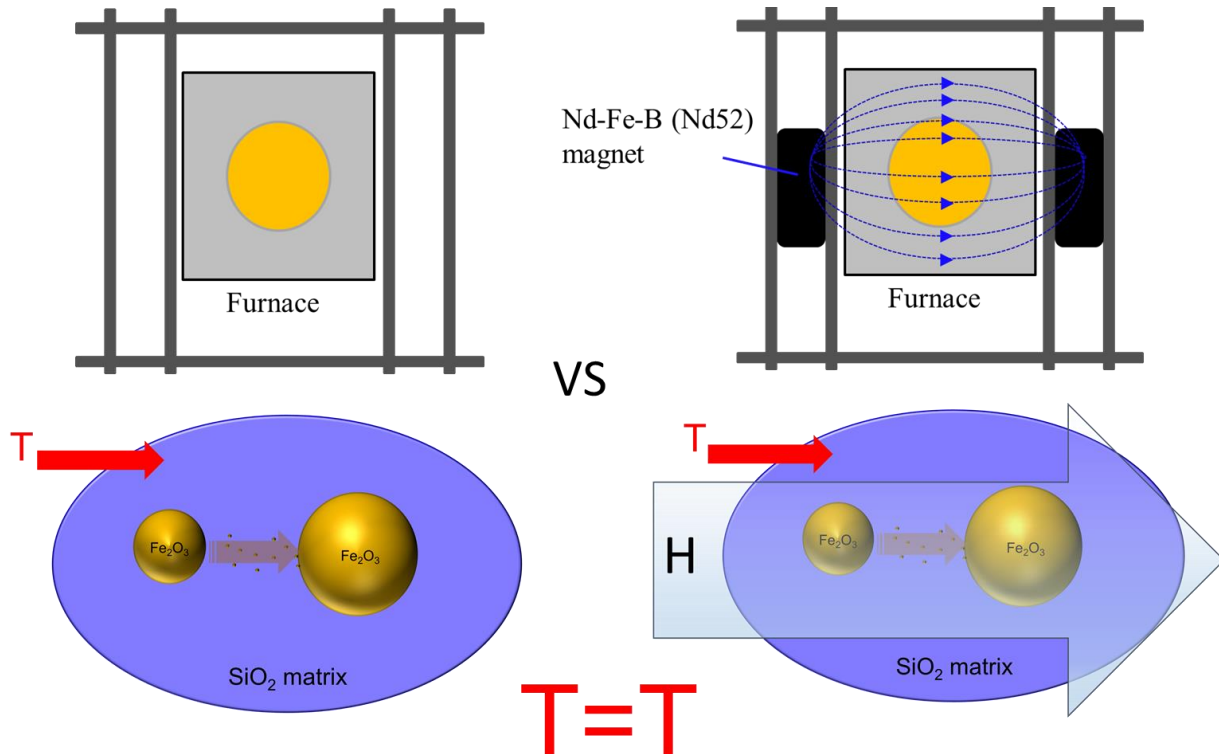


Figure 4.17 Diagram of the magnetic annealing furnace designed for the annealing tests. The system is designed to keep consistent heating parameters with a removable furnace in order to compare samples annealed with a field and without a field

Figure 4.18 shows the samples which were annealed at 450, 600, 700, 800, 900, and 950°C under a magnetic field and in the absence of a magnetic field. The powders were then magnetically characterized with VSM. The resulting hysteresis loops were normalized by the maximum magnetization values in order to accurately compare the hysteresis shapes. As was discussed in previous sections, the magnetic behavior is intrinsically linked to the crystal structure and phase.

Therefore, it is predicted that a significantly different hysteresis shape should indicate a difference in composition, both magnetically and crystallographically. In previous work, it was predicted that the formation of a magnetically ordered phases should begin at annealing temperatures above 800°C[5]. It can be seen that the samples annealed in the absence of an external field remain primarily paramagnetic until 700°C, a result which is consistent with the previously discussed results in this work (**Section 4.5**) as well as reports in literature[5], [26], [68]. After annealing at temperatures above 900°C, an increase in coercivity to values above 12 kOe indicates that likely, ϵ -Fe₂O₃ is forming as the dominant magnetic phase.

The samples annealed under a constant magnetic field exhibit similar changes, but at a much lower temperature. It can be seen that contrary to the results observed in the non-magnetically annealed samples, the magnetically annealed samples begin to exhibit a magnetic ordering behavior as low as 450°C, and undergoes a pronounced transition into a ferromagnetic state at 600°C. At higher temperatures, the differences in magnetic properties between the samples annealed with and without an external magnetic field become less pronounced, which is likely due to the thermal energy overwhelming the effects of the magnetic field. At temperatures higher than 800°C, the effects of the external field become negligible as the thermal effects on phase transformations/magnetic ordering becomes dominant.

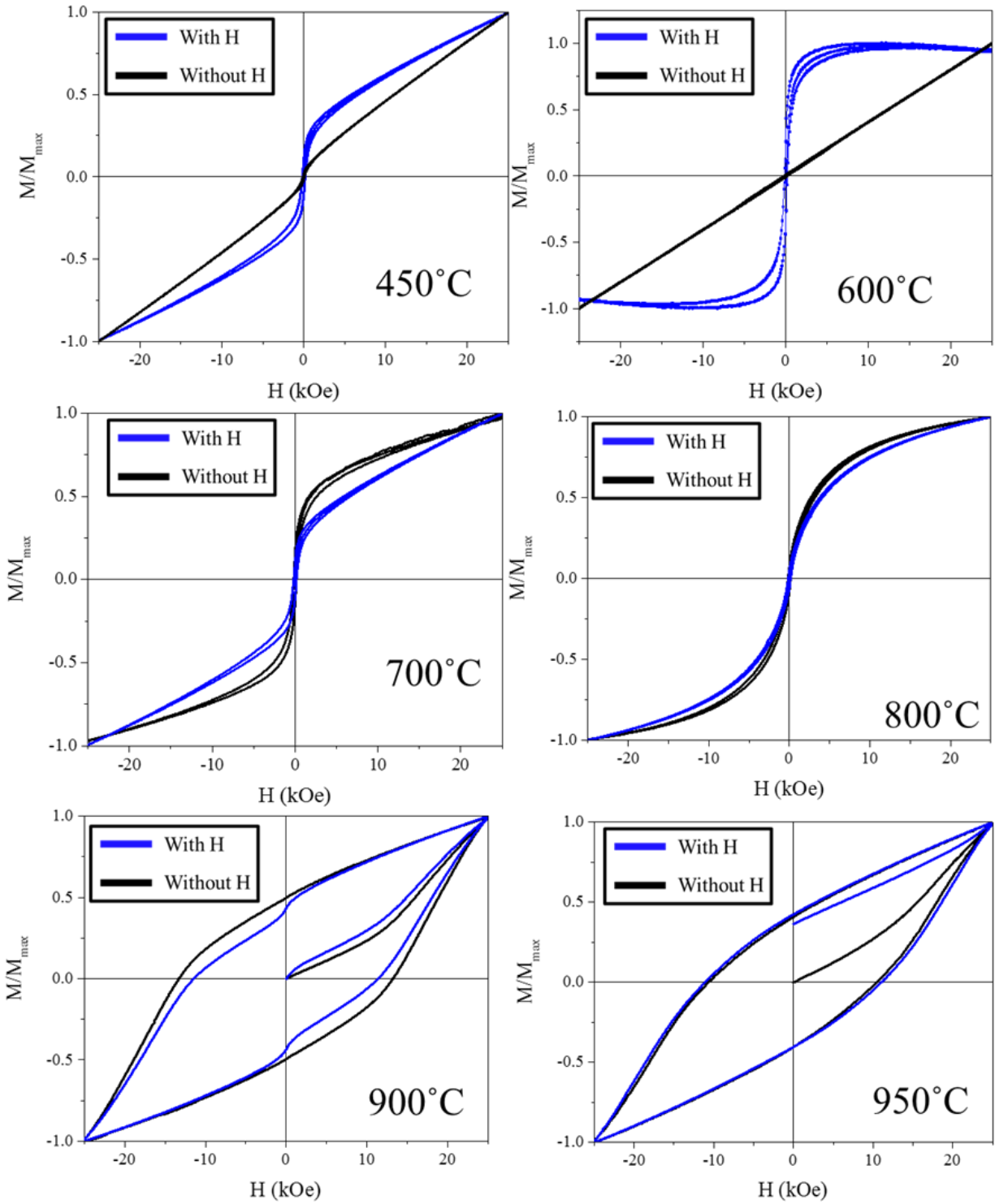


Figure 4.18 Normalized hysteresis loops comparing Si-O-90 samples annealed with and without an external magnetic field at 450, 600, 700, 800, 900, and 950°C.

It is proposed that the transition from an iron hydroxide/amorphous nano-sized iron oxide core to a larger, crystalline iron oxide core begins first with the nucleation and growth of γ -Fe₂O₃, the ferromagnetic, inverse-spinel phase of Fe₂O₃ which is typically believed to exist primarily as the smallest of the four polymorphs. The annealing process is believed to drive the transformation, nucleation, and growth of the crystalline Fe₂O₃ phases, with the increase in temperature serving to increase diffusion and growth rates. From the comparison of the normalized hysteresis loops of samples annealed with and without an external magnetic field, it can be seen that the transition towards a ferromagnetic behavior occurs as low as 450°C under field, compared to 700°C without field, indicating that it is likely γ -Fe₂O₃ is forming at a significantly lower temperature when the Si-O-90 powders are magnetically annealed.

In addition to the magnetic hysteresis measurements, field-cooling was performed on the sample annealed at 600°C both with an external field, as shown in **Figure 4.19**. It can be seen that the blocking temperature at or below 60K that has been associated with the γ -Fe₂O₃ phase, which indicates a transition in magnetic behavior in which the thermal randomization effects (flipping time) becomes slower than the effects of an externally applied magnetizing field. It can be seen in **Figure 4.19** that the magnetization vs temperature behavior of the magnetically annealed sample is similar to the γ -Fe₂O₃ transitions shown in **Figure 1.10**, implying that a magnetically ordered phase is prominent in the sample. The transition signifies the blocking temperature of γ -Fe₂O₃, which, as previously discussed in **section 1.3.3**, is known to typically occur at temperatures below 60K. Various transition behaviors may occur, but in ferrimagnetic γ -Fe₂O₃ particles, it has been shown that the magnetization values can increase with its slope decreasing at temperatures below 60K[5]. and was attained from annealing at a temperature ~300°C lower than the temperature reported in literature[5].

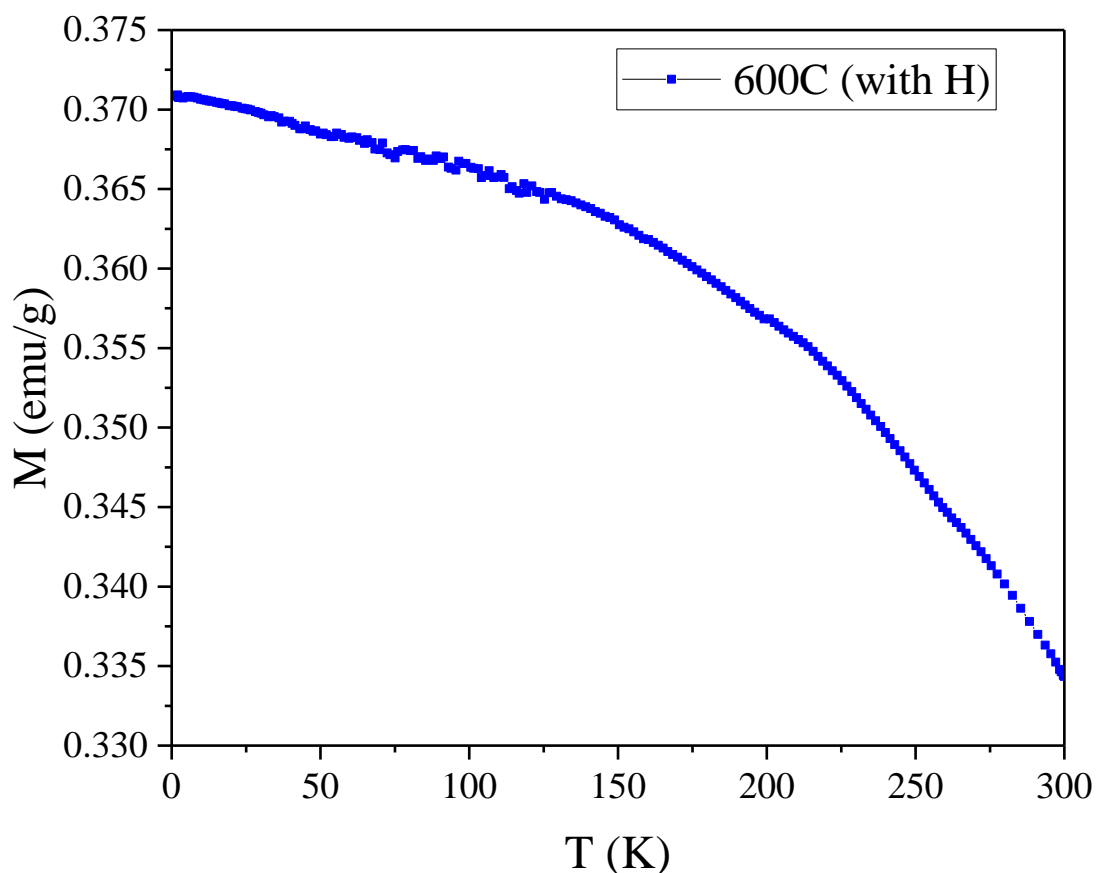


Figure 4.19 Field cooling of sample annealed at 600°C with an external field, showing an increase in magnetization that is consistent with previously reported low-temperature behavior of γ -Fe₂O₃[5]

Figure 4.20a shows the field cooling curve of the samples annealed at 600C both under field and without field while **Figure 4.20b** shows the field cooling curve of the sample annealed without field only. It can be seen from **Figure 4.20a** that not only is the magnetization value significantly higher in the sample annealed with field, but the magnet behavior is drastically different. While the magnetization of the sample annealed with an external magnetic field can be seen to level off at low temperature, the magnetization of the sample annealed without field can be seen to drastically increase at low temperature. The behavior of the sample annealed without an external magnetic field, as shown in **Figure 4.20b**, is typical behavior expected of superparamagnetic

materials, in which at the blocking temperature (usually below 50K), the magnetization can significantly increase as the thermal energy within the system is insufficient to cause the magnetic flipping.

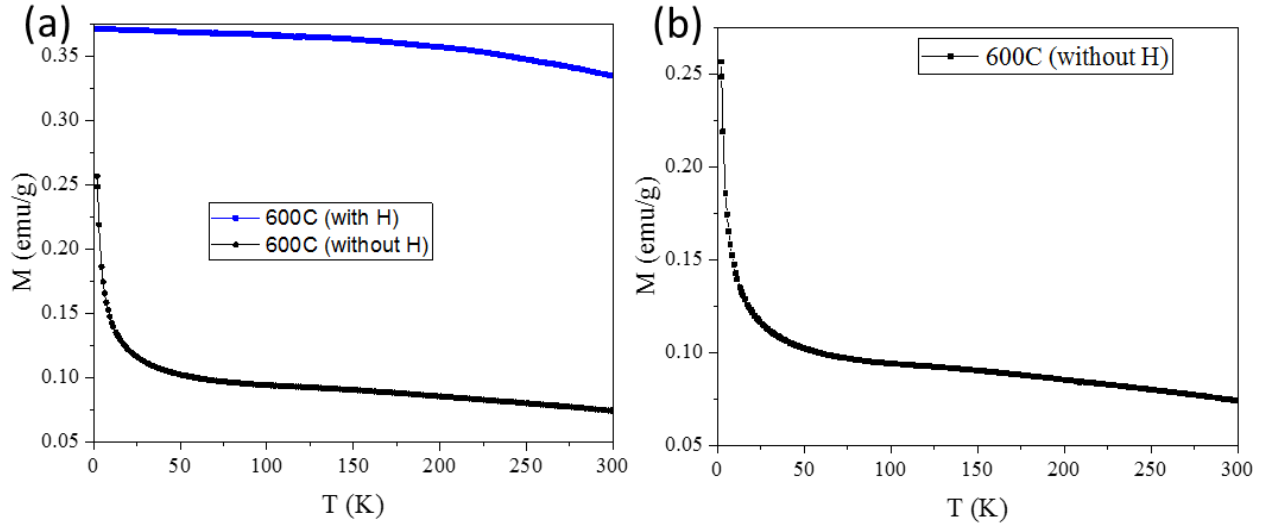


Figure 4.20 (a) Field cooling curves of samples annealed at 600C with and without field (b) field cooling of the sample annealed at 600C without field

The results from this work demonstrate that control over the low-temperature transformations of the Si-O-90 powders can be achieved with an externally applied field, which appears to drive formation of γ - Fe_2O_3 phase. These results are promising for future work in utilizing magnetic fields to facilitate or inhibit phase transformations and in enhancing controllability of metastable phase formation in magnetic materials.

4.7. Summary of Chapter 4

In summary, the goal of this project was to understand and control the phase transformations in the Fe-O/Si-O material system through various diffusion control mechanisms in order to utilize metastable phases more effectively in functional materials, as well as to decrease the energy requirements during materials synthesis and processing. The methods used to control the diffusion and phase transformations of Fe₂O₃ comprised of altering the diffusion rates of iron by altering the silica matrix surrounding the Fe₂O₃ and the application of external forces (magnetic fields) during the annealing processes. The role of the silica matrix was to facilitate diffusion of Fe and O at the desired rate, and is believed to be the rate-limiting step for phase transformations within the Fe₂O₃ system. By altering the composition of the silica matrix, the diffusion rate was altered as well, leading to enhanced diffusion and growth at a lower temperature and allowed for the stabilization of the metastable ϵ -Fe₂O₃ phase at a lower temperature. Alternatively, it is believed that the application of the external magnetic field during annealing allows for formation of desirable magnetic phases by affecting either the diffusion rate or diffusion mean free path of the iron ions, thereby allowing for the formation of a ferromagnetic phase at a significantly lower temperature. In summary, the findings from this work may be utilized to enhance the controllability and phase selectivity during synthesis and processing of functional magnetic materials.

Chapter 4 is co-authored with Professor Javier E. Garay and Dr. Yasuhiro Kodera. It is currently in preparation for submission. The dissertation author was the primary investigator and author on this paper.

5. HIGH COERCIVITY COMPOSITE MAGNET WITH HIGH ϵ -Fe₂O₃ CONTENT

5.1. Bulk Composite Magnet Based on Metastable ϵ -Fe₂O₃

The primary goal of this work was to achieve a rare earth-free, high-coercivity, bulk, permanent magnet comprised of earth abundant materials. The ϵ -Fe₂O₃ phase is well-suited for this purpose due to the remarkably high coercivity which had previously been observed in the phase. However, it is also a metastable phase, with its stability being largely size-dependent. Because of this, it is difficult to attain a bulk magnet comprised entirely of ϵ -Fe₂O₃ and prior work has largely dealt with the synthesis of the phase as a nano-material (nanorods, nanoparticles, thin films, etc.). In the previous section, the work discussed focused on understanding and controlling the mechanisms which lead to phase transformations within the Fe₂O₃ material system. By first understanding the mechanisms of the phase transformations, it is possible to then control the phase transformations and utilize the desirable metastable phases. It was proposed that the ϵ -Fe₂O₃ phase may be utilized as the magnetic component in a bulk composite material with sufficiently high magnetic content concentration to be useful as a hard magnetic material. The following work presents a method of synthesizing and processing a magnetic composite material comprised of a high concentration and high volumetric magnetization (high density) of the metastable ϵ -Fe₂O₃ phase while retaining the high coercivity.

5.2. Experimental Procedure

Figure 5.1 shows the experimental procedure used to produce a bulk composite with ϵ - Fe_2O_3 as the magnetically dominant phase. The initial powder was synthesized using the reverse-micelle/sol-gel process previously described, with the amount of TEOS added being varied to attain the desired cation-to-silica ratios. The cation concentration was varied from 15 mol% to 90 mol%. These samples are hereafter designated as IO-XX, where XX is the cation concentration in mol%. Following the initial synthesis and drying under vacuum, the powder was collected and a low temperature calcination step, with calcination carried out at 450-600°C, was added to remove excess organic residue and minimize the outgassing during the subsequent densification process. A portion of the synthesized IO-15 powder was annealed at 1025°C for 4 hours for comparison to bulk samples.

Densification of the synthesized powder was carried out using Current Activated Pressure Assisted Densification (CAPAD) – the process described in a previous section. In order to achieve the desired densification behavior, 0.25g of the synthesized powder was loaded into a graphite die with 9.5 mm inner diameter, and pressed with two tungsten carbide plungers which were separated from direct contact with the powder by a thin layer of graphite foil. The applied pressure varied from 100-300 MPa, with a load rate of 28 MPa min⁻¹. The maximum temperature reached during processing ranged from 450-600°C, with average heating rates between 100-300°C min⁻¹. All processing was carried out in a vacuum environment. After reaching the desired load and temperature, the samples were held at these conditions between 1-5 minutes before rapidly removing the load and cooling of the system. Following the densification process, the bulk samples were extracted from the die and annealed at 1025°C for one hour in order to grow the ϵ - Fe_2O_3

nanorods inside the silica matrix. The resulting samples were characterized with SEM, XRD, and VSM and the Archimedes method was used to determine density.

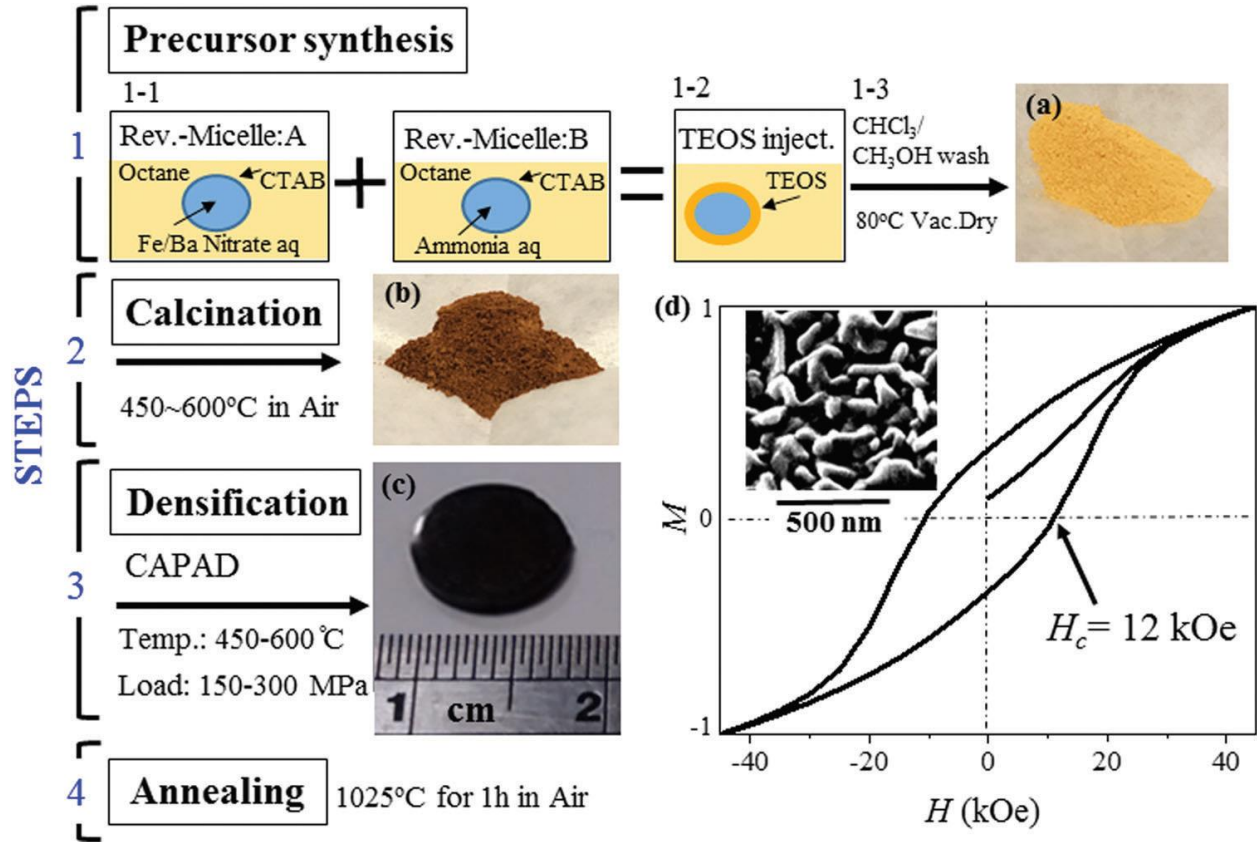


Figure 5.1 Synthesis and densification process to attain a bulk composite with ϵ -Fe₂O₃ nanorods/silica matrix[57]

5.3. Results and Discussion

The IO-15 powder was characterized before and after annealing. **Figure 5.2a** shows that prior to annealing, SEM reveals small, uniform nanoparticles of diameter less than 50nm. **Figure 5.2b** shows that following the annealing, the powder was partially etched with a 3M NaOH solution at 60°C for 2 hours, revealing many uniform nanorods approximately 50 nm x 200-300nm,

which is consistent morphology and size with previous reports[24], [25], [60], [73]. **Figure 5.2c** shows the XRD of the pre-annealed powder shows primarily amorphous material, while post-annealed powders show prominent crystalline peaks which can be identified as a combination of ϵ -Fe₂O₃ and cristobalite (SiO₂). VSM measurements of the sample both pre- and post-annealing show a transition from a weakly paramagnetic material to a high-coercivity ferromagnetic material (**Figure 5.2d**). The high coercivity (18 kOe) is a signature trait of ϵ -Fe₂O₃ and is a strong indicator that the desired phase was attained. A kink in the second and fourth quadrants of the hysteresis indicate that a secondary magnetic phase is likely forming with a significantly different magnetic remanence.

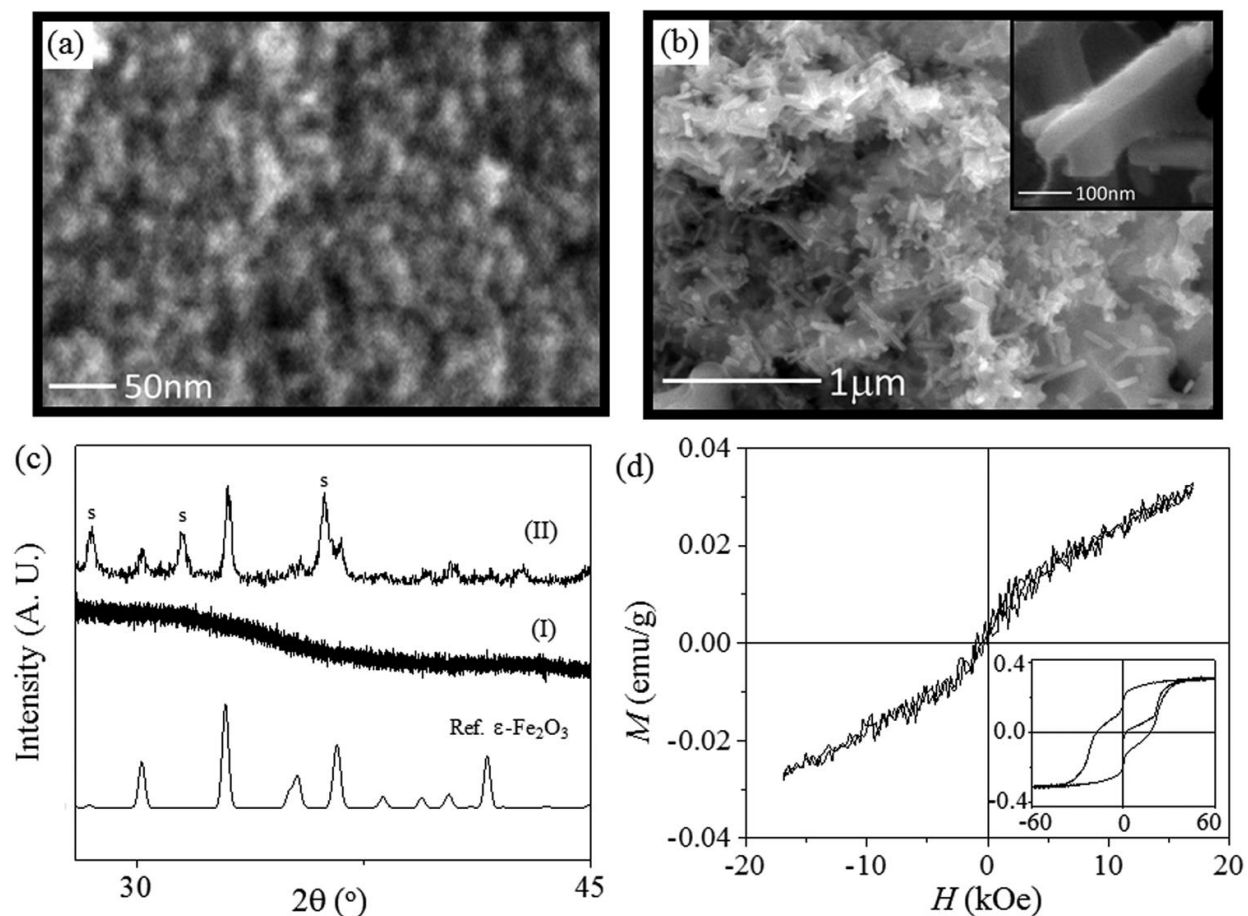


Figure 5.2 (a) SEM of pre-annealed powder showing small (sub-50nm) particles, and (b) post-annealing and partial etching showing high-aspect ratio nanorods. (c) XRD analysis shows a transition from a primarily amorphous (I) material to a crystalline material comprised of cristobalite (silica) and ϵ - Fe_2O_3 (II). (d) magnetic hysteresis indicate a transition from a weakly paramagnetic material to a high-coercivity magnetic material[57]

Following the successful conversion of the IO-15 powder to ϵ - Fe_2O_3 , the unannealed IO-15 powder was densified via CAPAD processing. To achieve the desired high concentration of iron oxide content in the bulk composite, the silica shell thickness was systematically decreased using the method described previously. Through this method, IO-15, 40, 75, and 90 samples were prepared and densified, annealed, then characterized. It was found that during densification with an applied pressure of 100 MPa, IO-15 to IO-75 samples showed similar normalized extension curves, indicating a similar densification behavior (**Figure 5.3a**), and resulted in relatively high

densities (>80% relative density). When the IO-90 sample was processed under the same conditions, it was found that the densification behavior (normalized extension) was vastly different, and resulted in a comparatively low relative density of only 71%. In order to achieve the high density required for a high volumetric magnetization in the IO-90 sample, the applied pressure was increased from 100 MPa to 300 MPa during CAPAD processing. With the higher pressure, densities >80% were achieved. Using this method, the IO-90 samples with varying densities were prepared by varying dwell time at temperature and pressure during CAPAD processing. XRD was performed on the samples after the post-densification annealing process, and comparison of samples with varying cation concentration (**Figure 5.3b**) shows that in all cases, silica and iron oxide phases can be identified. The peaks in **samples #1** (IO-15) and **#2** (IO-40) can be identified as belonging to cristobalite and ϵ -Fe₂O₃, demonstrating that at low iron oxide concentrations, the synthesis and densification process was successful in attaining a dense ϵ -Fe₂O₃-based composite. It can be seen that with increasing iron oxide concentration, the cristobalite peaks substantially decrease and the ϵ -Fe₂O₃ peaks begin to dominate. This change in relative intensity of ϵ -Fe₂O₃ to SiO₂ peaks verifies that the goal of dense composites (with comparable relative densities) with increased iron oxide content was achieved. With higher iron oxide concentrations, **sample #3** (IO-75) and **#4** (IO-90) begin to exhibit an additional peak $\sim 33.2^\circ$, which can be attributed to either α -Fe₂O₃ or β -Fe₂O₃. While it has been shown in previous work by Sakurai, et al.[5] that ϵ -Fe₂O₃ and β -Fe₂O₃ can co-exist, the results were reported for powders of significantly lower iron oxide concentration and produced with a different synthesis route, rather than the dense, bulk composites produced in this work. Furthermore, because the peaks observed in the XRD patterns closely match those of the α -Fe₂O₃ reference (PDF# 00-033-0664), and it is the most thermodynamically stable phase, it is believed that the secondary phase forming in the samples is likely α -Fe₂O₃. It is

believed that because the stability of $\varepsilon\text{-Fe}_2\text{O}_3$ is inherently size-dependent, and therefore can only exist as a nano-phase material, leading to the formation of $\alpha\text{-Fe}_2\text{O}_3$ in the high concentration samples due to the significantly decreased diffusion lengths.

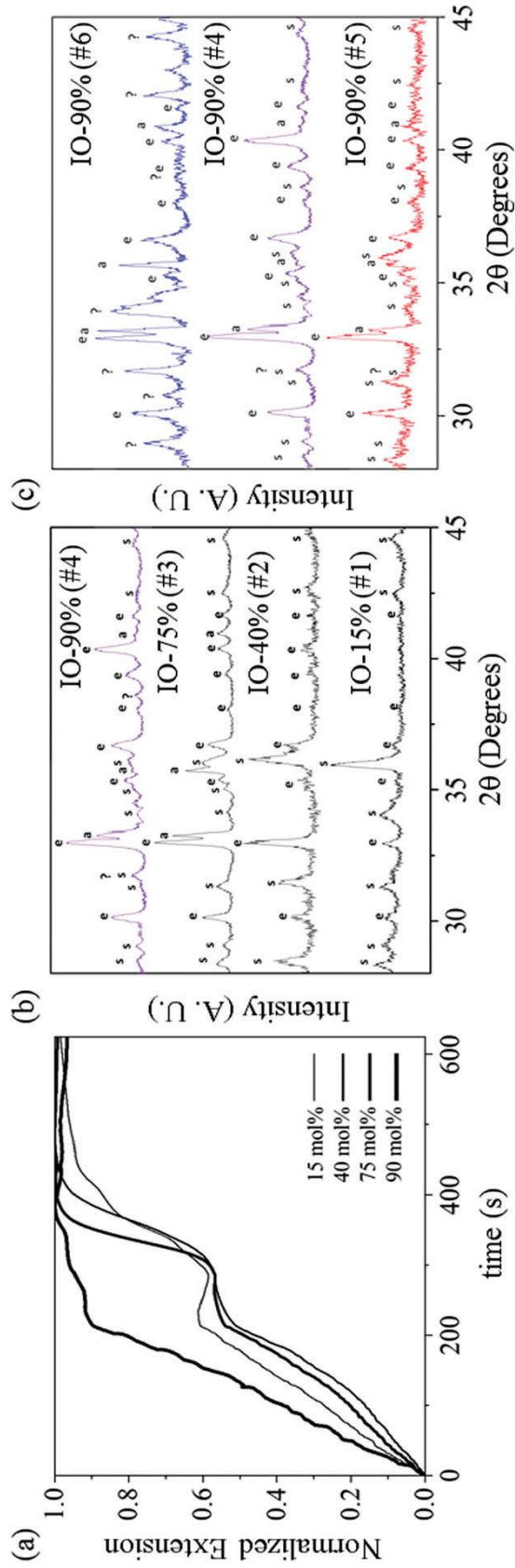


Figure 5.3 (a) Normalized extension curves show drastic change in densification behavior at 90 mol% concentration. (b) XRD analysis of samples with increasing iron oxide content indicate that ϵ -Fe₂O begins to dominate at high concentrations, but also

XRD of the IO-90 sample with varying densities was also obtained (figure 5.3c), and it was seen that the lowest density sample (**sample #5**), which was <70% dense, exhibited the highest ratio of e-Fe₂O₃ peaks to silica and secondary phase peaks. Alternatively, the highest density sample (**sample #6**), which was ~99% dense, exhibited the highest intensity of secondary Fe₂O₃ phases. The sample at an intermediate density (**sample #4**), which was ~89% dense, exhibited peak intensity ratios which were in between **samples #5** and **#6**.

Magnetic measurements of the samples showed that in the low concentration samples (IO-15 and IO-40), the coercivity was similarly high (15 kOe). As the iron oxide concentration was increased while maintaining comparable densities, the coercivity decreased to 12 kOe in the IO-90 sample. Coercivity values for varied densities in the IO-90 samples (**samples #4,5,6**) were consistent with the XRD analysis. Increased density (**sample #6**) led to the formation of secondary phases, leading to a substantially decreased coercivity (7.5 kOe), while the lowest density (**sample #5**) led to the highest coercivity (14.5 kOe). However, it was found that the best balance between volumetric magnetization and coercivity was in the IO-90 sample with 89% relative density (**sample #4**). **Table 5.1** summarizes the results of coercivity measurements for samples of varying iron oxide concentration and densities. In all samples, it can be seen that the relative densities do not significantly change before and after annealing, implying that the densities were achieved from the CAPAD processing and not from sintering of the silica or iron oxide during the annealing process. Furthermore, the relative densities of samples #1-4 are comparable, implying that the decreasing coercivity may be linked to the initial proximity of the iron oxide particles – the thinner silica shell significantly decreases the diffusion lengths, leading to greater grain growth when annealed under comparable conditions. It can be seen that the high coercivity in **sample #5**

corresponds to a low density, implying that the role of porosity in the sample may be to act as a diffusion/growth inhibitor.

Table 5.1 Comparison of the coercivity of samples with different cation concentration (samples #1-4) and varying densities at high concentration (samples#4-6)[57]

Sample#	Mol% IO (Fe-Ba)	Density-Pre Anneal (%)	Density-Post Anneal (%)	Coercivity (kOe)
1	15	94.1	93.9	15.0
2	40	88.4	88.7	15.0
3	75	83.9	84.2	12.5
4	90	89.0	87.1	12.0
5	90	67.0	69.7	14.5
6	90	99.9	99.5	7.5

It is believed that the role of density is important in the functionality of a permanent magnet based on the metastable ϵ -Fe₂O₃ phase for several reasons: a high density with high iron oxide concentration is desired as a high concentration of magnetic content is required to produce a strong magnetic response, a high density allows for greater grain growth and therefore requires careful selection of processing parameters, sufficiently increased proximity of magnetic moments may allow for a coupling effect, and a higher density should typically increase the mechanical stability of the bulk magnet, allowing for greater applicability.

These results are further summarized in **Figure 5.4a**, in which the coercivity of each sample after CAPAD processing and annealing is plotted against the cation concentration. It can be seen that in **samples #1-4**, which were of comparable densities after densification, the coercivity values decrease slightly from 15 kOe to 12 kOe, but remain high compared to typical rare earth-based permanent magnets. These coercivity values corroborate the XRD results which indicate that the ϵ -Fe₂O₃ phase is the dominant phase in these samples. The coercivity values of the samples with varying density (**samples #4-6**) are also consistent with XRD results, with increased density leading to decreased coercivity, which can be attributed to formation of a secondary iron oxide phase. It is proposed that the higher pore concentration (lower density) acts as diffusion inhibitor in conjunction with the silica shell, which leads to a slower growth rate of the Fe₂O₃ particles, allowing for a larger quantity of ϵ -Fe₂O₃ to form. The ratio of the primary XRD peak of the secondary iron oxide phase (at 33.2° for α -Fe₂O₃) to the primary ϵ -Fe₂O₃ peak (the (122) plane at 33.0°) was found for each sample and compared to the coercivity (figure 5.4b). The results were consistent with previously discussed behaviors throughout all samples, with a high peak intensity ratio of ϵ -Fe₂O₃ to α -Fe₂O₃ corresponding to higher coercivity. **Sample #6**, which had the lowest coercivity of 7.5 kOe, also exhibited the lowest ratio of ϵ -Fe₂O₃ to α -Fe₂O₃ primary peaks, indicating that the ϵ -Fe₂O₃ phase is likely significantly less prominent, and thus, less magnetically dominant. The lowest density sample also had the highest coercivity among the IO-90 samples as well as the highest ratio of ϵ -Fe₂O₃ peak intensities, which is consistent with the role of pores being akin to diffusion inhibition sites, allowing for a greater control of the Fe₂O₃ particle growth rate.

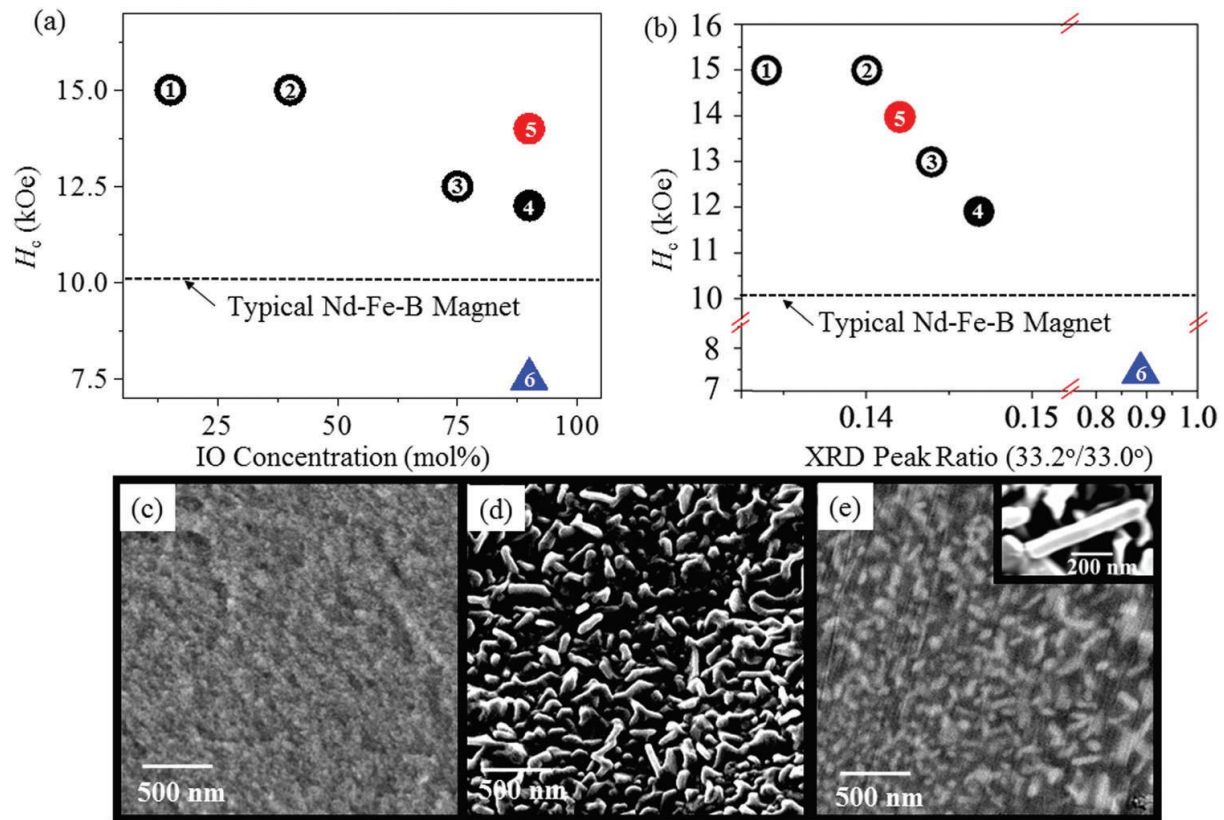


Figure 5.4 (a) Plot of coercivity vs IO concentration, (b) plot of coercivity vs primary peak ratio between ϵ -Fe₂O₃ and α -Fe₂O₃, SEM micrographs of (c) bulk fracture surface prior to annealing, (d) bulk fracture surface after annealing, and (e) bulk fracture surface after annealing and polishing of the surface[57]

SEM micrographs were obtained for the fracture surface of the IO-90, 89% dense, bulk samples before annealing (**Figure 5.4c**), after annealing (**Figure 5.4d**), and after annealing and polishing of the fracture surface (**Figure 5.4e**). The micrograph of the fracture surface prior to the annealing step reveals relatively uniform roughness throughout, suggesting that the constituent grains are relatively small. Following the annealing step, a nanorod-like morphology is observed, reminiscent of the nanorods seen in the powder samples, but with much closer proximity between the nanorods, which is consistent with the results expected in a 90 mol% cation concentration sample with a significantly decreased silica matrix thickness. Measurements of the nanorods resulted in average dimensions of 56 nm x 195 nm with a standard deviation of 11.2 nm for the short axis and 48.3

for the long axis. Additionally, there was no evidence of large isolated pores, corroborating the high relative density values obtained from the Archimedes density measurements. The transition in microstructure from **Figure 5.4c** to **Figure 5.4d** suggests that a similar growth behavior is occurring in the bulk sample as in the powder, providing further evidence that the ϵ -Fe₂O₃ formation is occurring in the bulk sample through a comparable mechanism. Analysis of the polished surface micrograph (**Figure 5.4e**) suggests through the Z-contrast difference between Fe-rich and Si-rich areas that the lighter areas are ϵ -Fe₂O₃ with minor α -Fe₂O₃ content, and the dark areas are cristobalite (SiO₂). From the polished-surface micrograph, it can be seen that there is a homogenous distribution of ϵ -Fe₂O₃ nanorods with a comparatively thin SiO₂ matrix. The higher resolution image of a nanorod (**Figure 5.4e** inset) shows a nanorod-like structure similar to those seen in the powder samples, further corroborating the XRD and magnetometry data, and proves the success in obtaining a bulk composite material comprised primarily of ϵ -Fe₂O₃.

Magnetic characterization of the IO-15 and IO-90 samples included room-temperature hysteresis loops (moment vs field at 300K), low-temperature hysteresis (moment vs field at 20K), field-cooling (moment vs temperature), and ferromagnetic resonance. Room-temperature hysteresis (**Figure 5.5a**) comparison of IO-15 (**sample #1**) and IO-90 (**sample #4**) with similar densities shows a slight drop in coercivity with increased cation concentration, as expected due to the formation of minor amounts of α -Fe₂O₃. However, more importantly, there is a drastic increase in both remanent and maximum magnetization in the higher Fe₂O₃ content sample, which can be attributed to the significant reduction of SiO₂ – a diamagnetic phase which serves to dilute the concentration of magnetic moments in the bulk sample. Most importantly, it should be noted that previous works reported the magnetization values of ϵ -Fe₂O₃ as mass-normalized (emu/g) due to the existence of the phase only in nanopowder form, whereas this work reports the first volumetric

magnetization value, due to the high iron oxide content in the bulk composite structure. Magnetization values of bulk permanent magnets are often reported in volumetric magnetization as it more accurately reflects the importance of the magnet dimensions. Because the samples produced in this work are dense, bulk, composite materials (as shown in the inset of **Figure 5.5a**), it is accurate to describe the magnetization with volume-normalized values. To compare, the remanent magnetization of pure ϵ -Fe₂O₃ was calculated by taking literature magnetization values and the theoretical density of ϵ -Fe₂O₃. The range of remanent magnetization was found to be 14-30 emu/cm³, slightly higher than the 10 emu/cm³ found in the IO-90 sample, which is consistent with the presence of some silica content as well as some residual porosity. In contrast, the IO-15 sample showed a significantly lower remanent magnetization of ~ 1 emu/cm³, which is consistent with the significantly reduced iron oxide content due to the high silica concentration.

The low temperature hysteresis loops were measured at 20K (**Figure 5.5b**) and reveal a significant decrease in coercivity for both the high (**sample #4**) and low (**sample #1**) iron oxide content samples. The exact nature of the magnetic behavior of ϵ -Fe₂O₃ remains unclear, as it has been variously described as both a canted-antiferromagnet and non-collinear ferromagnet with a low-temperature magnetic structure transition which has been variously described as either a square-wave incommensurate magnetic structure or a second canted antiferromagnetic state. While the magnetic transition may not be well understood, the low-temperature hysteresis results of the IO-15 sample are consistent with the decrease in coercivity in powder samples from previous reports[27], [42], [55], [117], marked by a significant decrease in coercivity. The second magnetic transition that has been associated with ϵ -Fe₂O₃ occurs around 20K, and is due to a transition from a fully antiferromagnetic state to a second canted-antiferromagnetic state. Since the magnetic hysteresis were measured at this temperature, it is expected that the coercivity should drastically

decrease, due to the transitional magnetic state. The IO-90 sample however, exhibited a much smaller decrease in coercivity, which may be due either to the significantly higher volume content of ϵ -Fe₂O₃ leading to a coupling effect, or a greater distribution in grain size.

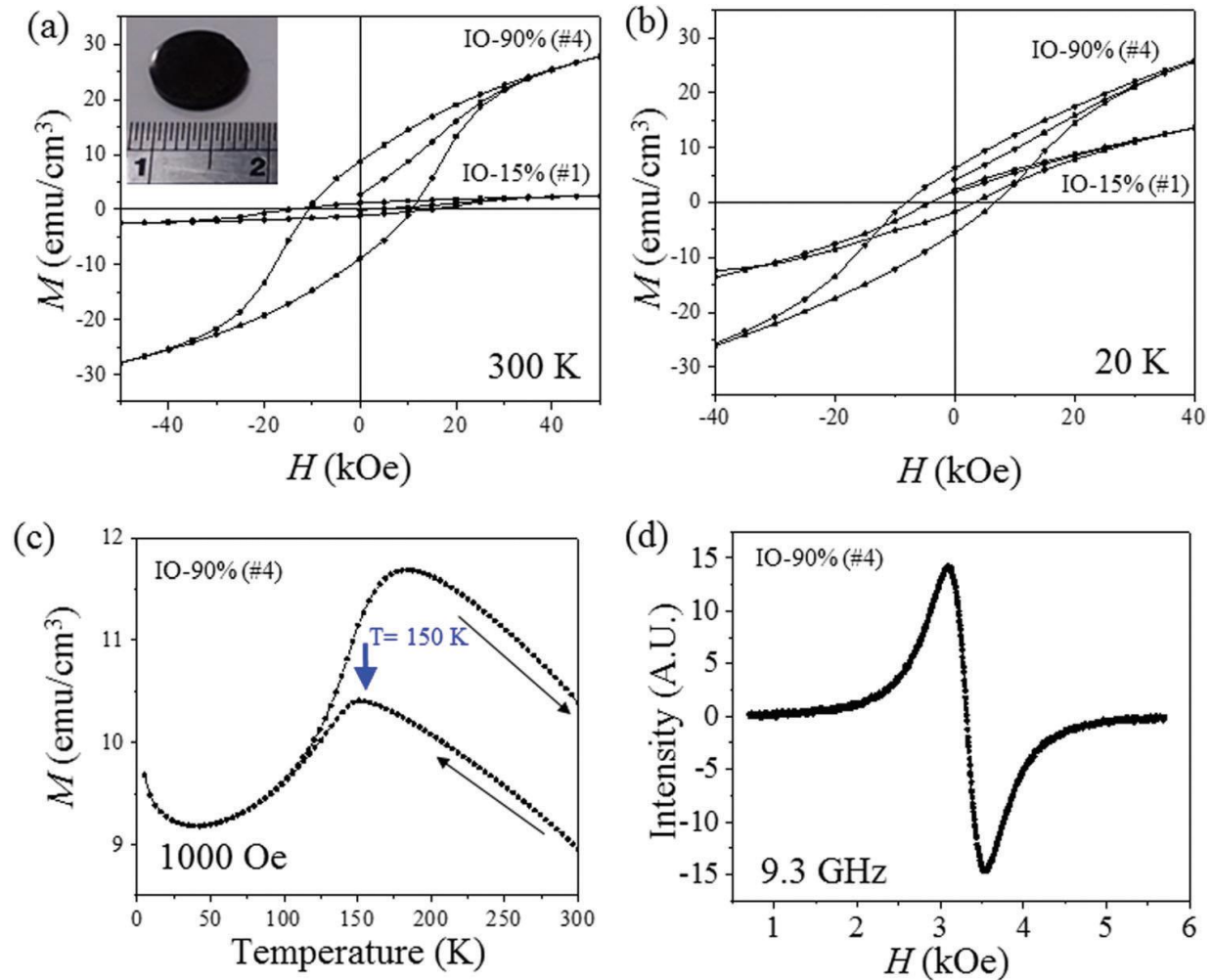


Figure 5.5 (a) Room temperature M-H loops of IO-15 vs IO-90 samples of comparable density, (b) low-temperature M-H loops of IO-15 vs IO-90 samples, (c) field cooling of IO-90 sample, (d) FMR measurement of IO-90 sample[57]

As discussed in previous sections, the magnetic transitions due to magnetic reordering at different temperatures is strongly indicative of the overall crystalline structure, and hence, the phase as well. Similar to samples discussed in previous sections, field-cooling measurements were

performed on the IO-90 sample (sample #4) with an applied field of 1000 Oe and temperature was swept from room temperature (300K) to 2K, and an increase in the magnetization was observed with decreasing temperature until a peak and abrupt decrease at 150K, followed by an increase in magnetization at 25K. The two transitions observed are consistent with the transitions reported for powder samples of ϵ -Fe₂O₃, particularly the Morin-like transition which is the most prominent of transitions in the system, and has been reported to be between 110-150K. The Morin-like transition at 150K marks a change from the first canted-antiferromagnetic state to a fully antiferromagnetic state. This is analogous to the Morin transition which is seen in α -Fe₂O₃ ~260K, and marks a transition from a slightly canted antiferromagnetic state at room temperature to a fully antiferromagnetic state. The lack of a Morin transition at higher temperatures despite the XRD evidence of the existence of a secondary Fe₂O₃ phase indicates that the ϵ -Fe₂O₃ phase is magnetically dominant in the sample. It is possible that the Morin transition of α -Fe₂O₃ in the sample is masked due to a distribution of particle sizes, as the Morin transition temperature has been reported to be size dependent for α -Fe₂O₃. At 25K, the increase in magnetization is consistent with the second transition that has reported for ϵ -Fe₂O₃, which is typically described as a second canted-antiferromagnetic state, and it behaves similarly to the first canted-antiferromagnetic state at room temperature. The results of the magnetization vs temperature measurements indicate that ϵ -Fe₂O₃ is the dominant phase in the IO-90 sample. Ferromagnetic resonance measurements were performed as further verification of the ϵ -Fe₂O₃ phase, where the resonance behavior closely matches that of ϵ -Fe₂O₃ phases, rather than those of other Fe₂O₃ or barium-ferrite phases[105], [106], [118]–[120]. The results of the ferromagnetic resonance measurements further verify the magnetic dominance of the ϵ -Fe₂O₃ phase in the IO-90 sample.

5.4. Dense Magnetic Fe-O/Na-Si-O Composites

The Na-Si-O-15 and Na-Si-O-90 powders discussed in **Chapter 4** were also densified following the processing route discussed in **section 5.3**. Interestingly, the onset of densification in the Na-Si-O samples is significantly lower than that of the Si-O samples, as shown in **Figure 5.7**. While an increase in extension while maintaining a constant load can typically imply the onset of densification (as can be seen at $\sim 380^\circ\text{C}$ in the Si-O-15 sample) the lack of extension increase in the Na-Si-O samples while under constant load may be attributed to the densification occurring at a sufficiently low temperature ($\sim 320^\circ\text{C}$) such that the applied load is still in the process of increasing. This would imply that the substitution of the Si-O shell with an Na-Si-O shell allows for lower temperature CAPAD processing and densification.

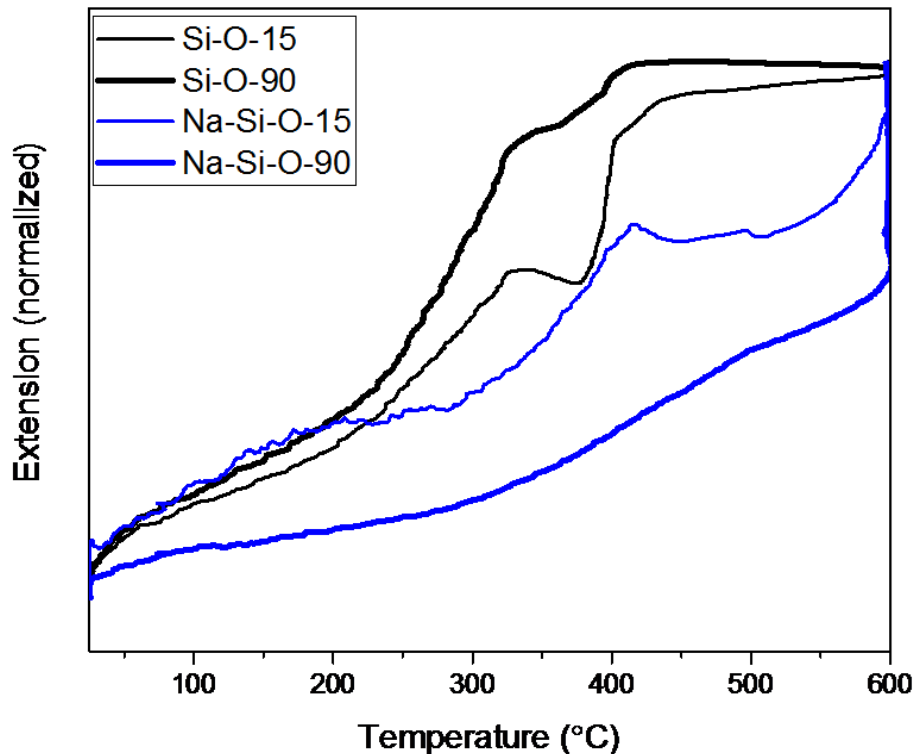


Figure 5.6 Normalized extension curves of Na-Si-O and Si-O samples with comparable cation concentrations plotted versus temperature

While the extension vs densification curves alone indicate a drastically densification behavior, the proposition that the onset of densification in the Na-Si-O samples begins at $\sim 320^\circ\text{C}$ can be indirectly verified by the resulting densities. **Table 5.2** shows the temperature at which the onset of densification occurs for each Si-O and Na-Si-O sample, as well as the green body densities, resulting relative densities, and resulting coercivities of the samples after annealing. It can be seen that the Na-Si-O show a higher relative density ($\sim 99.0\%$) after densification. It is proposed that the Na-Si-O shell may allow for lower temperature densification. The results of the densification aligns well with the hypothesis that the silica is the primary densifying medium in the $\epsilon\text{-Fe}_2\text{O}_3/\text{SiO}_2$ work. Furthermore, the resulting coercivity of the dense Na-Si-O-15 sample annealed at 875°C was 13.0 kOe, which is sufficiently high to be attributable to $\epsilon\text{-Fe}_2\text{O}_3$ being the magnetically dominant phase.

Table 5.2 The densification onset temperature, densities measured by Archimedes method, resulting relative densities and coercivities for the Si-O and Na-Si-O samples. The * indicates that the sample was annealed at 875°C instead of 1025°C

Sample	$T_{\text{densification start}} (^\circ\text{C})$	Density (g/cm^3)	Relative Density (%)	H_c (kOe)
Si-O-15	385	2.86	94.1	15.0
Si-O-40	390	3.27	88.4	15.0
Si-O-75	390	3.87	83.9	12.5
Si-O-90	N/A	N/A	< 50.0	N/A
Na-Si-O-15	320	2.84	99.0	13.0*
Na-Si-O-90	330	4.93	99.0	N/A

Figure 5.7 shows the hysteresis loops for the bulk Na-Si-O-15 and Si-O-15 samples annealed at 875°C and 1025°C, respectively. It can be seen that the coercivity of the Si-O-15 sample is ~15.0 kOe, which agrees with the work discussed in **Section 5.3**. The densified Na-Si-O-15 sample shows a coercivity of ~13.0 kOe. Both samples had magnetization values ~1.3 emu/cm³, which are similar to previously synthesized bulk, 15 mol% samples, as shown in **Section 5.3**. It is worthwhile to note that these samples are reported in volumetric magnetization, which is possible due to the samples being dense (>94% relative density), bulk (millimeter-scale) samples. These results agree with the findings discussed in both **Section 4.4** and **Section 5.3**, in which it was found that the substitution of an Na-Si-O shell for the standard Si-O shell yielded comparable nanorod growth at a significantly lower temperature and produced samples with a high coercivity which can be attributed to the ϵ -Fe₂O₃ phase. Upon densification, the samples showed a slight decrease in coercivity which can be attributed to an increase in secondary phases, but retained high coercivity values (>12 kOe) which are within the expected range for the ϵ -Fe₂O₃ phase.

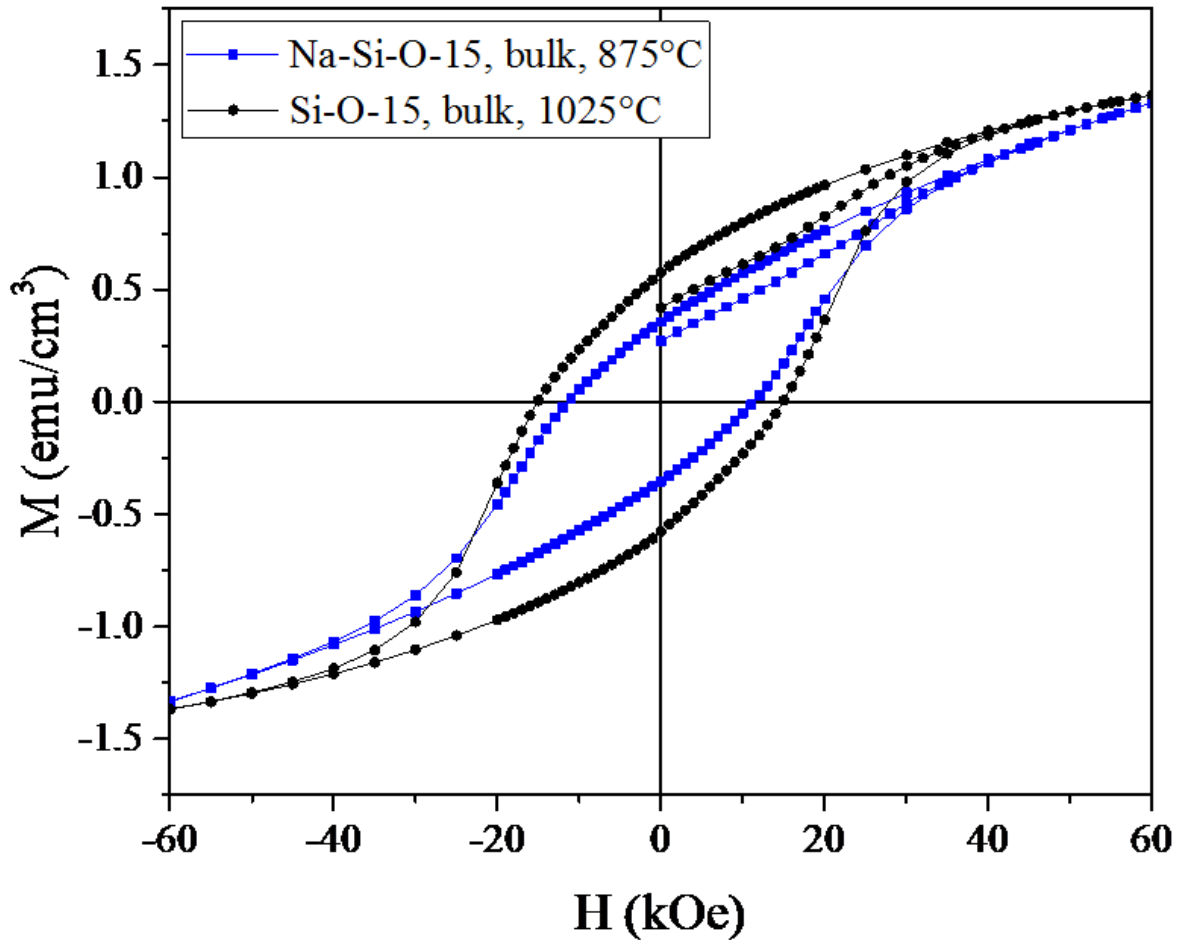


Figure 5.7 Hysteresis loops of bulk Na-Si-O-15 and Si-O-15 samples annealed at 875C and 1025C, respectively

The presence of secondary phases in the densified Na-Si-O-15 sample is confirmed with the field cooling measurements shown in **Figure 5.8**. It can be seen that two transitions occur – one at 150K, which can be attributed to the Morin-like transition of ϵ -Fe₂O₃, and a second transition ~120K, which can be attributed to the existence of β -Fe₂O₃. These results agree well with previous studies which indicated that the β -Fe₂O₃ phase is stabilized at larger sizes than ϵ -Fe₂O₃ and often coexists with other phases of Fe₂O₃. Furthermore, these results verify the hypothesis proposed in **Chapter 4** holds true, in that the addition of sodium should increase the diffusivity of Fe/O while

maintaining the same kinetics. The coexistence of β -Fe₂O₃ and ε -Fe₂O₃ indicates that the Na-Si-O shell allows for increased diffusivity of Fe/O, which makes it possible to stabilize the ε -Fe₂O₃ phase in a bulk composite at significantly lower temperatures.

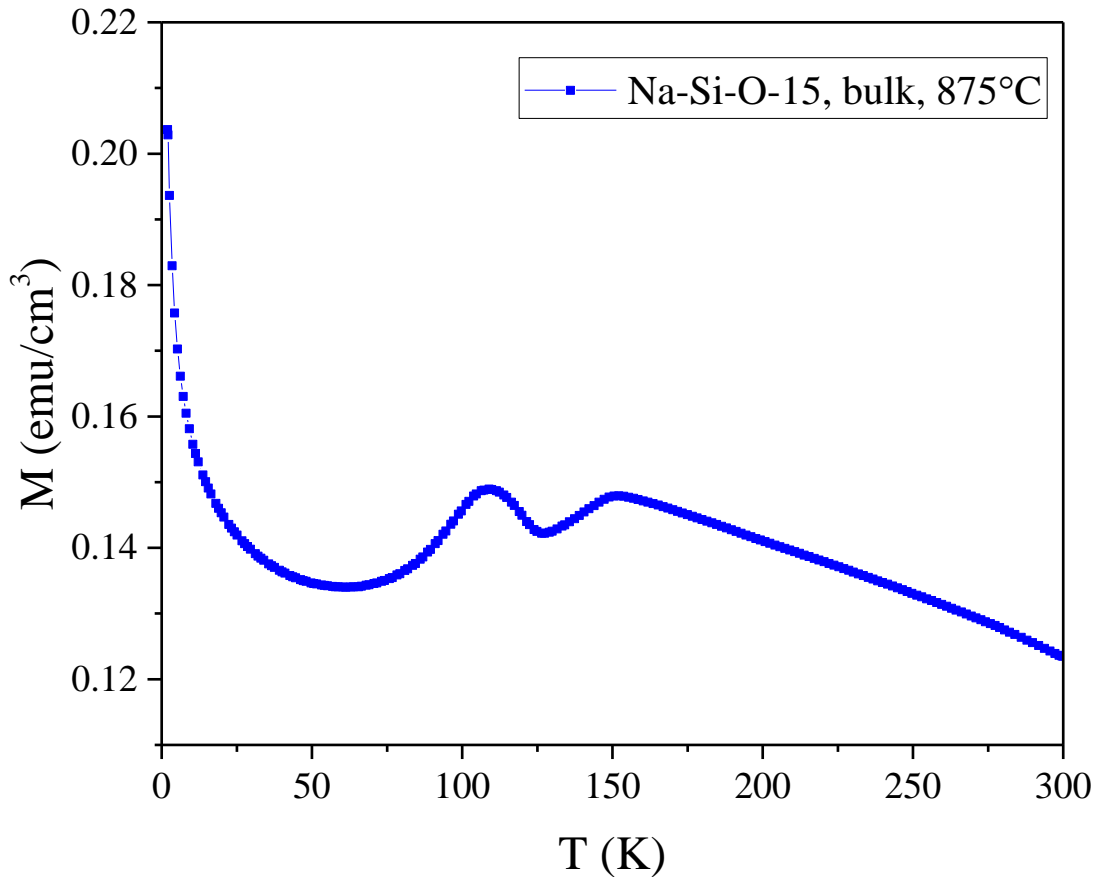


Figure 5.8 Field cooling of densified Na-Si-O-15 sample, annealed at 875°C. Two transitions occur which can be attributed to the presence of β -Fe₂O₃ which is stable at a larger size range than ε -Fe₂O₃

Figure 5.9 shows the coercivity of the densified Na-Si-O-15 and Si-O-15 samples annealed at varying temperatures. It can be seen that the Na-Si-O-15 sample reaches a maximum coercivity of 13.0 kOe at 875°C, while the Si-O-15 sample has a lower coercivity of 9.5kOe after annealing at

the same temperature. The Si-O-15 sample reaches a maximum coercivity of 15 kOe after annealing at 1025°C. From the results shown in **Figure 5.9**, it can be seen that the formation temperatures of ϵ -Fe₂O₃ in a bulk composite comprised of Fe-O and Na-Si-O/Si-O follow the same trend as those shown in **Section 4.4**. The increase in coercivity with increasing temperature, followed by a rapid drop-off in coercivity at sufficiently high temperatures follows the patterns shown in previous work[5], [28].

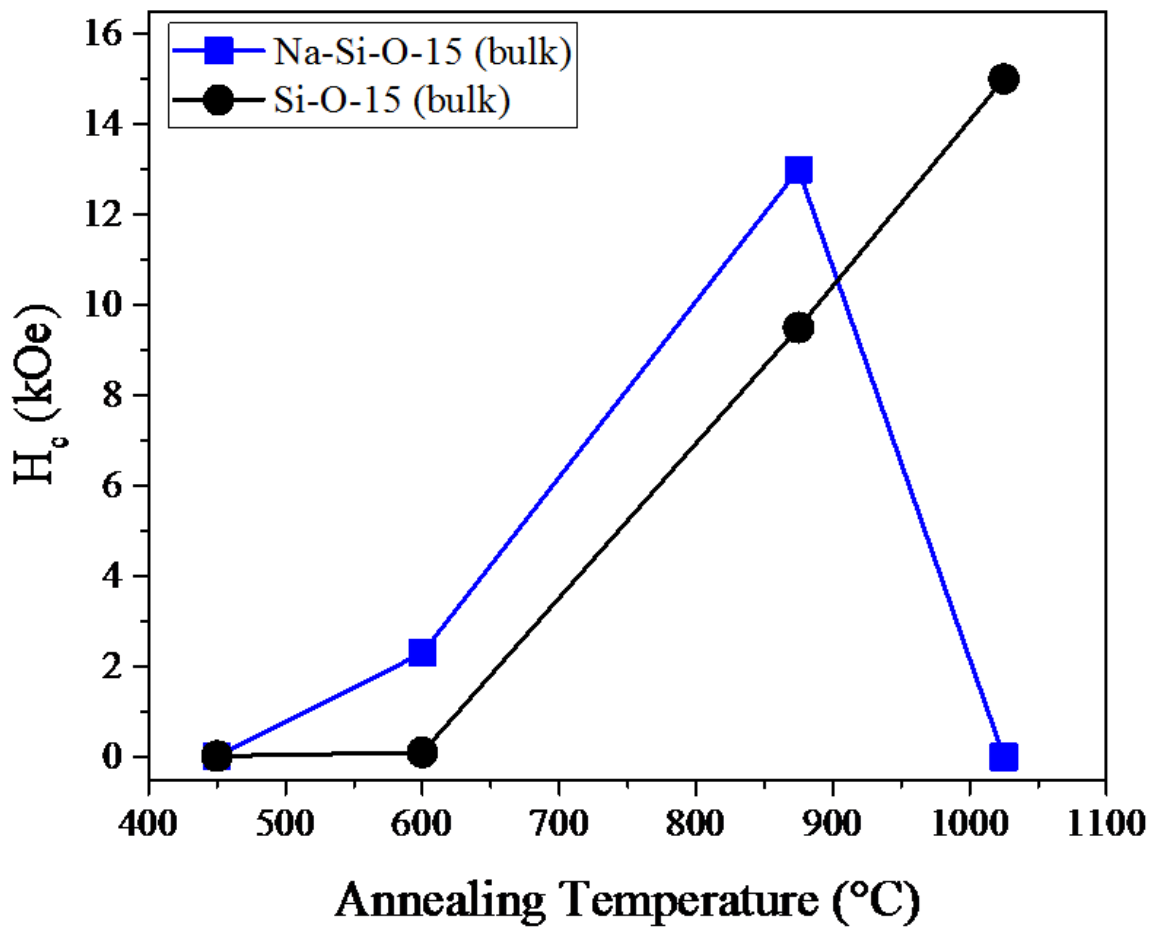


Figure 5.9 Coercivity of densified Na-Si-O-15 and Si-O-15 samples annealed at 450, 600, 875, and 1025°C

The results of this work indicate that the substitution of the Si-O shell with an Na-Si-O shell significantly decreases the required energy in processing both during and post densification. This

allowed for the formation of ϵ -Fe₂O₃ in a bulk composite at significantly lower temperatures. The initial results from densification of Na-Si-O shell samples are promising, and hold the potential for drastically reducing the required energy input during processing of bulk, composite magnetic materials.

5.5. Summary of Chapter 5

In summary, the primary goal of this work was to produce a dense, bulk, nanocomposite with a high ϵ -Fe₂O₃ content, and was achieved by adjusting the chemical synthesis to achieve the desired iron oxide concentration, then rapidly densifying the as-synthesized powders through CAPAD processing. The resulting samples with comparably high densities (>80% relative density) maintained a high coercivity of 12-15 kOe, which compares favorably to those of rare earth-based magnets[121], [122]. A significant decrease in coercivity was observed when both iron oxide concentration and density were high, which is attributed to an increase in formation of secondary phases due to decreased diffusion length and increased grain growth, since the stability of ϵ -Fe₂O₃ is size-dependent. A high ϵ -Fe₂O₃ concentration of 90 mol% was achieved in the bulk samples, and was verified through XRD, SEM, and VSM measurements. The resulting bulk, composite permanent magnets retained the remarkably high coercivity that is associated with the metastable ϵ -Fe₂O₃ phase while also significantly increasing the magnetic content. Further work was done with the Na-Si-O shell samples, in which the Na-Si-O-15 powders were densified and annealed at varying temperatures, then magnetically characterized and compared to the densified Si-O-15 samples. The initial results indicate that the addition of Na to the Si-O shell leads to a decreased densification temperature as well as a decreased ϵ -Fe₂O₃ formation and stabilization temperature.

These results offer a promising possibility of utilizing metastable phases of earth-abundant and environmentally benign materials in bulk composite magnets as an alternative to rare earths which require environmentally damaging refinement processes.

Chapter 5 is co-authored by Dr. Jason R. Morales, Dr. Yasuhiro Kodaera, and Professor Javier E. Garay, and is published in *Journal of Materials Chemistry C* 2017,**5**, 7911-7918. The dissertation author was the primary investigator and author on this paper.

6. SUMMARY AND CONCLUSIONS

Iron oxides are earth abundant and environmentally friendly materials which have been historically significant in the development of magnetic materials for various technological applications. Specifically, iron (III) oxide (Fe_2O_3) is of particular interest due to the existence of five crystallographic polymorphs, four of which are magnetically distinct. Among these four magnetically distinct polymorphs, three are considered to be metastable – the ferromagnetic $\gamma\text{-Fe}_2\text{O}_3$, the canted-antiferromagnetic $\varepsilon\text{-Fe}_2\text{O}_3$, and paramagnetic $\beta\text{-Fe}_2\text{O}_3$ – with both temperature and size, while the fourth polymorph – the antiferromagnetic $\alpha\text{-Fe}_2\text{O}_3$ – is considered to be the most stable phase. Particularly interesting is the $\varepsilon\text{-Fe}_2\text{O}_3$ phase, which exhibits a remarkably high coercivity which is often comparable or higher than rare earth-based magnets (such as neodymium iron boron magnets). However, while the metastable phase had previously been well studied as a nanophase (nanoparticles, nanorods, thin films, etc.), the size-dependence had thus far rendered it an unviable candidate for use in bulk permanent magnetic applications. This work sought to first understand and decouple the size and temperature effects on the formation and stabilization of the $\varepsilon\text{-Fe}_2\text{O}_3$ phase, then effectively utilize this knowledge to effectively control the phase transformation. Following this, the goal was to utilize the metastable $\varepsilon\text{-Fe}_2\text{O}_3$ phase as the primary component in a bulk, functional permanent magnetic material.

Prior work by Navrotsky, et al.[6] had proposed and demonstrated a strong link between the surface energy and free energy of materials – most notably, the various iron oxide phases and compositions. Specifically, the surface energy is determined by morphology and particle size, and the free energy describes the stability of various phases under specific conditions. The implications of this prior work led this work to apply a grain growth kinetics model to the particle sizes reported

in work by Sakurai, et al.[5], in which the transformation between four phases of Fe_2O_3 was observed and it was demonstrated that the dominant phase was dependent on the particle size. From this kinetics analysis, it was seen that a diffusion-mediated growth model was an excellent fit for the growth behavior of spherical Fe_2O_3 nanoparticles constrained in a growth-controlling mesoporous silica matrix. Similarly, the same particle growth model was found to fit for the growth behavior of both the long and short axes of $\epsilon\text{-Fe}_2\text{O}_3$ nanorods. The close match of a grain growth model further implied that the phase transformations of Fe_2O_3 may be predicted by grain size and thus should be controllable by modifying the growth behavior.

A modified reverse-micelle/sol-gel process adapted from prior work was used to synthesize iron oxide/silica core-shell powders with initial grain sizes of <50 nm. This process was modified in two ways: adding sodium to form a sodium-silicate shell and increase diffusivity of iron, and systematically decreasing the shell thickness to increase iron oxide content. The samples were characterized with SEM, XRD, and VSM for microstructural, crystallographic, and magnetic properties. The work was split into two primary projects: project I – understanding and decoupling the size and heat effects on phase transformations, then manipulating the growth behavior to decrease processing energy requirements, and project II – utilizing the desirable metastable phases in a bulk, functional, composite.

The work discussed in **Chapter 4** focused on the ability to control the phase formation conditions by utilizing a sodium silicate shell to increase diffusivity of iron through the diffusion matrix and allow for comparable grain growth and significantly lower temperatures. It was shown that nanorods of comparable dimensions to those of the pure silica matrix samples could be formed at a lower temperature, and the resulting magnetic properties and magnetic structure indicated the dominance of the $\epsilon\text{-Fe}_2\text{O}_3$, verifying that the particle size was dominant in determining the stability

of various phases. Additionally, a magnetic field was applied during the annealing of the powders, and it was found that the applied field significantly reduced the temperature at which magnetic ordering is formed in the samples, implying that the externally applied field may assist in the nucleation and formation of the ferromagnetic γ -Fe₂O₃ phase from the iron hydroxide precursor. This is further confirmed by field-cooling measurements of samples annealed both with and without an external magnetic field, and it was seen that the low temperature behavior of the magnetically annealed sample at 600°C appeared to behave like γ -Fe₂O₃, while the sample annealed without field at 600°C appeared to behave like a typical paramagnetic material.

The work discussed in **Chapter 5** focused on the utilization of the knowledge gained from project I, and sought to produce a bulk, functional magnet based on the ϵ -Fe₂O₃ phase. Due to the size-dependent metastability, a composite material was produced, with the SiO₂ phase acting as the densifying matrix while restricting the growth of Fe₂O₃ nanoparticles. The diamagnetic silica content was systematically decreased until a cation concentration of 90 mol% was achieved. Crystallographic and microstructural analysis indicated that ϵ -Fe₂O₃ was dominant in all of the samples, even at high concentration. Magnetic characterization indicated that ϵ -Fe₂O₃ was magnetically dominant throughout and a bulk, rare earth-free magnetic was produced with high coercivity. In addition to the densification of a bulk composite with high ϵ -Fe₂O₃ content, the Na-Si-O shell samples were also densified. It was found that by replacing the Si-O shell with an Na-Si-O shell, the temperature where densification onset occurs was significantly lowered, and further verifies that the proposal that the SiO₂ acts as the densifying medium in ϵ -Fe₂O₃/SiO₂ composite work is accurate.

This work demonstrated a decoupling of size and temperature effects on the formation and magnetic properties of the metastable ϵ -Fe₂O₃ phase, thereby allowing for the production of a bulk,

permanent magnet comprised of the metastable phase, with coercivities comparable to those of rare earth-based magnets. A promising future direction is to utilize these findings to produce exchange-coupled permanent magnets based on metastable phases of environmentally-friendly and earth-abundant materials.

APPENDIX

A-1 Grain Growth Kinetics Calculations

Grain sizes were determined by measuring between 250-500 nanorods then averaged. The initial grain size was assumed to be negligible, as the synthesis process involves the growth of Fe₂O₃ from a precipitate.

$$d^2 - d_0^2 = k * t$$

d = average final grain size

*d*₀ = initial grain size (assumed to be 0)

t = time at temperature (seconds)

k = rate constant (m²s⁻¹)

$$k = k_0 \exp\left(\frac{E_A}{k_B T}\right)$$

k = growth constant

*k*₀ = pre - exponential constant

*E*_A = activation energy

*k*_B = Boltzmann constant (8.617 × 10⁻⁵ $\frac{ev}{K}$)

T = temperature (K)

A-2 Grain Growth Kinetics Calculation Results

Grain growth kinetics were calculated for data adapted from literature[5], [24], [25], [73] as well as from the results found in this work. The grain growth constants were used to determine the kinetics of growth for the various diffusion control methods.

Table A.1 Calculation of grain growth constant (k) for values reported in literature as well as values found in this work

d (nm)	d(m)	Temp	1/T	k (m ² /s) (d ₀ =0)	ln(k) (d ₀ =0)
4	0.000000004	900	0.000852	1.11111E-21	-48.24892644
8	0.000000008	1000	0.000785	4.44444E-21	-46.86263208
19	0.000000019	1100	0.000728	2.50694E-20	-45.1326372
25	0.000000025	1150	0.000703	4.34028E-20	-44.58376351
34	0.000000034	1200	0.000679	8.02778E-20	-43.96879411
40	0.00000004	1225	0.000667	1.11111E-19	-43.64375625
45	0.000000045	1250	0.000656	1.40625E-19	-43.40819018
3	0.000000003	80	0.00283	6.25E-22	-48.82429058
5	0.000000005	900	0.000852	1.73611E-21	-47.80263933
20	0.00000002	1000	0.000785	2.77778E-20	-45.03005061
50	0.00000005	1050	0.000756	1.73611E-19	-43.19746915
5	0.000000005		0.003659	1.73611E-21	-47.80263933
80	0.00000008		0.003659	4.44444E-19	-42.25746189
200	0.0000002		0.003659	2.77778E-18	-40.42488043
33.1	3.31E-08	875	0.000871	1.52168E-19	-43.32930141
219	0.000000219	875	0.000871	6.66125E-18	-39.55022452
155	0.000000155	875	0.000871	3.33681E-18	-40.24151775
651	0.000000651	875	0.000871	5.88613E-17	-37.37134869
204	0.000000204	1025	0.00077	2.89E-18	-40.38527517
26	0.000000026	1025	0.00077	4.69444E-20	-44.50532208
10	0.00000001	450	0.001383	1.38889E-20	-45.72319779

A-3 Additional Magnetic Hysteresis Measurements

A-3.1 Hysteresis of Na-Si-O-15 samples

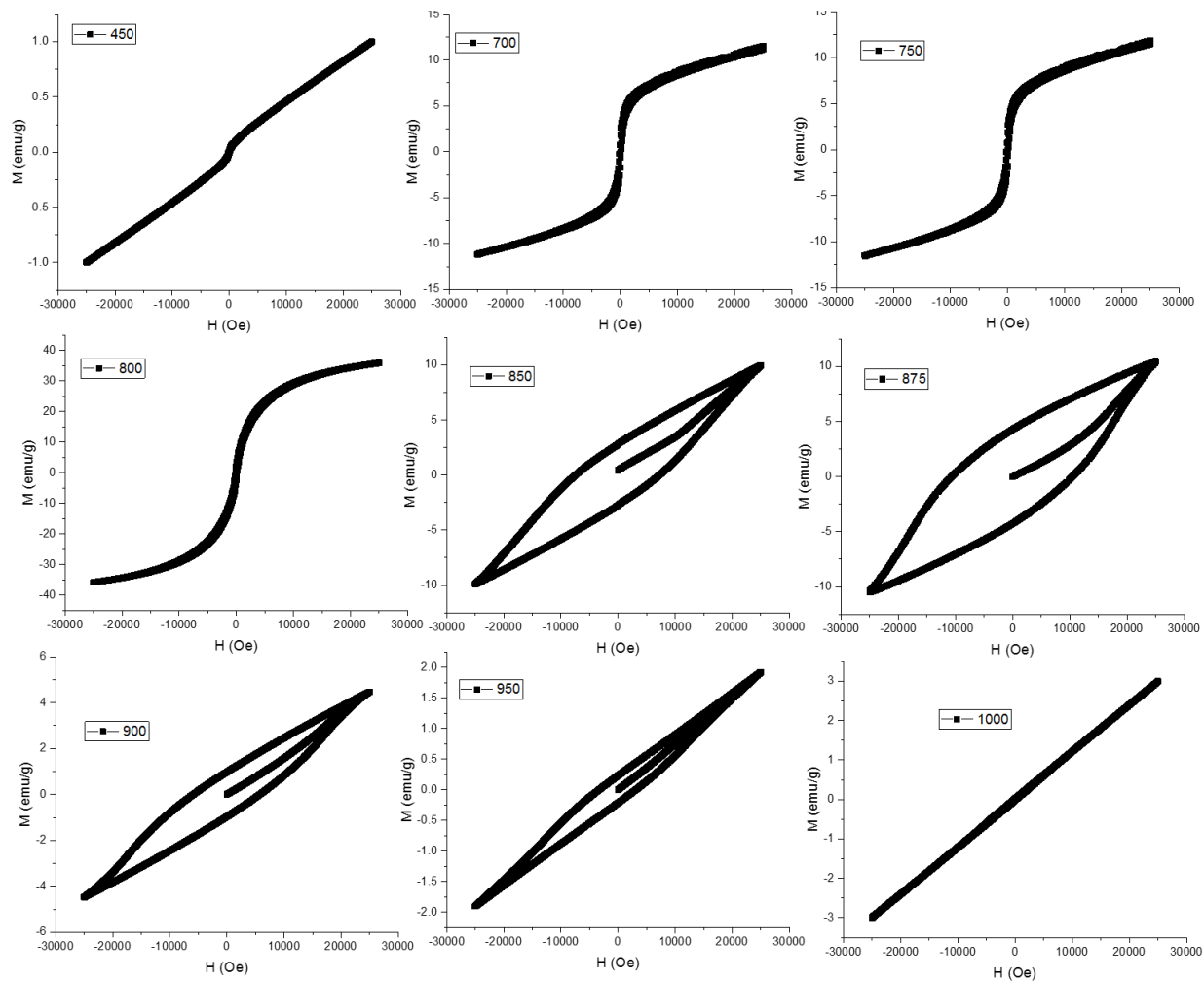


Figure A.1 Hysteresis loops of Na-Si-O-15 samples annealed at temperatures ranging from 450-1000°C

A-3.2 Hysteresis of Si-O-15 samples

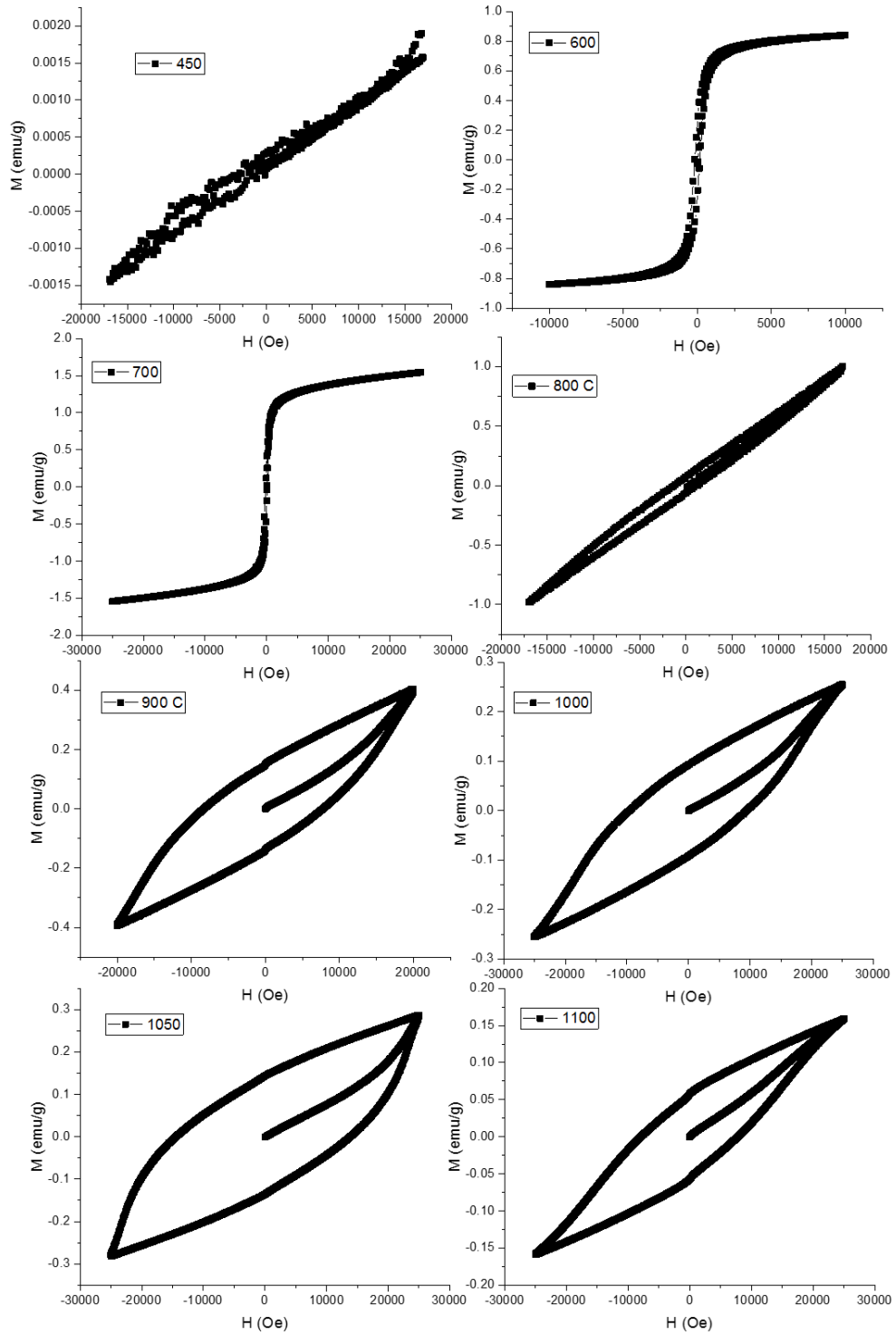


Figure A.2 Hysteresis loops of Si-O-15 samples annealed at varying temperatures from 450-1100°C

A-3.3 Hysteresis of Si-O-90 Samples

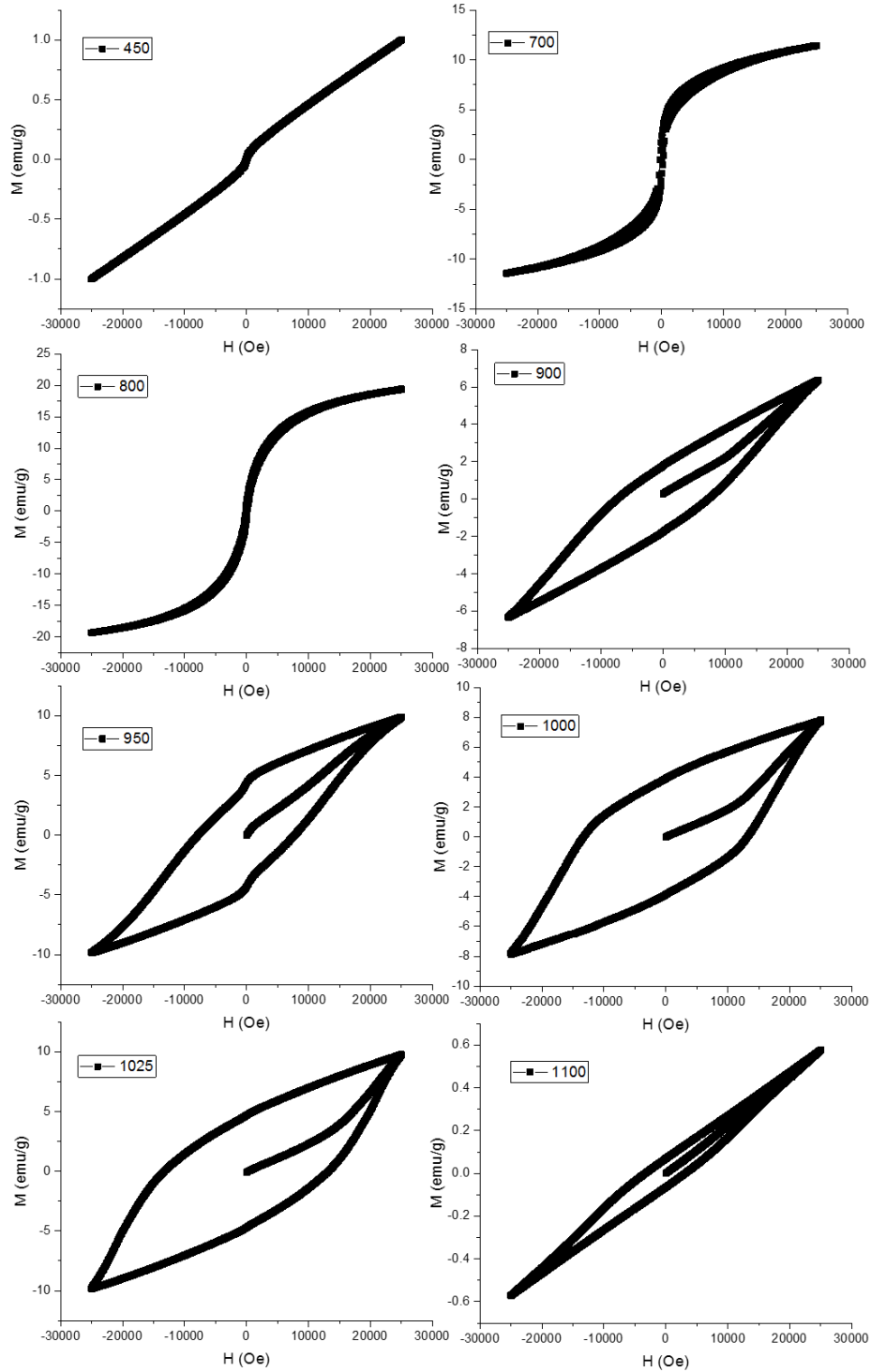


Figure A.3 Hysteresis loops of Si-O-90 samples annealed from 450-1100°C

A-3.4 Hysteresis of Densified Na-Si-O-15 and Si-O-15 Samples

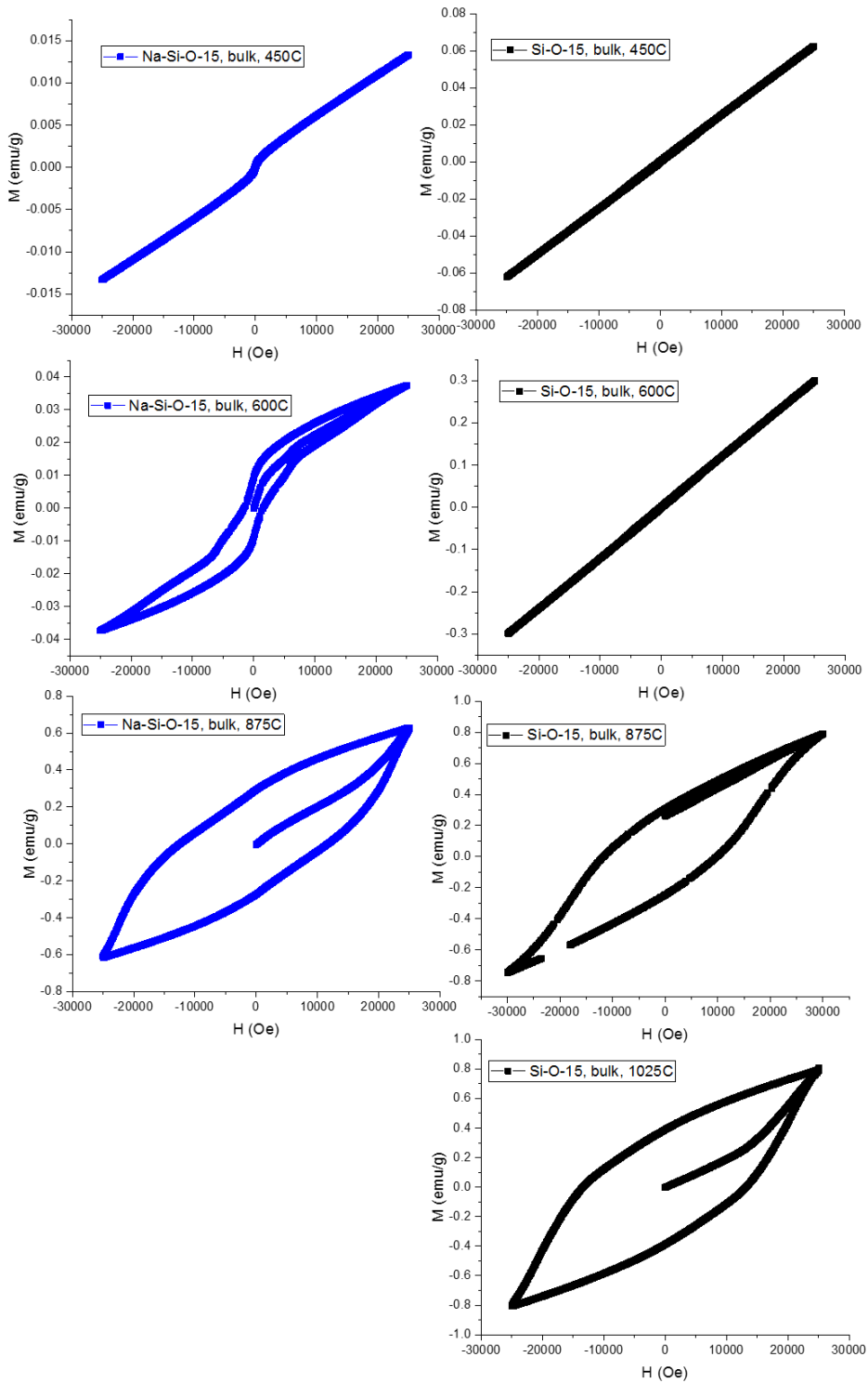


Figure A.4 Hysteresis of densified Na-Si-O-15 and Si-O-15 samples annealed at 450, 600, 875, and 1025°C

A-4 Surface Area to Volume Ratios

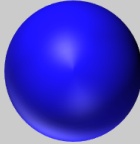
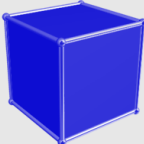

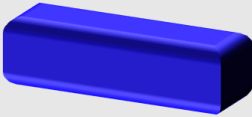

SHAPE	SURFACE AREA	VOLUME	SA/V
	$4\pi r^2$	$\frac{4}{3}\pi r^3$	$\frac{3}{r}$
	$6a^2$	a^3	$\frac{6}{a}$
	$2\sqrt{3}a^2$	$\frac{\sqrt{2}}{3}a^3$	$\frac{3\sqrt{6}}{a}$
	$4al + 2a^2l$	a^2l	$\frac{4}{a} + 2$
	$2\pi rl + 2\pi r^2$	πr^2l	$\frac{2}{r} + \frac{2}{l}$

Figure A.5 Surface area-to-volume ratios of various geometries

REFERENCES

- [1] H. W. Meyer, *A History of Electricity and Magnetism*. Norwalk, Connecticut: Burndy Library, 1972.
- [2] B. D. Cullity and C. D. Graham, *Introduction to Magnetic Materials*, 2nd ed. Wiley-IEEE Press, 2008.
- [3] J. Paul and G. Campbell, “Investigating Rare Earth Element Mine Development in EPA Region 8 and Potential Environmental Impacts,” pp. 1–35, 2011.
- [4] R. M. Cornell and U. Schwertmann, *The Iron Oxides*, 2nd ed. 2003.
- [5] S. Sakurai, A. Namai, K. Hashimoto, and S. Ohkoshi, “First Observation of Phase Transformation of All Four Fe₂O₃ Phases ($\gamma \rightarrow \varepsilon \rightarrow \beta \rightarrow \alpha$ -Phase),” *J. Am. Chem. Soc.*, vol. 131, no. 51, pp. 18299–18303, Dec. 2009.
- [6] A. Navrotsky, L. Mazeina, and J. Majzlan, “Size-driven structural and thermodynamic complexity in iron oxides,” *Science*, vol. 319, no. 5870, pp. 1635–8, Mar. 2008.
- [7] J. Tuček, L. Machala, S. Ono, A. Namai, M. Yoshikiyo, K. Imoto, H. Tokoro, S. Ohkoshi, and R. Zbořil, “Zeta-Fe₂O₃ – A new stable polymorph in iron(III) oxide family,” *Sci. Rep.*, vol. 5, no. 1, p. 15091, Dec. 2015.
- [8] K. Momma and F. Izumi, “VESTA 3 for three-dimensional visualization of crystal, volumetric and morphology data,” *J. Appl. Crystallogr.*, vol. 44, no. 6, pp. 1272–1276, Dec. 2011.
- [9] F. del Monte, M. P. Morales, D. Levy, A. Fernandez, M. Ocaña, A. Roig, E. Molins, K. O’Grady, and C. J. Serna, “Formation of γ -Fe₂O₃ Isolated Nanoparticles in a Silica Matrix,” *Langmuir*, vol. 13, no. 14, pp. 3627–3634, Jul. 1997.
- [10] S. Sakurai, J. Jin, K. Hashimoto, and S. Ohkoshi, “Reorientation Phenomenon in a Magnetic Phase of ε -Fe₂O₃ Nanocrystal,” *J. Phys. Soc. Japan*, vol. 74, no. 7, pp. 1946–1949, Jul. 2005.
- [11] T. Danno, D. Nakatsuka, Y. Kusano, H. Asaoka, M. Nakanishi, T. Fujii, Y. Ikeda, and J. Takada, “Crystal Structure of β -Fe₂O₃ and Topotactic Phase Transformation to α -Fe₂O₃,” *Cryst. Growth Des.*, vol. 13, no. 2, pp. 770–774, Feb. 2013.
- [12] R. L. Blake, R. E. HessevicK, T. Zoltai, and L. W. Finger, “Refinement of the Hematite Structure,” *Am. Mineral.*, vol. 51, pp. 123–129, 1966.
- [13] N. Amin and S. Araj, “Morin temperature of annealed submicronic α -Fe₂O₃ particles,” *Phys. Rev. B*, vol. 35, no. 10, pp. 4810–4811, Apr. 1987.
- [14] R. E. Vandenberghe, C. A. Barrero, G. M. Da Costa, E. Van San, and E. De Grave,

- “Mössbauer characterization of iron oxides and (oxy)hydroxides: The present state of the art,” *Hyperfine Interact.*, vol. 126, no. 1–4, pp. 247–259, 2000.
- [15] M. -Z. Dang, D. G. Rancourt, J. E. Dutrizac, G. Lamarche, and R. Provencher, “Interplay of surface conditions, particle size, stoichiometry, cell parameters, and magnetism in synthetic hematite-like materials,” *Hyperfine Interact.*, vol. 117, no. 1/4, pp. 271–319, 1998.
- [16] G. Schimanke, “In situ XRD study of the phase transition of nanocrystalline maghemite (γ -Fe₂O₃) to hematite (α -Fe₂O₃),” *Solid State Ionics*, vol. 136–137, no. 1–2, pp. 1235–1240, Nov. 2000.
- [17] J. E. Jørgensen, L. Mosegaard, L. E. Thomsen, T. R. Jensen, and J. C. Hanson, “Formation of γ -Fe₂O₃ nanoparticles and vacancy ordering: An in situ X-ray powder diffraction study,” *J. Solid State Chem.*, vol. 180, no. 1, pp. 180–185, 2007.
- [18] J. Tuček, R. Zbořil, A. Namai, and S. Ohkoshi, “ ϵ -Fe₂O₃: An Advanced Nanomaterial Exhibiting Giant Coercive Field, Millimeter-Wave Ferromagnetic Resonance, and Magnetoelectric Coupling,” *Chem. Mater.*, vol. 22, no. 24, pp. 6483–6505, Dec. 2010.
- [19] R. Zboril, M. Mashlan, K. Barcova, and M. Vujtek, “Thermally Induced Solid-State Syntheses of γ -Fe₂O₃ Nanoparticles and Their Transformation to α -Fe₂O₃ via ϵ -Fe₂O₃,” *Hyperfine Interact.*, vol. 139/140, no. 1/4, pp. 597–606, 2002.
- [20] E. Tronc, C. Chane, and J. P. Jolivet, “Structural and Magnetic Characterization of ϵ -Fe₂O₃,” vol. 104, no. 139, pp. 93–104, 1998.
- [21] A. Navrotsky, L. Mazeina, and J. Majzlan, “Size-Driven Structural and Thermodynamic Complexity in Iron Oxides,” *Science (80-.)*, vol. 319, no. 5870, pp. 1635–1638, Mar. 2008.
- [22] C. Laberty and A. Navrotsky, “Energetics of stable and metastable low-temperature iron oxides and oxyhydroxides,” *Geochim. Cosmochim. Acta*, vol. 62, no. 17, pp. 2905–2913, Sep. 1998.
- [23] O. Bomati-Miguel, L. Mazeina, A. Navrotsky, and S. Veintemillas-Verdaguer, “Calorimetric Study of Maghemite Nanoparticles Synthesized by Laser-Induced Pyrolysis,” *Chem. Mater.*, vol. 20, no. 2, pp. 591–598, Jan. 2008.
- [24] J. Jin, K. Hashimoto, and S. Ohkoshi, “Formation of spherical and rod-shaped ϵ -Fe₂O₃ nanocrystals with a large coercive field,” *J. Mater. Chem.*, vol. 15, no. 10, p. 1067, 2005.
- [25] S. Ohkoshi, S. Sakurai, J. Jin, and K. Hashimoto, “The addition effects of alkaline earth ions in the chemical synthesis of ϵ -Fe₂O₃ nanocrystals that exhibit a huge coercive field,” *J. Appl. Phys.*, vol. 97, no. 10, p. 10K312, 2005.
- [26] P. Brázda, D. Nižňanský, J.-L. Rehspringer, and J. P. Vejpravová, “Novel sol–gel method for preparation of high concentration ϵ -Fe₂O₃/SiO₂ nanocomposite,” *J. Sol-Gel Sci. Technol.*, vol. 51, no. 1, pp. 78–83, Jul. 2009.

- [27] J. Tuček, R. Zbořil, A. Namai, and S. Ohkoshi, “ ϵ -Fe₂O₃: An Advanced Nanomaterial Exhibiting Giant Coercive Field, Millimeter-Wave Ferromagnetic Resonance, and Magnetoelectric Coupling,” *Chem. Mater.*, vol. 22, no. 24, pp. 6483–6505, Dec. 2010.
- [28] S. Lee and H. Xu, “Size-Dependent Phase Map and Phase Transformation Kinetics for Nanometric Iron(III) Oxides ($\gamma \rightarrow \epsilon \rightarrow \alpha$ Pathway),” *J. Phys. Chem. C*, vol. 120, no. 24, pp. 13316–13322, Jun. 2016.
- [29] R. Zboril, M. Mashlan, and D. Petridis, “Iron(III) Oxides from Thermal Processes Synthesis, Structural and Magnetic Properties, Mössbauer Spectroscopy Characterization, and Applications †,” *Chem. Mater.*, vol. 14, no. 3, pp. 969–982, Mar. 2002.
- [30] C. Pascal, J. L. Pascal, F. Favier, M. L. E. Moubtassim, and C. Payen, “Electrochemical Synthesis for the Control of γ -Fe₂O₃ Nanoparticle Size. Morphology, Microstructure, and Magnetic Behavior,” *Chem. Mater.*, vol. 11, no. 17, pp. 141–147, 1999.
- [31] S. R. Janasi, M. Emura, F. J. G. Landgraf, and D. Rodrigues, “The effects of synthesis variables on the magnetic properties of coprecipitated barium ferrite powders,” *J. Magn. Magn. Mater.*, vol. 238, no. 2–3, pp. 168–172, 2002.
- [32] K. Deshpande, A. Mukasyan, and A. Varma, “Direct Synthesis of Iron Oxide Nanopowders by the Combustion Approach: Reaction Mechanism and Properties,” *Chem. Mater.*, vol. 16, no. 24, pp. 4896–4904, Nov. 2004.
- [33] K. Kelm and W. Mader, “Synthesis and structural analysis of ϵ -Fe₂O₃,” *Zeitschrift für Anorg. und Allg. Chemie*, vol. 631, no. 12, pp. 2383–2389, 2005.
- [34] J. Navrotsky, Alexandra, Mazeina, Lena, Majzlan, “Size-Driven Structural and Thermodynamic Complexity in Iron Oxides,” *Science (80-.)*, vol. 319, no. 5870, pp. 1635–1638, 2008.
- [35] H. Mehrer, *Diffusion in Solids*, vol. 155. Berlin, Heidelberg: Springer Berlin Heidelberg, 2007.
- [36] D. K. Fislér and S. J. Mackwell, “Kinetics of diffusion-controlled growth of fayalite,” *Phys. Chem. Miner.*, vol. 21, no. 3, pp. 156–165, Jul. 1994.
- [37] J. E. Burke and D. Turnbull, “Recrystallization and grain growth,” *Prog. Met. Phys.*, vol. 3, pp. 220–292, 1952.
- [38] M. F. Yan, “Grain Growth in Fe₃O₄,” *J. Am. Ceram. Soc.*, vol. 63, no. 7–8, pp. 443–447, Jul. 1980.
- [39] S.-J. Cho, J.-C. Idrobo, J. Olamit, K. Liu, N. D. Browning, and S. M. Kauzlarich, “Growth Mechanisms and Oxidation Resistance of Gold-Coated Iron Nanoparticles,” *Chem. Mater.*, vol. 17, no. 12, pp. 3181–3186, Jun. 2005.
- [40] A. Navrotsky, “Energetics of nanoparticle oxides: interplay between surface energy and

- polymorphism Presented at the ACS Division of Geochemistry Symposium "The Impact of Nanoparticle Growth and Transformation Processes on Contaminant Geochemical Cycling", New Orleans, LA, " *Geochem. Trans.*, vol. 4, no. 6, p. 34, 2003.
- [41] L. Vayssières, C. Chanéac, E. Tronc, and J. P. Jolivet, "Size Tailoring of Magnetite Particles Formed by Aqueous Precipitation: An Example of Thermodynamic Stability of Nanometric Oxide Particles," *J. Colloid Interface Sci.*, vol. 205, no. 2, pp. 205–212, Sep. 1998.
- [42] P. Brázda, E. Večerníková, E. Plížingrová, A. Lančok, and D. Nižňanský, "Thermal stability of nanocrystalline ϵ -Fe₂O₃," *J. Therm. Anal. Calorim.*, Apr. 2014.
- [43] M. J. Buerger, *Elementary Crystallography*. New York: John Wiley & Sons, Inc., 1956.
- [44] I. (Tohoku U. Sunagawa, *Crystals Growth, Morphology, and Perfection*. Cambridge University Press, 2005.
- [45] J. M. D. Coey, *Magnetism and Magnetic Materials*: Cambridge: Cambridge University Press, 2001.
- [46] C.-G. Stefanita, *Magnetism Basics and Applications*. New York: Springer-Verlag Berlin Heidelberg, 2012.
- [47] J. M. D. Coey, "Permanent magnetism," *Solid State Commun.*, vol. 102, no. 2–3, pp. 101–105, 1997.
- [48] J. M. D. Coey, *Magnetism and Magnetic Materials*: Cambridge: Cambridge University Press, 2001.
- [49] J. R. Morales, J. E. Garay, M. Biasini, and W. P. Beyermann, "Magnetic characterization of bulk nanostructured iron oxides," *Appl. Phys. Lett.*, vol. 93, no. 2, 2008.
- [50] M. I. Dar and S. A. Shivashankar, "Single crystalline magnetite, maghemite, and hematite nanoparticles with rich coercivity," *RSC Adv.*, vol. 4, no. 8, pp. 4105–4113, 2014.
- [51] K. Kluchova, R. Zboril, J. Tucek, M. Pecova, L. Zajoncova, I. Safarik, M. Mashlan, I. Markova, D. Jancik, M. Sebel, H. Bartonkova, V. Bellesi, P. Novak, and D. Petridis, "Superparamagnetic maghemite nanoparticles from solid-state synthesis - their functionalization towards peroral MRI contrast agent and magnetic carrier for trypsin immobilization.," *Biomaterials*, vol. 30, no. 15, pp. 2855–63, May 2009.
- [52] J. Kohout, P. Brázda, K. Závěta, D. Kubániová, T. Kmječ, L. Kubičková, M. Klementová, E. Šantavá, and A. Lančok, "The magnetic transition in ϵ -Fe₂O₃ nanoparticles: Magnetic properties and hyperfine interactions from Mössbauer spectroscopy," *J. Appl. Phys.*, vol. 117, no. 17, pp. 16–20, 2015.
- [53] E. Taboada, M. Gich, and A. Roig, "Nanospheres of silica with an epsilon-Fe₂O₃ single crystal nucleus.," *ACS Nano*, vol. 3, no. 11, pp. 3377–82, Nov. 2009.

- [54] J. L. Dormann, N. Viart, J. L. Rehspringer, A. Ezzir, and D. Niznansky, "Magnetic properties of Fe₂O₃ particles prepared by sol-gel method," *Hyperfine Interact.*, vol. 112, no. 1–4, pp. 89–92, 1998.
- [55] M. Gich, A. Roig, E. Taboada, E. Molins, C. Bonafos, and E. Snoeck, "Stabilization of metastable phases in spatially restricted fields: the case of the Fe₂O₃ polymorphs," *Faraday Discuss.*, vol. 136, p. 345, 2007.
- [56] J.-L. Rehspringer, S. Vilminot, D. Niznansky, K. Zaveta, C. Estournes, and M. Kurmoo, "A temperature and magnetic field dependence Mössbauer study of ϵ -Fe₂O₃," *Hyperfine Interact.*, vol. 166, no. 1–4, pp. 475–481, Dec. 2006.
- [57] K. T. Chan, J. R. Morales, Y. Kodera, and J. E. Garay, "A processing route for bulk, high coercivity, rare-earth free, nanocomposite magnets based on metastable iron oxide," *J. Mater. Chem. C*, vol. 5, no. 31, pp. 7911–7918, 2017.
- [58] J. Jin, S. Ohkoshi, and K. Hashimoto, "Giant Coercive Field of Nanometer- Sized Iron Oxide," *Adv. Mater.*, vol. 16, no. 1, pp. 48–51, Jan. 2004.
- [59] G. Herzer, "Grain size dependence of coercivity and permeability in nanocrystalline ferromagnets," *IEEE Trans. Magn.*, vol. 26, no. 5, pp. 1397–1402, 1990.
- [60] S. Ohkoshi, A. Namai, and S. Sakurai, "The Origin of Ferromagnetism in ϵ -Fe₂O₃ and ϵ -Ga_xFe_{2-x}O₃ Nanomagnets," *J. Phys. Chem. C*, vol. 113, no. 26, pp. 11235–11238, Jul. 2009.
- [61] Y.-C. Tseng, N. M. Souza-Neto, D. Haskel, M. Gich, C. Frontera, A. Roig, M. van Veenendaal, and J. Nogués, "Nonzero orbital moment in high coercivity ϵ -Fe₂O₃ and low-temperature collapse of the magnetocrystalline anisotropy," *Phys. Rev. B*, vol. 79, no. 9, p. 094404, Mar. 2009.
- [62] P. Brázda, J. Kohout, P. Bezdička, and T. Kmječ, " α -Fe₂O₃ versus β -Fe₂O₃: Controlling the Phase of the Transformation Product of ϵ -Fe₂O₃ in the Fe₂O₃/SiO₂ System," *Cryst. Growth Des.*, vol. 14, no. 3, pp. 1039–1046, Mar. 2014.
- [63] M. M. Rahman, A. Jamal, S. B. Khan, and M. Faisal, "Characterization and applications of as-grown β -Fe₂O₃ nanoparticles prepared by hydrothermal method," *J. Nanoparticle Res.*, vol. 13, no. 9, pp. 3789–3799, Mar. 2011.
- [64] S. Laurent, D. Forge, M. Port, A. Roch, C. Robic, L. Vander Elst, and R. N. Muller, "Magnetic iron oxide nanoparticles: synthesis, stabilization, vectorization, physicochemical characterizations, and biological applications," *Chem. Rev.*, vol. 108, no. 6, pp. 2064–110, Jun. 2008.
- [65] S. R. Janasi, D. Rodrigues, F. J. G. Landgraf, and M. Emura, "Magnetic properties of coprecipitated barium ferrite powders as a function of synthesis conditions," *IEEE Trans. Magn.*, vol. 36, no. 5, pp. 3327–3329, 2000.

- [66] D. Barb, L. Diamandescu, A. Rusi, D. TĂRĂBĂȘANU-MIHĂILĂ, M. Morariu, and V. Teodorescu, "Preparation of barium hexaferrite by a hydrothermal method: structure and magnetic properties," *J. Mater. Sci.*, vol. 21, no. 4, pp. 1118–1122, Apr. 1986.
- [67] M. A. Willard, L. K. Kurihara, E. E. Carpenter, S. Calvin, and V. G. Harris, "Chemically prepared magnetic nanoparticles," *Int. Mater. Rev.*, vol. 49, no. 3–4, pp. 125–170, 2004.
- [68] S. Akbar, S. K. Hasanain, N. Azmat, and M. Nadeem, "Synthesis of Fe₂O₃ nanoparticles by new Sol-Gel method and their structural and magnetic characterizations," pp. 1–19.
- [69] E. M. Rabinovich, J. B. Macchesney, D. W. Johnson, J. R. Simpson, B. W. Meagher, F. V. Dimarcello, D. L. Wood, and E. A. Sigety, "Sol-gel preparation of transparent silica glass," *J. Non. Cryst. Solids*, vol. 63, no. 1–2, pp. 155–161, Feb. 1984.
- [70] O. M. Lemine, K. Omri, B. Zhang, L. El Mir, M. Sajieddine, A. Alyamani, and M. Bououdina, "Sol–gel synthesis of 8nm magnetite (Fe₃O₄) nanoparticles and their magnetic properties," *Superlattices Microstruct.*, vol. 52, no. 4, pp. 793–799, 2012.
- [71] G. Salazar-Alvarez, M. Muhammed, and A. A. Zagorodni, "Novel flow injection synthesis of iron oxide nanoparticles with narrow size distribution," *Chem. Eng. Sci.*, vol. 61, no. 14, pp. 4625–4633, Jul. 2006.
- [72] A. A. Dubrovskiy, D. A. Balaev, K. A. Shaykhutdinov, O. A. Bayukov, O. N. Pletnev, S. S. Yakushkin, G. A. Bukhtiyarova, and O. N. Martyanov, "Size effects in the magnetic properties of ε-Fe₂O₃ nanoparticles," *J. Appl. Phys.*, vol. 118, no. 21, 2015.
- [73] S. Sakurai, K. Tomita, K. Hashimoto, H. Yashiro, and S. Ohkoshi, "Preparation of the Nanowire Form of ε-Fe₂O₃ Single Crystal and a Study of the Formation Process," *J. Phys. Chem. C*, vol. 112, no. 51, pp. 20212–20216, Dec. 2008.
- [74] A. Solids, "SOL-GEL PROCESSING II. The role of the catalyst OF SILICA," vol. 7, 1986.
- [75] D. Zhao, J. Sun, Q. Li, G. D. Stucky, and S. Barbara, "Morphological Control of Highly Ordered Mesoporous Silica SBA-15 Mesoporous materials are of great interest to the materials community because their pore structures as well as catalytic , adsorbed , conductive and magnetic ordered large mesoporous silica ," no. 22, pp. 275–279, 2000.
- [76] R. L. COBLE, "Initial Sintering of Alumina and Hematite," *J. Am. Ceram. Soc.*, vol. 41, no. 2, pp. 55–62, Feb. 1958.
- [77] F. del Monte, M. P. Morales, D. Levy, A. Fernandez, M. Ocaña, A. Roig, E. Molins, K. O'Grady, and C. J. Serna, "Formation of γ-Fe₂O₃ Isolated Nanoparticles in a Silica Matrix," *Langmuir*, vol. 13, no. 14, pp. 3627–3634, Jul. 1997.
- [78] W. Höland and G. H. Beall, *Glass-Ceramic Technology*. Hoboken, NJ, USA: John Wiley & Sons, Inc., 2012.
- [79] N. P. Bansal and R. H. Doremus, *Handbook of glass properties*. Academic Press, 1986.

- [80] G. J. Hooyman, "Thermodynamics of diffusion in multicomponent systems," *Physica*, vol. 22, no. 6–12, pp. 751–759, Jan. 1956.
- [81] J. Kvasnica, "Diffusion in multicomponent systems," *Czechoslov. J. Phys.*, vol. 32, no. 1, pp. 19–21, Jan. 1982.
- [82] M. P. BOROM and J. A. PASK, "Kinetics of Dissolution and Diffusion of the Oxides of Iron in Sodium Disilicate Glass," *J. Am. Ceram. Soc.*, vol. 51, no. 9, pp. 490–498, Sep. 1968.
- [83] O. Kononchuk, K. G. Korablev, N. Yarykin, and G. A. Rozgonyi, "Diffusion of iron in the silicon dioxide layer of silicon-on-insulator structures," *Appl. Phys. Lett.*, vol. 73, no. 9, pp. 1206–1208, 1998.
- [84] D. A. Ramappa, "Diffusion of Iron in Silicon Dioxide," *J. Electrochem. Soc.*, vol. 146, no. 10, p. 3773, 1999.
- [85] D. K. McElfresh and D. G. Howitt, "Activation Enthalpy for Diffusion in Glass," *J. Am. Ceram. Soc.*, vol. 69, no. 10, p. C-237-C-238, 1986.
- [86] B. Karmakar, "Introduction to functional glasses and glass-ceramics," in *Functional Glasses and Glass-Ceramics*, Elsevier, 2017, pp. 3–21.
- [87] C. Suryanarayana, "Mechanical alloying and milling," *Prog. Mater. Sci.*, vol. 46, no. 1–2, pp. 1–184, Jan. 2001.
- [88] S. Begin-colin, G. Le Caer, A. Mocellin, and M. Zandona, "Polymorphic transformations of titania induced by ball milling," *Philos. Mag. Lett.*, vol. 69, no. 1, pp. 1–7, Jan. 1994.
- [89] A. Y. Fong, H. Xu, K. Page, M. R. Dirmyer, Y. Kodera, S. J. Obrey, and J. E. Garay, "Synthesis and structural characterization of dense polycrystalline Mg₉Sn₅, a metastable Mg–Sn phase," *J. Alloys Compd.*, vol. 616, pp. 333–339, Dec. 2014.
- [90] R. H. R. Castro, S. V. Ushakov, L. Gengembre, D. Gouvêa, and A. Navrotsky, "Surface Energy and Thermodynamic Stability of γ -Alumina: Effect of Dopants and Water," *Chem. Mater.*, vol. 18, no. 7, pp. 1867–1872, Apr. 2006.
- [91] R. J. Fruehan, "The rate of reduction of iron oxides by carbon," *Metall. Trans. B*, vol. 8, no. 1, pp. 279–286, Mar. 1977.
- [92] K. Mondal, H. Lorethova, E. Hippo, T. Wiltowski, and S. B. Lalvani, "Reduction of iron oxide in carbon monoxide atmosphere - Reaction controlled kinetics," *Fuel Process. Technol.*, vol. 86, no. 1, pp. 33–47, 2004.
- [93] A. Volodchenkov, "Synthesis and Characterization of Metal - Oxide Composite Materials for Permanent Magnetic Applications," *Annu. Rev. Mater. Res.*, no. September, 2012.
- [94] I. Chen and X. Wang, "Sintering dense nanocrystalline ceramics without final-stage grain

- growth,” *Nature*, vol. 404, no. 6774, pp. 168–71, Mar. 2000.
- [95] M. Cologna, B. Rashkova, and R. Raj, “Flash Sintering of Nanograin Zirconia in <5 s at 850°C,” *J. Am. Ceram. Soc.*, vol. 93, no. 11, pp. 3556–3559, Nov. 2010.
- [96] J. Perelaer, M. Klokkenburg, C. E. Hendriks, and U. S. Schubert, “Microwave Flash Sintering of Inkjet-Printed Silver Tracks on Polymer Substrates,” *Adv. Mater.*, vol. 21, no. 47, pp. 4830–4834, Dec. 2009.
- [97] W. E. Frazier, “Metal Additive Manufacturing: A Review,” *J. Mater. Eng. Perform.*, vol. 23, no. 6, pp. 1917–1928, Jun. 2014.
- [98] H. V. Atkinson and S. Davies, “Fundamental aspects of hot isostatic pressing: An overview,” *Metall. Mater. Trans. A*, vol. 31, no. 12, pp. 2981–3000, Dec. 2000.
- [99] M. Decottignies, J. Phalippou, and J. Zarzycki, “Synthesis of glasses by hot-pressing of gels,” *J. Mater. Sci.*, vol. 13, no. 12, pp. 2605–2618, Dec. 1978.
- [100] H. T. Larker and R. Larker, “Hot Isostatic Pressing,” in *Materials Science and Technology*, Weinheim, Germany: Wiley-VCH Verlag GmbH & Co. KGaA, 2006.
- [101] J. E. Garay, “Current-Activated, Pressure-Assisted Densification of Materials,” *Annu. Rev. Mater. Res.*, vol. 40, no. 1, pp. 445–468, Jun. 2010.
- [102] S. Foner, “Versatile and Sensitive Vibrating-Sample Magnetometer,” *Rev. Sci. Instrum.*, vol. 30, no. 7, pp. 548–557, 1959.
- [103] C. Kittel, “On the Theory of Ferromagnetic Resonance Absorption,” *Phys. Rev.*, vol. 73, no. 2, pp. 155–161, Jan. 1948.
- [104] L. Walker, “Magnetostatic Modes in Ferromagnetic Resonance,” *Phys. Rev.*, vol. 105, no. 2, pp. 390–399, Jan. 1957.
- [105] S. S. Yakushkin, G. A. Bukhtiyarova, and O. N. Martyanov, “Formation conditions of a magnetically ordered phase ϵ -Fe₂O₃. A FMR in situ study,” *J. Struct. Chem.*, vol. 54, no. 5, pp. 876–882, Sep. 2013.
- [106] Y. Chen, T. Sakai, T. Chen, S. D. Yoon, A. L. Geiler, C. Vittoria, and V. G. Harris, “Oriented barium hexaferrite thick films with narrow ferromagnetic resonance linewidth,” *Appl. Phys. Lett.*, vol. 88, no. 6, 2006.
- [107] B. D. Cullity, “Elements of X-Ray Diffraction,” *Am. J. Phys.*, vol. 25, no. 6, p. 394, 1957.
- [108] V. Kazmiruk, *Scanning Electron Microscopy*. Croatia, 2012.
- [109] M. Gich, A. Roig, E. Taboada, E. Molins, C. Bonafos, and E. Snoeck, “Stabilization of metastable phases in spatially restricted fields: the case of the Fe₂O₃ polymorphs,” *Faraday Discuss.*, vol. 136, p. 345, 2007.

- [110] K. Mori, Y. Oaki, M. Suda, Y. Einaga, and H. Imai, "Formation of ϵ -Fe₂O₃ Nanocrystals through Segregation in Mesoporous Silica Particles," *Chem. Lett.*, vol. 37, no. 8, pp. 814–815, 2008.
- [111] E. V. Belova, Y. A. Kolyagin, and I. A. Uspenskaya, "Structure and glass transition temperature of sodium-silicate glasses doped with iron," *J. Non. Cryst. Solids*, vol. 423–424, pp. 50–57, Sep. 2015.
- [112] L. S. Darken, "Melting Points of Iron Oxides on Silica; Phase Equilibria in the System Fe-Si-O as a Function of Gas Composition and Temperature," *J. Am. Chem. Soc.*, vol. 70, no. 6, pp. 2046–2053, 1948.
- [113] N. Amin, S. Arajs, and E. Matijevic, "Magnetic properties of submicronic α -Fe₂O₃ particles of uniform size distribution at 300 K," *Phys. Status Solidi*, vol. 104, no. 1, pp. K65–K68, Nov. 1987.
- [114] C. T. Rodgers, "Magnetic field effects in chemical systems," *Pure Appl. Chem.*, vol. 81, no. 1, pp. 19–43, 2009.
- [115] H. Pender and R. L. Jones, "The Annealing of Steel in an Alternating Magnetic Field," *Phys. Rev.*, vol. 1, no. 4, pp. 259–273, Apr. 1913.
- [116] J. Wang, Q. Chen, C. Zeng, and B. Hou, "Magnetic-field-induced growth of single-crystalline Fe₃O₄ nanowires," *Adv. Mater.*, vol. 16, no. 2, pp. 137–140, 2004.
- [117] M. Gich, C. Frontera, A. Roig, J. Fontcuberta, E. Molins, N. Bellido, C. Simon, and C. Fleta, "Magnetoelectric coupling in ϵ -Fe₂O₃ nanoparticles," *Nanotechnology*, vol. 17, no. 3, pp. 687–691, Feb. 2006.
- [118] A. A. Dubrovskiy, D. A. Balaev, K. A. Shaykhutdinov, O. A. Bayukov, O. N. Pletnev, S. S. Yakushkin, G. A. Bukhtiyarova, and O. N. Martyanov, "Size effects in the magnetic properties of ϵ -Fe₂O₃ nanoparticles," *J. Appl. Phys.*, vol. 118, no. 21, 2015.
- [119] Y. Y. Meng, M. H. He, Q. Zeng, D. L. Jiao, S. Shukla, R. V. Ramanujan, and Z. W. Liu, "Synthesis of barium ferrite ultrafine powders by a sol-gel combustion method using glycine gels," *J. Alloys Compd.*, vol. 583, pp. 220–225, 2014.
- [120] Y. Y. Song, J. Das, Z. Wang, W. Tong, and C. E. Patton, "In-plane c-axis oriented barium ferrite films with self-bias and low microwave loss," *Appl. Phys. Lett.*, vol. 93, no. 17, pp. 17–20, 2008.
- [121] M. Sagawa, S. Fujimura, N. Togawa, H. Yamamoto, and Y. Matsuura, "New material for permanent magnets on a base of Nd and Fe (invited)," *J. Appl. Phys.*, vol. 55, no. 6, pp. 2083–2087, 1984.
- [122] K.-D. Durst and H. Kronmüller, "The coercive field of sintered and melt-spun NdFeB magnets," *J. Magn. Magn. Mater.*, vol. 68, no. 1, pp. 63–75, Aug. 1987.